NEAR-INFRARED DIODE LASER ABSORPTION SPECTROSCOPY WITH APPLICATIONS TO REACTIVE SYSTEMS AND COMBUSTION CONTROL

A DISSERTATION

SUBMITTED TO THE DEPARTMENT OF MECHANICAL ENGINEERING

AND THE COMMITTEE ON GRADUATE STUDIES

OF STANFORD UNIVERSITY

IN PARTIAL FULFILLMENT OF THE REQUIREMENTS FOR THE DEGREE OF

DOCTOR OF PHILOSOPHY

Hejie Li

September 2007

I certify that I have read this dissertation and that, in my opinion, it is fully adequate in scope and quality as a dissertation for the degree of Doctor of Philosophy.

_____
(Ronald K. Hanson) Principal Adviser

I certify that I have read this dissertation and that, in my opinion, it is fully adequate in scope and quality as a dissertation for the degree of Doctor of Philosophy.

_____
(Craig T. Bowman)

I certify that I have read this dissertation and that, in my opinion, it is fully adequate in scope and quality as a dissertation for the degree of Doctor of Philosophy.

_____
(Jay B. Jeffries)

Approved for the University Committee on Graduate Studies.

ABSTRACT

Tunable diode laser (TDL) absorption spectroscopy based on H_2O absorption in the near-infrared (NIR) provides a non-intrusive, fast, and sensitive method for reliable detection of various important gas parameters. Although much progress has already been made using TDL sensing of H_2O, the success of these sensors has provided many new opportunities. This thesis extends and applies two techniques, wavelength-scanned direct absorption and wavelength modulation spectroscopy (WMS), to practical and laboratory combustion experiments and uses a TDL sensor for real-time combustion control.

Quantitative absorption measurements require accurate spectroscopic data for the probed transitions. The work presented here adds to the H_2O NIR spectroscopic database. High-resolution absorption lineshapes of selected H_2O transitions have been recorded in a heated static cell. Strong collisional narrowing effects are observed in the Ar-broadened H_2O spectra due to the relatively weak collisional broadening induced by Ar-H_2O collisions. Temperature dependences of the Ar-induced broadening, narrowing, and shift coefficients are determined using Galatry fits to the absorption data.

A fiber-coupled TDL sensor system based on direct absorption spectroscopy is developed to measure gas temperature and H_2O concentration in the harsh environment of coal-fired power plants. The field measurement results at a TVA 280 MW power plant demonstrate the utility of the TDL sensor for *in-situ* measurements for combustion optimization in large-scale facilities.

TDL absorption measurements at high pressures using WMS require large modulation depths for optimum detection of blended molecular absorption spectra. In these measurements, real diode laser performance, including the phase shift between frequency modulation and intensity modulation and nonlinear intensity modulation, becomes important. Following published theory, these parameters are incorporated for

the first time into an improved model of the WMS signal. The influence of these non-ideal laser effects is investigated via wavelength-scanned WMS measurements as a function of pressure on H_2O rovibrational transitions near 1388 nm.

A fast-response (100 kHz) TDL absorption sensor is developed for studies of combustion chemistry in shock tubes when there is significant heat release. Gas temperature is determined from the ratio of fixed-wavelength laser absorption of two H_2O transitions near 7185.60 and 7154.35 cm^{-1}, which are selected using design rules for target conditions. WMS is employed with $2f$ detection to improve the sensor sensitivity and accuracy. Normalization of the second-harmonic signal by the first-harmonic signal is used to remove the need for calibration and minimize interference from emission, scattering, and beam steering. Before being used in combustion chemistry experiments, the WMS-$2f$ sensor is validated in a heated cell and shock tests with H_2O-Ar mixtures.

A simple gasdynamic model called CHEMSHOCK is developed to predict gas temperature and species concentrations behind reflected shock waves with significant energy release. CHEMSHOCK is based on combining constant-U,V reaction with isentropic expansion (or compression) to the measured pressure for a control mass of gas mixture in infinitesimal time steps. This new CHEMSHOCK model is first validated with 1-D reacting computational fluid dynamics (CFD) calculations using a reduced heptane mechanism, and then compared to the gas temperature and H_2O concentration measured by the fast TDL sensor. The computational time for the CHEMSHOCK model is significantly reduced relative to the 1-D reacting CFD model. CHEMSHOCK provides a convenient simulation tool, in conjunction with diagnostics for pressure, temperature, and species, to study various combustion mechanisms over a wide range of conditions.

Combustion instabilities are monitored in propane/air flames in a swirl-stabilized combustor using a real-time TDL temperature sensor for feedback control. Detailed experiments are conducted to optimize the position of the sensor line-of-sight in the flame for thermoacoustic instability and lean blowout (LBO) sensing. The intensity of the low-frequency fluctuations is used to detect the proximity to LBO and as a control variable for feedback LBO suppression without knowing the LBO fuel/air ratio limit.

ACKNOWLEDGMENTS

TABLE OF CONTENTS

LIST OF TABLES

LIST OF FIGURES

xvii

Chapter 1

INTRODUCTION

1.1 Motivation and scope

Hydrocarbon combustion is currently the most common method for power generation in the world. Recent efforts to improve power and propulsion systems are directed toward more environmentally friendly power generation with improved combustion efficiency and reduced pollutant emissions. Gas temperature is a key parameter of the combustion process and a good indicator of combustion efficiency. In combustion kinetics, temperature has an important effect on the rate of chemical reactions, and thus the formation of pollutant emissions. For example, lower flame temperatures can reduce the production of NOx [Martin and Brown 1990; Lefebvre 1999]. Thus, gas temperature has potential for use as a control variable in real-time combustion control to improve efficiency and reduce pollutant levels.

Diode laser absorption spectroscopy provides a non-intrusive, fast, and sensitive method for reliable sensing of various gas parameters in a variety of combustion applications. Semiconductor diode lasers offer many advantages, such as simple control, small size, light weight, low cost, and fast direct modulation capability. Room temperature, narrow-linewidth, tunable diode lasers (TDL) have been demonstrated successfully for temperature, pressure, concentration, and flow velocity measurements in gases by various researchers [Philippe and Hanson 1993; Baer *et al.* 1996; Allen 1998; Silver and Kane 1999; Richter *et al.* 2000; Sanders *et al.* 2000; Teichert *et al.* 2003; Lyle 2005]. Semiconductor diode laser technology has become quite robust in the near-infrared (NIR) because of telecommunications investments. Fiber-coupled diode lasers are readily available which can access combination bands of water vapor. Water vapor is

a significant component of the atmosphere and a major combustion product of hydrocarbon fuels, and has a strong absorption spectrum in the NIR [Herzberg 1945]. Therefore, H_2O is often chosen as the target absorbing species for temperature measurements in reactive systems. This thesis also focuses on NIR diode laser absorption spectroscopy based on H_2O.

Most of the developed TDL sensors are based on direct absorption techniques due to the relatively simple interpretation of measurement results [Arroyo and Hanson 1993; Baer *et al.* 1996; Allen 1998; Zhou *et al.* 2003]. Gas temperature can be determined from the ratio of peak absorbance or spectrally integrated absorbance of two transitions with line strengths that exhibit different temperature dependences due to differences in lower-state energy [Liu *et al.* 2004c]. For scanned-wavelength direct absorption measurements, high-resolution absorption lineshapes are recorded by scanning the laser wavelength across the absorption features. The sensor bandwidth is usually limited to several kHz by the wide laser scanning range needed to reach the non-absorbing wings of the spectroscopic features, in order to infer the zero-absorption baseline. In addition, this technique is less effective for high pressure applications where molecular absorption spectra are blended by collisional broadening. A fixed-wavelength direct absorption technique may be used to improve the sensor bandwidth [Sanders *et al.* 2000]. However, these direct absorption methods can be prone to errors for low-absorption applications because of various noise sources such as beam steering and baseline-fitting errors.

Wavelength modulation spectroscopy (WMS), as an extension of absorption spectroscopy, is a well-known technique for improving the signal-to-noise ratio (SNR) [Bomse *et al.* 1992; Philippe and Hanson 1993; Silver and Kane 1999; Liu *et al.* 2004a]. In this technique, the laser wavelength is rapidly modulated (typically hundreds of kHz), and the second harmonic of the laser transmission signal (WMS-2*f* signal) is recorded by a lock-in amplifier. Gas temperature can be inferred from the ratio of the WMS-2*f* signals of two transitions [Zhou *et al.* 2005a]. This technique is sensitive to absorption lineshape curvature rather than the absorption magnitude alone, and is also insensitive to low-frequency noise. Thus WMS-2*f* offers benefits over direct absorption in terms of noise

resistance and sensitivity. These benefits make WMS with second-harmonic detection an attractive technique for combustion measurements. However, TDL absorption measurements at high pressures by use of WMS require large modulation depths for optimum detection of blended transitions [Liu *et al.* 2004b]. The WMS theory needs to be extended in such cases to include real diode laser performance characteristics such as simultaneous frequency modulation (FM) and intensity modulation (IM), the phase shift between FM and IM, and nonlinear IM. This thesis characterizes the real diode laser parameters and incorporates them into the improved model of the WMS signal. This provides the ground work for large-modulation-depth WMS for diode laser absorption measurements in high-pressure gases (e.g., IC engines [Rieker *et al.* 2007a]).

The development and accuracy of TDL sensors rely on the knowledge of spectral parameters for the selected transitions of the target species, including linecenter position, line strength, lower-state energy and lineshape information. The HITRAN spectroscopy database [Rothman *et al.* 2005] provides a good reference for sensor design. However, the spectroscopic parameters of the selected transitions must be validated before use in a combustion sensor, since HITRAN was originally designed for atmospheric monitoring applications where the temperature range is limited to a few hundred K. In addition, some important spectral parameters are not listed in the HITRAN database, such as the Ar-broadening parameter and its temperature dependence needed for shock tube chemistry studies in Ar-diluted mixtures. These motivate the quantitative study of selected NIR H_2O transitions in a well-controlled laboratory environment (e.g., a heated static cell) presented in this thesis.

Detailed chemical mechanisms are required in the design of modern combustion systems to optimize fuel consumption and pollutant formation [Glassman 1996]. Chemical kinetics studies in the controlled pressure and temperature environment of shock tubes have provided important reaction rate parameters needed for such mechanisms as well as validation of complete combustion mechanisms [Bowman and Hanson 1979; Curran *et al.* 1998; Hanson and Davidson 2001]. When the heat release of the post-shock chemistry is small compared to the heat capacity of the gas mixture, the

temperature increase (due to chemical reactions) will be insignificant [Davidson and Hanson 2004], and the post-shock (incident and reflected) temperatures are precisely given by the measured shock velocity and the standard shock wave relations. However, it is desirable to test chemical mechanisms of combustible mixtures that provide significant heat release. For these chemical kinetics shock tube experiments, a fast temperature sensor providing accurate temperature time-histories can improve the quality of kinetic data. This thesis also reports the development of a fast-response (100 kHz) NIR diode laser absorption sensor for nonintrusive measurements of gas temperature and H_2O concentration behind reflected shock waves, thus providing a new diagnostic tool to study the hydrocarbon combustion mechanisms over a wide range of conditions.

There is also a need for a fast computational model that can provide accurate temperature and species concentrations time-histories for chemical kinetics shock tube experiments with significant heat release behind the reflected shock wave, where measurements are typically made. Such a model can enable quantitative use of experimental data and inference of reaction rate information. This thesis reports the development and validation of a model called CHEMSHOCK, which is based on combining constant-U,V reaction with isentropic expansion (or compression) to the measured pressure for a control mass of gas mixture in infinitesimal time steps. The CHEMSHOCK model significantly reduces (by orders of magnitude) computational time compared to a computational fluid dynamics (CFD) calculation. This time-savings is especially valuable for reflected shock calculations with finite rate chemistry using large combustion mechanisms. This new model is capable of accurately and efficiently predicting combustion gas temperature and species concentrations behind reflected shock waves. The resulting model provides a convenient simulation method to study various hydrocarbon combustion mechanisms over a wide range of conditions.

Emissions legislation has motivated the development of combustors that operate at leaner fuel/air equivalence ratios, where lower flame temperatures reduce the production of NOx. However, fuel-lean combustion is susceptible to instabilities in the form of thermoacoustic oscillations and lean blowout, which pose a serious problem for the

operation of low-emission gas turbine combustors. This thesis also demonstrates the application of a TDL temperature sensor for sensing and feedback control of combustion instabilities in a swirl-stabilized combustor which serves as a model of a gas turbine combustor.

1.2   Organization of thesis

The aim of this thesis is to extend and apply NIR diode laser absorption spectroscopy to various reactive systems and real-time combustion control. Chapter 2 presents the fundamentals of high-resolution diode laser absorption spectroscopy including line broadening and narrowing mechanisms. Both scanned-wavelength and fixed-wavelength direct absorption sensing strategies are discussed. Chapter 3 presents the quantitative spectroscopy of H_2O transitions in the NIR. Line strength and broadening coefficient measurements are described for H_2O transitions suitable for short-path and long-path applications. A sample application of diode laser direct-absorption spectroscopy is given for coal-fired power plants through collaboration with Zolo Technologies Inc. The collisional narrowing effect on Ar-perturbed H_2O lineshapes is also presented in detail. Wavelength modulation spectroscopy is extended to include real diode laser performance in Chapter 4. It is also shown that normalizing the WMS-$2f$ signal by the $1f$ signal and including the laser performance parameters can remove the need for calibration.

Chapter 5 presents the development of a rapid (100 kHz) TDL sensor for measuring gas temperature and H_2O concentration in shock tubes to study combustion mechanisms of hydrocarbon fuels. The sensor is based on fixed-wavelength absorption of two H_2O rovibrational transitions near 1.4 μm. A simple gasdynamic model, called CHEMSHOCK, is developed in Chapter 6 to predict the temporal evolution of combustion gas temperature and species concentration behind reflected shock waves with significant energy release. The CHEMSHOCK simulation results are compared to experimental results, for temperature and water vapor concentration, obtained with the TDL sensor developed in Chapter 5.

Chapter 7 explores the application of a real-time single-laser temperature sensor in sensing and control of combustion instabilities in a swirl-stabilized combustor. Thermoacoustic instability and lean blowout are monitored with optimized sensor position. A feedback control system is developed to suppress LBO. Chapter 8 summarizes the thesis and suggests future work.

Appendix A investigates the potential of diode laser-induced fluorescence of H_2O as a spatially-resolved gasdynamic diagnostic. Appendix B summarizes the design of a long-path flat flame burner. Appendix C describes the hardware and software involved in the real-time combustion control system. The cited references are listed alphabetically at the end of the thesis.

Chapter 2

DIODE LASER ABSORPTION SPECTROSCOPY

Diode laser absorption spectroscopy offers great advantages for rapid *in-situ* gas sensing in various environments. TDL sensors based on high-resolution absorption spectroscopy have been demonstrated for nonintrusive measurements of temperature, pressure, species concentration, and flow velocity in a variety of applications [Arroyo and Hanson 1993; Philippe and Hanson 1993; Baer *et al.* 1996; Allen 1998; Richter *et al.* 2000; Sanders *et al.* 2000; Teichert *et al.* 2003]. Most of these TDL sensors are based on direct absorption techniques due to the relatively simple interpretation of measurement results. This chapter will cover the fundamentals of diode laser absorption spectroscopy including lineshape broadening and narrowing mechanisms. A brief discussion of various direct absorption sensing strategies will be carried out in Section 2.3.

2.1 Beer-Lambert law

The transmission of monochromatic radiation at frequency v through a uniform medium of length L (cm) (Fig 2.1) is given by the Beer-Lambert relation

$$\tau_v = \left(\frac{I_t}{I_0}\right)_v = \exp(-\alpha_v),$$ (2.1)

where I_t and I_0 are the transmitted and incident laser intensities, respectively, and α_v represents the spectral absorbance.
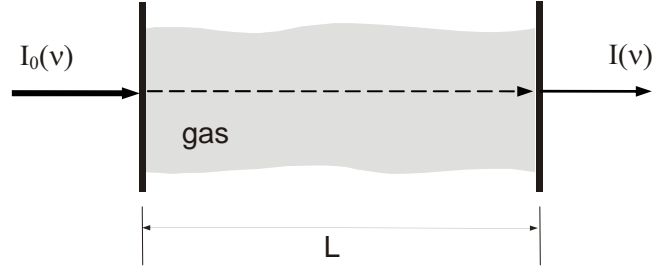
Figure 2.1   Schematic of typical absorption measurements.

For an isolated transition,

$$\alpha_v = P\chi_{abs}S(T)\varphi_v L,\qquad(2.2)$$

where P (atm) is total gas pressure, χ_{abs} is the mole fraction of the absorbing species, T (K) is gas temperature, S (cm^{-2}/atm) and φ_v (cm) are the line strength and lineshape function for the absorption feature. The lineshape function φ_v is normalized such that $\int_{-\infty}^{\infty}\varphi_v dv \equiv 1$ and the integrated absorbance area (cm^{-1}) can be expressed as

$$A = \int_{-\infty}^{\infty}\alpha_v dv = P\chi_{abs}S(T)L.\qquad(2.3)$$

The temperature-dependent line strength is given by

$$S(T) = S(T_0)\frac{Q(T_0)}{Q(T)}\left(\frac{T_0}{T}\right)\exp\left[-\frac{hcE''}{k}\left(\frac{1}{T}-\frac{1}{T_0}\right)\right]\left[1-\exp\left(-\frac{hcv_0}{kT}\right)\right]\left[1-\exp\left(-\frac{hcv_0}{kT_0}\right)\right]^{-1},\quad(2.4)$$

where $S(T_0)$ is the line strength at reference temperature (usually T_0=296 K), $Q(T)$ the partition function of the absorbing molecule [Gamache *et al.* 2000], h (J s) Planck's constant, c (cm/s) the speed of light, k (J/K) Boltzmann's constant, E'' (cm^{-1}) the lower state energy and v_0 (cm^{-1}) the linecenter frequency of the transition.

2.2 Lineshape mechanisms

Any spectral transition possesses a finite line width and specific lineshape due to the uncertainty principle [Yariv 1982], random thermal motion of absorbing molecules, and dynamics of molecular interactions. For NIR TDL absorption measurements, the

instrument broadening, associated with the spectral line width of the lasers, is negligibly small compared to other lineshape effects. Lineshape mechanisms that are important to quantitative spectral measurements in the NIR are discussed in the following sections. Lineshape broadening mechanisms can be classified into homogeneous broadening which affects all molecules in the same way, and inhomogeneous broadening for which the interaction varies with different groups of molecules. Lineshape narrowing mechanisms which are important for some applications will also be covered in this section.

2.2.1 Doppler broadening

Doppler broadening is one inhomogeneous broadening mechanism, and arises from the random thermal motion of the absorber molecules. From equilibrium statistical mechanics, the distribution of molecular velocity follows the Maxwellian velocity distribution [Vincenti and Kruger 1965]. Hence, the Doppler lineshape is given by a Gaussian profile:

$$\phi_D = \frac{2}{\Delta \nu_D} \sqrt{\frac{\ln 2}{\pi}} \exp\left[-4\ln 2 \left(\frac{\nu - \nu_0}{\Delta \nu_D} \right)^2 \right], \quad (2.5)$$

where $\Delta \nu_D (\text{cm}^{-1})$ is the Doppler full width at half maximum (FWHM), and is given by

$$\Delta \nu_D = 2\sqrt{\ln 2}\Delta \nu_D' = 7.162 \times 10^{-7} \nu_0 \sqrt{T/M}, \quad (2.6)$$

where M (g/mol) is the molecular weight of the absorbing species and $\Delta \nu_D'$ is the $1/e$ Doppler halfwidth. The Doppler FWHM provides a measure of gas temperature when the Doppler broadening is dominant (e.g., at low pressures or high temperatures).

2.2.2 Collisional broadening and shift

Collisional (pressure) broadening and shift of spectral lines originate from molecular interactions. Collisional (pressure) broadening is one important homogeneous broadening mechanism, and arises from collisions of absorbing molecules with other molecules. The uncertainty principle can be used to understand this phenomenon. The more likely

collisions are to occur, the more likely lifetime of a molecule in an energy level is shortened and transitions are broadened. The resulting lineshape is given by a Lorentzian profile:

$$\phi_L = \frac{1}{\pi} \frac{\Delta v_C / 2}{\left(v - v_0\right)^2 + \left(\Delta v_C / 2\right)^2}, \tag{2.7}$$

where Δv_C (cm^{-1}) is the collisional FWHM, and is proportional to the system pressure as follows:

$$\Delta v_C = P 2\gamma = P \sum_i \chi_i 2\gamma_i . \tag{2.8}$$

Here γ_i (cm^{-1}/atm) is the collisional broadening coefficient of absorbing species for perturber i with mole fraction χ_i. The temperature dependence of the collisional broadening coefficient can be expressed in terms of the temperature exponent n as

$$\gamma_i\left(T\right) = \gamma_i\left(T_0\right)\left(T_0 / T\right)^n . \tag{2.9}$$

Interaction of two collision partners can also lead to differences in the energy spacings, and hence the frequencies of the different transitions. The collisional (pressure) -induced line shift is proportional to the system pressure:

$$v_0' - v_0 = P\delta = P \sum_i \chi_i \delta_i , \tag{2.10}$$

where v_0' is the pressure shifted linecenter, and δ_i (cm^{-1}atm^{-1}) is the shifting coefficient of absorbing species for perturber i with mole fraction χ_i. The temperature dependence of the shifting coefficient can be expressed in terms of the temperature exponent m as

$$\delta_i\left(T\right) = \delta_i(T_0)\left(T_0 / T\right)^m . \tag{2.11}$$

2.2.3 Voigt profile

If the collisional broadening effect is assumed statistically independent of the thermal motion, the lineshape profile is a convolution of the Gaussian and Lorentzian

components. This convolution results in a Voigt profile [Schreier 1992], which is expressed as

$$V(x',y) = \frac{y}{\pi} \int_{-\infty}^{\infty} d\xi \frac{\exp(-\xi^2)}{y^2 + (x'-\xi)^2} = \text{Re}\left[w(x',y)\right], \tag{2.12}$$

where $x' = (\nu - \nu_0')/\Delta\nu_D'$ is the normalized frequency detuning relative to the pressure shifted linecenter ν_0', $y = P\gamma/\Delta\nu_D'$ is the normalized collisional (pressure) broadening parameter, and $w(x',y)$ is the complex probability function. Note y is linearly proportional to pressure and is identical to the Voigt parameter a $(= \Delta\nu_C/2\Delta\nu_D')$. When Doppler broadening is dominant (i.e., $y \to 0$), the Voigt profile is reduced to a Gaussian profile; when collisional broadening is dominant (i.e., $y \gg 1$), the Voigt profile is reduced to a Lorentzian profile. The Voigt profile is usually calculated using numerical approximations [Whiting 1976].
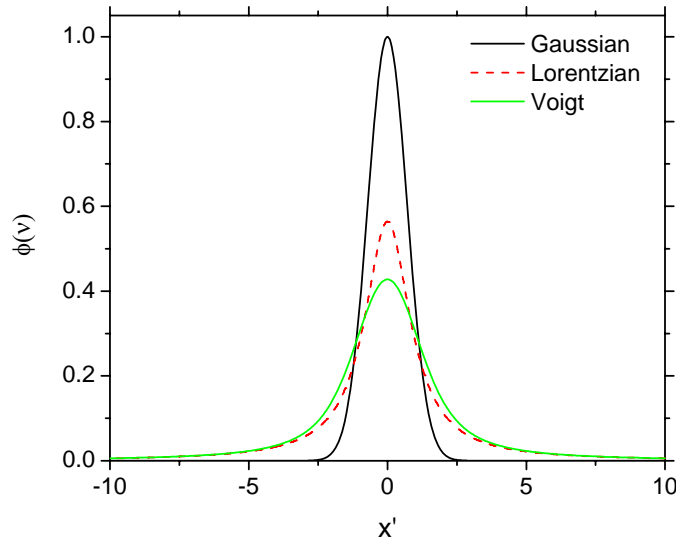
Figure 2.2   Comparison of Gaussian, Lorentzian, and Voigt profiles with same area (for $\Delta\nu_C = 2\Delta\nu_D'$).

Figure 2.2 compares the Gaussian, Lorentzian, and Voigt profiles with same area ($\Delta\nu_C = 2\Delta\nu'_D$). The Gaussian profile decays rapidly from the linecenter while the Lorentzian profile decays slowly. The Voigt profile resembles the Lorentzian profile in the far wings. The Voigt profile is the most widely used lineshape in atmospheric pressure applications since both Doppler and collisional broadening are important. It has good computational efficiency and generally yields adequate results for applications such as combustion measurements. However, through combining the Doppler and collisional broadening effects, the phase-perturbing collisions are idealized as speed-independent and the effects of velocity-averaging collisions are neglected.

2.2.4 Collisional (Dicke) narrowing

Collisions can also narrow spectral profiles in addition to line broadening due to phase-changing collisions [Dicke 1953]. The phenomenon of collisional (Dicke) narrowing has been studied extensively for molecules with large rotational level spacings (e.g. H_2O, HCN and HF) [Eng *et al.* 1972; Pine *et al.* 1980; Varghese 1983; Chou *et al.* 1999]. The collisional-narrowing effect on H_2O transitions was first observed by Eng *et al.* [1972] on a transition in the ν_2 band near 1879.02 cm^{-1} perturbed by Ar and Xe. More recently, Claveau *et al.* [2001] reported precise Fourier transform spectroscopy measurements of absorption lineshapes in the R branch of the ν_2 band of H_2O perturbed by He, Ne, Ar, Kr and N_2, in a pressure range where collisional narrowing and broadening are both observable. In the NIR, collisional narrowing by air, N_2, O_2, and Ar was examined for H_2O lines in the 720-nm wavelength region by Grossmann and Browell [1989] using cw ring dye laser absorption. More recently, collisional narrowing effects were observed on H_2O lines broadened by N_2 and CO_2 in the 1.4 μm region by Nagali *et al.* [1997] using InGaAsP diode laser absorption. Lepere *et al.* [2001] have measured the collisional broadening and narrowing coefficients of H_2O lines perturbed by N_2, O_2, He, and Ar in the region of 1.39 μm using a White-type cell at room temperature.

A simple physical explanation of collision-induced (or collisional) narrowing can be found in Varghese and Hanson [1984] and Chou *et al.* [1999, 2000], based on uncertainty

principle arguments, which are similar to those used to understand the broadening of spectral lineshapes by internal state-perturbing collisions. In short, the velocity-changing collisions reduce the net Doppler broadening, and the actual lineshape is somewhat narrower than one calculated neglecting this effect [Varghese and Hanson 1984]. This effect may be modeled analytically in two limits denoted as hard ($M_1 \ll M_2$) and soft ($M_1 \gg M_2$) collisions; here M_1 and M_2 are the molecular weight of the absorber and perturber. In both models, a narrowing parameter is introduced as the effective frequency of the velocity-changing collisions. The hard collision model [Rautian and Sobel'man 1967] assumes that the velocity of a molecule after collision is completely uncorrelated to the velocity prior to the collision; while the soft collision model [Galatry 1961] assumes that a substantial change in velocity requires a large number of collisions. The soft collision model is also appropriate for more general situations (e.g., when M_1, M_2 are not very different), since infinitesimal velocity changes can also arise in small angle scattering from the long-range part of the intermolecular potential [Varghese and Hanson 1984]. Therefore, the soft collision model can be extended to more general cases (e.g., HCN perturbed by N_2 or HF and H_2O perturbed by Ar) with little numerical error [Varghese and Hanson 1984; Chou *et al.* 1999, 2000].

The collisional narrowing effect is taken into account in the soft collision model [Galatry 1961] using a lineshape function given by

$$G(x',y,z) = \frac{1}{\sqrt{\pi}} \text{Re} \left(\int_0^\infty d\tau \exp \left\{ -ix'\tau - y\tau + \frac{1}{2z^2} \left[1 - z\tau - \exp(-z\tau) \right] \right\} \right), \quad (2.13)$$

where $z = P\beta / \Delta v'_D$, and β (cm^{-1}/atm) is the collisional narrowing parameter. The hard collision model [Rautian and Sobel'man 1967] is expressed by

$$P(x',y,z) = \text{Re} \left[\frac{w(x',y+z)}{1 - \sqrt{\pi}zw(x',y+z)} \right]. \quad (2.14)$$

The narrowing parameter β may be compared with the dynamic friction coefficient β_{Diff} inferred from the diffusion coefficient D_{12} [Lepere *et al.* 2001],

$$\beta_{Diff} = \frac{kT}{2\pi c M_1 D_{12}}, \tag{2.15}$$

where D_{12} is the mass-diffusion coefficient for an absorbing molecule 1 (molecular weight M_1) in a perturbing molecule 2. The diffusion coefficient can be calculated from Lennard-Jones potential parameters and has theoretical temperature dependence of $T^{1.5}$ for hard sphere collisions [Hirschfelder 1954; Lepere *et al.* 2001]. This implies the collisional narrowing parameter β has approximate temperature dependence of $T^{-0.5}$. In the limit of $M_1 \gg M_2$ or $M_1 \ll M_2$, the dynamic friction coefficient will be a good approximation for the measured β using the Galatry profile and Rautian profile, respectively. For the situations where M_1 and M_2 are not very different, this approximation is not strictly valid [Varghese and Hanson 1984; Lepere *et al.* 2001].

When z=0, both Galatry profile and Rautian profile are reduced to a Voigt profile given by Eq.(2.12). The lineshape functions used here are in the standardized form suggested by [Herbert 1974], and are normalized such that

$$\int_{-\infty}^{\infty} G(x',y,z)\,dx' = \int_{-\infty}^{\infty} P(x',y,z)\,dx' = \int_{-\infty}^{\infty} V(x',y)\,dx' \equiv \sqrt{\pi}. \tag{2.16}$$
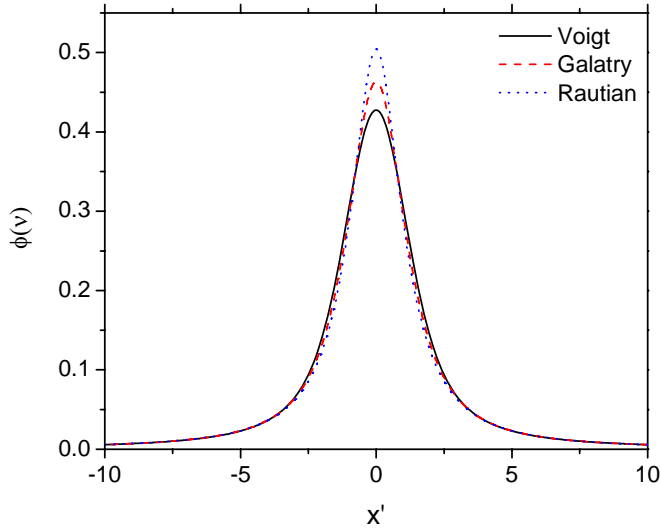
Figure 2.3   Calculated lineshapes for standardized Voigt, Galatry, and Rautian profiles (for y=z=1). Areas under each profile are equal to $\sqrt{\pi}$.

Figure 2.3 compares the simulated lineshapes for standardized Voigt, Galatry, and Rautian profiles with $y = z = 1$. With the same values of y and z, the Rautian profile exhibits a narrower feature than the Galatry profile because each hard collision destroys the velocity correlation completely while each soft collisions changes the velocity slightly. The Galatry profile is computationally more expensive than the relatively simple Voigt profile, and thus is only used in those cases where Voigt fits differ significantly from the observed data.

2.3 Direct absorption sensing strategies

Direct absorption techniques have been used extensively for nonintrusive *in situ* measurements of gas parameters such as temperature, pressure, species concentration, and flow velocity [Allen 1998]. This section will be focused on gas temperature and species concentration measurements. Gas temperature can be determined from the ratio of peak absorbance or spectrally integrated absorbance of two transitions. Thus, there are two different sensing strategies for direct absorption measurements: scanned- and fixed-wavelength techniques [Baer *et al.* 1996].

2.3.1 Scanned-wavelength technique

For scanned-wavelength direct absorption measurements, high-resolution absorption lineshapes are recorded by scanning the laser wavelength across the absorption features. Figure 5 shows an example of a laser scan. The time scale can be converted to wavelength tuning by fitting the fringe centers in the interference pattern produced by an etalon. The zero-absorption baseline (I_0) is inferred from the non-absorbing wings of the spectroscopic features. The absorption lineshape is then determined with Beer-Lambert relation (Eq.(2.1)).
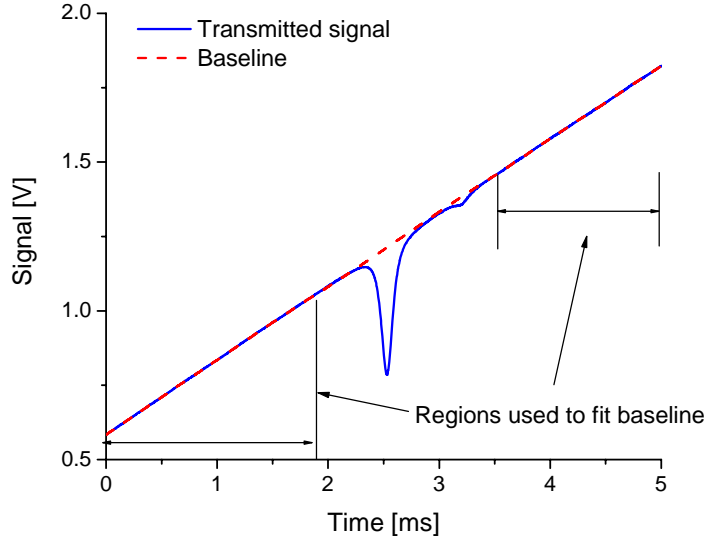
Figure 2.4   Schematic of typical scanned-wavelength direct absorption measurements.

For two-line thermometry, the integrated absorbances of two transitions are measured simultaneously with same pressure, mole fraction, and path length. Thus, their ratio simply reduces to the ratio of line strengths, which is a function of temperature only:

$$R = \frac{A_1}{A_2} = \frac{S_1(T)}{S_2(T)} = \frac{S_1(T_0)}{S_2(T_0)} \exp\left[-\frac{hc}{k}\left(E_1'' - E_2''\right)\left(\frac{1}{T} - \frac{1}{T_0}\right) \right]. \qquad (2.17)$$

As shown in Fig. 2.5, gas temperature can be determined from the ratio of the measured integrated absorbances of two isolated transitions with different temperature dependences due to differences in lower-state energy:

$$T = \frac{\left(E_1'' - E_2''\right)hc/k}{\ln R + \ln \dfrac{S_1(T_0)}{S_2(T_0)} + \left(E_1'' - E_2''\right)hc/kT_0}. \qquad (2.18)$$

Differentiating the Eq.(2.17) yields the temperature sensitivity for a given line pair:

$$\frac{dR/R}{dT/T} = \frac{hc}{k}\frac{\left(E_1'' - E_2''\right)}{T}. \qquad (2.19)$$

16
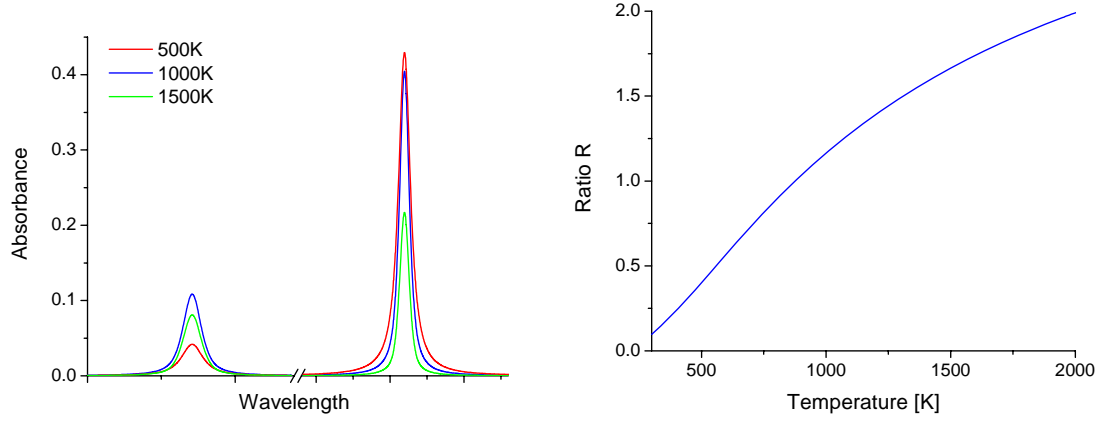
Figure 2.5　Two-line thermometry: ratio of integrated absorbance yields gas temperature.

At a specific temperature, the sensitivity increases with the difference in the lower-state energy of two transitions. This is one of the design rules in the line selection procedures for TDL sensor development.

It should be noted that this two-line thermometry actually yields a path-averaged temperature due to the assumption of a uniform gas medium along the line of sight [Liu *et al.* 2006]. The interference from cold boundary layers can be minimized in the line selection process. In cases where a significant temperature gradient (or nonuniformity) exists in the flowfield, multiple lines/paths may be utilized to provide information on the nonuniform temperature distribution [Ouyang and Varghese 1989; Sanders *et al.* 2001; Liu *et al.* 2005; Liu *et al.* 2007a].

When gas temperature is known, species concentration can be readily determined from the integrated area of one transition (Eq.(2.3)):

$$\chi_{abs} = \frac{A}{PS(T)L}.$$
(2.20)

The scanned-wavelength direct absorption technique is the most commonly used sensing strategy, and offers several advantages. First, this technique is relatively easy to implement. In addition, by integrating the absorption lineshape, this technique only needs

line strength data of the selected transitions. Line shape (broadening, narrowing) parameters are not necessary to infer temperature and concentration. However, this technique also has several disadvantages. First, the sensor bandwidth may be limited to several kHz by the wide laser scanned range needed to reach non-absorbing regions. Second, the baseline fitting procedure is prone to errors when the absorbance is low. Third, this method is less effective for high pressure applications due to lack of baseline as collisional broadening blends the features.

2.3.2 Fixed-wavelength technique

A fixed-wavelength direct absorption technique may be used to improve the sensor bandwidth up to 100 kHz [Sanders *et al.* 2000; Li *et al.* 2007d]. The laser wavelength is usually fixed at the line center of the transition. An additional non-resonant reference laser is generally combined with the probe beam to infer the baseline to account for transmission losses from beam steering and window fouling. Gas temperature can be determined from the ratio of peak absorbance. However, lineshape information (broadening, narrowing and shifting) is necessary to determine the temperature, since the ratio of peak absorbance is given by

$$R = \frac{\alpha(\nu_1)}{\alpha(\nu_2)} = \frac{S(T_1)\varphi_{\nu_1}}{S(T_2)\varphi_{\nu_2}} \,. \tag{2.21}$$

Species concentration can be determined after the temperature is known.

The fixed-wavelength direct absorption technique is more effective than the scanned-wavelength technique for high-pressure applications. However, both direct absorption methods can be prone to errors for low-absorption applications because of various noise sources such as beam steering and chemiluminescent emission. For such applications, wavelength modulation spectroscopy (WMS) can be used to improve the SNR. WMS will be discussed in detail in Chapter 4 after discussing the quantitative spectroscopy of H_2O transitions in the NIR in Chapter 3.

Chapter 3

QUANTITATIVE SPECTROSCOPY OF H_2O TRANSITIONS IN THE NIR

The development and accuracy of tunable diode laser sensors rely on knowledge of spectral parameters for the selected transitions of the target species, including linecenter position, line strength, and lower-state energy. For high-pressure and -temperature combustion gas sensing applications, an accurate understanding of the spectral lineshapes and their associated temperature dependence is needed as well.

Water vapor is a significant component of the atmosphere and a major combustion product of hydrocarbon fuels, and has a strong absorption spectrum ranging from the visible to mid-infrared [Herzberg 1991]. The overtone and combination bands of water vapor in the near-IR are especially attractive for sensor development since they overlap with the spectral region of 1.25-1.65 μm where robust, fiber-coupled, single-mode, telecom-grade diode lasers are readily available (Fig. 3.1). This chapter presents precise measurements of selected H_2O transitions in the NIR. These H_2O transitions are of particular interest owing to their use in TDL absorption sensors for measuring gas temperature and H_2O concentration in various applications, e.g., in coal-fired power plants (Section 3.4.2) and in shock tubes for studying hydrocarbon combustion mechanisms (Chapter 5 and 6).
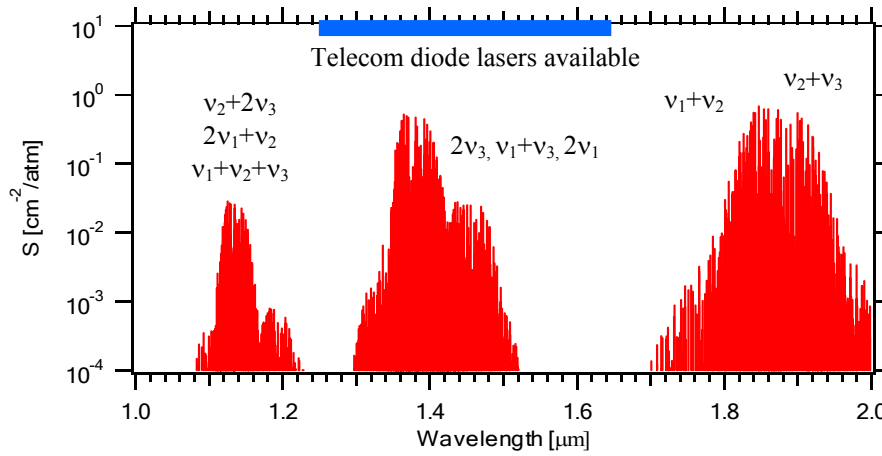
Figure 3.1   Water vapor absorption transitions in the 1-2 μm region. HITRAN 2004 database, 300 K.

3.1 Line selection for different path lengths

Selection of optimum absorption transitions is the first important step in the development of TDL sensors based on direct absorption spectroscopy. Systematic line selection criteria for absorption-based thermometry have been developed in the literature [Zhou *et al.* 2003; Zhou *et al.* 2005a]. One criterion is to ensure sufficient absorption for high SNR measurements over the expected conditions. From Eq. (2.3), the integrated area increases with absorbance. Hence, stronger absorption will reduce the uncertainty in the measured area. However, as the absorbance increases, the transmission decreases exponentially according to the Beer-Lambert relation. As shown in Fig. 3.2, less than 22% of the incident laser power is transmitted through the gas when the absorbance is larger than 1.5. The inferred absorbance near linecenter will have larger uncertainty due to the finite dynamic range and resolution of the data acquisition system. Therefore, peak absorbance between 0.05-1.5 is often preferred for practical direct absorption measurements.

Path lengths of the test facilities limit the choice of H_2O lines. For example, for short-path applications like a shock tube or a lab-scale combustor, the typical path length is ~10 cm. Strong H_2O transitions are generally preferred to achieve high SNR for such applications. For long-path applications like coal-fired power plants, the typical path

length is one hundred times longer (~ 10 m). Weaker lines are preferred to avoid low transmission near linecenter.

$$\tau_\nu = \exp(-\alpha)$$
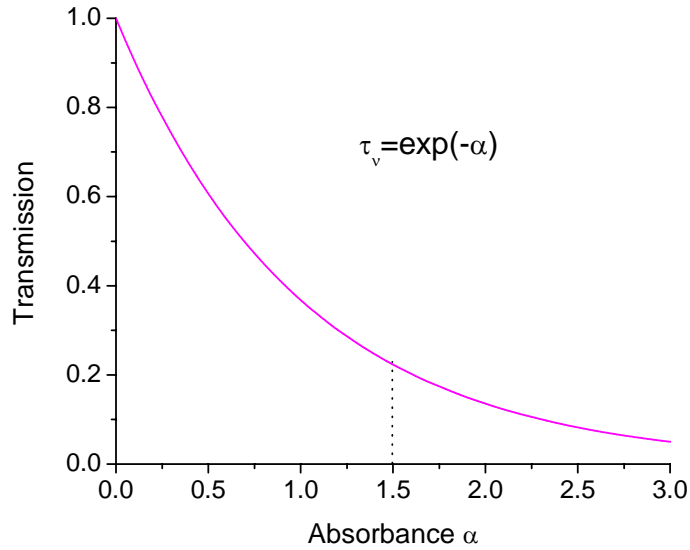
Figure 3.2 Transmission as a function of absorbance at line center.

The H_2O transitions in the 1.3-1.5 μm region are systematically analyzed to select optimum line pair for the various applications with different path lengths ranging from 10 cm to 10 m. These lines will be summarized in Section 3.3 and 3.4.

3.2 Experimental setup for quantitative spectroscopy

The HITRAN database [Rothman *et al.* 2003, 2005] provides a good reference for sensor design. However, the spectroscopic parameters of the selected transitions must be validated before use in a TDL sensor. In addition, some spectral parameters are not listed in the HITRAN database: e.g., temperature exponents for self-broadening and shift parameters, Ar-broadening and -narrowing parameters. Experiments in a well-controlled environment (e.g., heated static cell) are usually conducted to determine these important spectroscopic parameters.

3.2.1 Heated static cell

Figure 3.3 illustrates the experimental setup used to determine the spectroscopic parameters with a 3-section heated static cell (inner diameter, 4.4 cm). The same setup has been used in previous spectroscopy measurements [Liu *et al.* 2006; Liu *et al.* 2007c]. A three-zone furnace (MHI H14HT 2.5×27) with three independently adjustable heaters is used to maximize temperature uniformity in the center section of the quartz cell. The 76.2-cm center section of the cell is filled with test gas and located in the uniform-temperature region of the furnace, while the two outer sections are evacuated to avoid any interference by ambient water vapor in the region of the optical path with a temperature gradient [Liu *et al.* 2007c]. Three type-K thermocouples (Omega) with an accuracy of ±0.75% of reading are equally spaced along the center section of the heated cell to determine the temperature of gas samples. At each temperature set point in the range of 296-1200 K, the maximum temperature difference is determined to be <0.5%. The gas pressures are measured with two MKS Baratron pressure transducers (100 and 1000 Torr full scale, preheated to 45 ºC) with an accuracy of ±0.12% of reading. TDL absorption measurements are made when the measured gas pressures in the cell are stable.
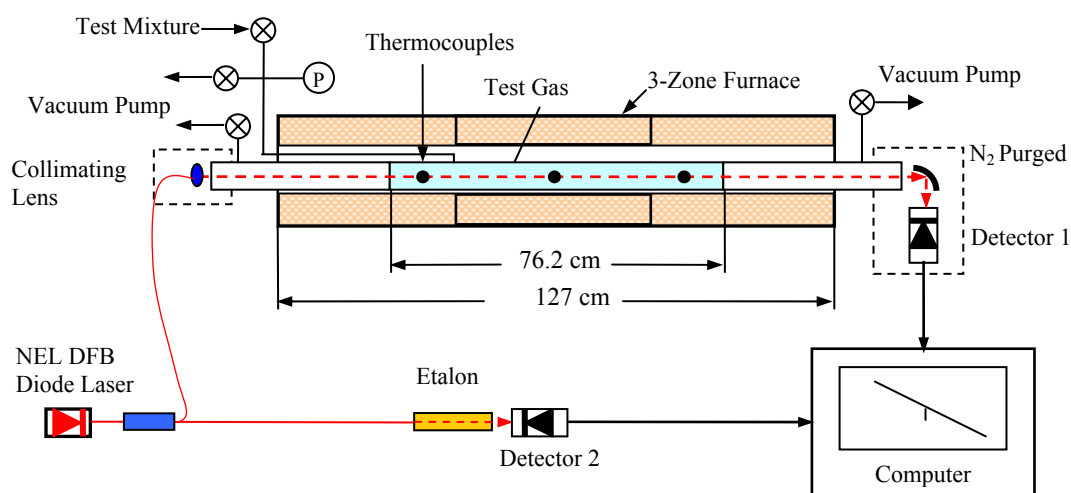
Figure 3.3   Schematic of experimental setup used for the spectroscopy measurements.

Pure water vapor is extracted from a flask containing distilled liquid water which was previously evacuated for ~15 min to remove any gaseous impurities. Controlled H_2O-Ar mixtures are made by sequentially introducing H_2O vapor and Ar into a stainless steel tank with Teflon beads to aid the stirring process. The tank is first shaken and then allowed to rest for at least 12 hours before the H_2O-Ar mixture is used for the absorption measurements.

3.2.2 TDL absorption measurement

Fiber-coupled, distributed-feedback (DFB) diode lasers operating near 1.4 μm are used, one at a time, to probe selected H_2O transitions: e.g., lines at 7185.60 and 7154.35 cm⁻¹. The spectral line width of the lasers is less than 2 MHz, according to the manufacturers' specifications [NEL website], resulting in negligible instrument broadening (comparing to the absorption line widths >1 GHz in the experiments performed). The diode lasers have a nominal output of 10 mW under typical operating conditions. Each laser is mounted in a commercial laser mount (ILX Lightwave LDM-4980) and maintained at constant temperature (ILX Lightwave LDC-3900). The laser wavelength is injection-current tuned with a linear ramp across the target absorption features.

The light from the diode laser is divided into two paths by the fiber splitter. For the first path, light is collimated into free space, transmitted through the sample gas, and focused by a spherical gold mirror onto an InGaAs detector (Thorlabs PDA 400, 10 MHz). The optics and detector are enclosed by plastic bags purged by dry N_2 to avoid absorption interference from the ambient water vapor. The windows on the gas cell are wedged to minimize interference effects as the laser wavelength is scanned [Liu *et al.* 2007c]. For the second path, the light goes through a fiber-ring etalon with a free spectral range (FSR) of 0.0277 cm⁻¹ onto a second detector to track the wavelength tuning of the laser by fitting the fringe centers in the interference pattern with a 5th-order polynomial. The absolute wavelength is calibrated by the combination of measurements using a wavemeter (Burleigh WA-1000) and the well-known positions of the strong H_2O transitions [Rothman *et al.* 2005].

The laser wavelength is tuned over a range of ~2.5 cm^{-1} at a frequency of 100 Hz. The detector signals are simultaneously sampled at 500 kHz. From the background-subtracted laser transmission I_t, the unattenuated laser intensity (the baseline) I_0 is inferred by fitting the part of scan without absorption with a third-order polynomial. The spectral absorbance is then calculated using Eq. (2.1). The lineshape of the target transition is best-fit using a Voigt or Galatry profile with the Doppler FWHM fixed at the value calculated by Eq. (2.6). The Voigt profile is calculated using numerical approximation [Whiting 1976]. The Galatry profile is computed using LabVIEW based on the FORTRAN code given by Varghese [1983]. The fitting procedure minimizes the mean-squared error between the experimental profile and the theoretical profile using a nonlinear Levenberg-Marquardt algorithm.

3.3 H$_2$O lines for short-path applications

This section presents precise measurements of line strength and self-broadening coefficient of H$_2$O transitions near 7185.60 cm^{-1} ($J'K'_{-1}K'_1 = 660 \leftarrow J''K''_{-1}K''_1 = 661$) and 7154.35 cm^{-1} ($J'K'_{-1}K'_1 = 880 \leftarrow J''K''_{-1}K''_1 = 881$) in the $\nu_1 + \nu_3$ combination band ($\nu'_1\nu'_2\nu'_3 = 101 \leftarrow \nu''_1\nu''_2\nu''_3 = 000$). These two H$_2$O transitions are of particular interest owing to their use in a new TDL absorption sensor for measuring gas temperature and H$_2$O concentration in studies of the combustion mechanisms of hydrocarbon fuels (Chapter 5 and 6). Several other H$_2$O lines suitable for shot path temperature measurements have also been characterized and will be summarized at the end of this section.

3.3.1 Line strength measurements

Figure 3.4 shows the measured spectrum of the H$_2$O transition near 7185.60 cm^{-1} in pure water vapor at the experimental conditions of *T*=1086 K and *P*=18.0 Torr. The experimental profiles are best-fit using both a Voigt profile and a Galatry profile for comparison, with the residuals (difference between data and fit normalized by peak absorbance) shown in the lower panels. It can be seen from the figure that both Voigt and

Galatry profiles can accurately describe the measured pure H_2O absorption profile. The lineshape model based on a Galatry profile yields a best fit with mean-squared error that is ~1.6 times smaller than that generated by the Voigt profile, suggesting a relatively small collisional-narrowing effect (with respect to the self broadening). The inferred line strength and self-broadening coefficient agree within 1% and 1.8%, respectively, using Voigt and Galatry profiles. Thus, the relatively simple Voigt lineshape is used in the data reduction for H_2O line strength and self-broadening coefficient measurements.
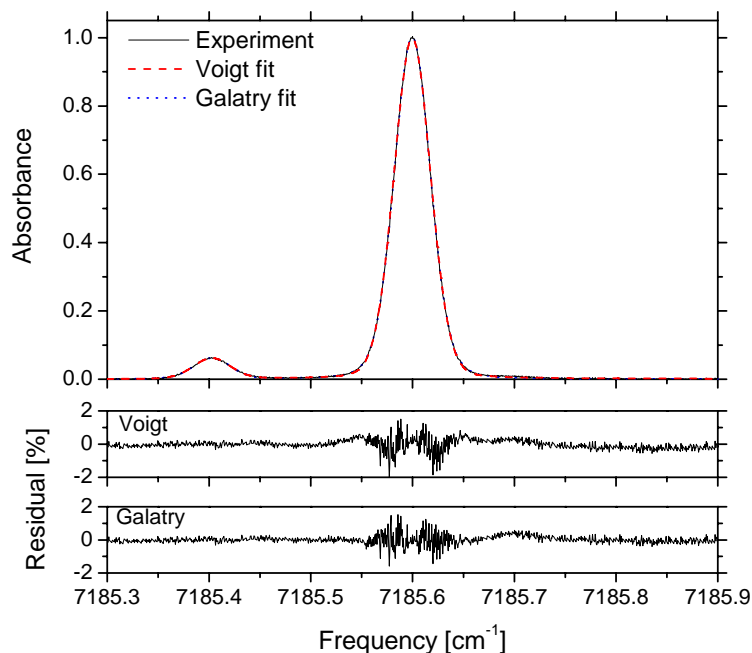
Figure 3.4   Single-scan absorption data taken at 100 Hz with pure H_2O at *P*=18.0 Torr, *T*=1086 K, and *L*=76.2 cm. Shown in the top panel are the 2-line best-fit Voigt profile and Galatry profile to the experimental data. The residuals of the fits are shown in the lower panels.

The line strength measurement procedure is illustrated in Fig.3.5 and is similar to that used in [Liu *et al.* 2007c]. For each temperature, the integrated absorbance area is first measured at 7 different pressures between 6 and 20 Torr. At each pressure, 20 measurements are conducted, and the average value of the integrated absorbance area and its standard deviation are determined and plotted in Fig. 3.5a (the error bars are too small

to be identified in the figure). Following Eq. (2.3), the line strength at this temperature is inferred from the slope of the linear fit to the data. The measured line strength at 10 different temperatures between 296 K and 1100 K is plotted in Fig. 3.5b (again the error bars are too small to be identified in the figure). These measured data are fit to Eq. (2.4) with E'' and S(296 K) as free parameters. The good agreement (within 0.1%) between the fit value of E'' and the HITRAN 2004 value confirms the spectroscopic assignment in HITRAN. With the lower state energy fixed at the HITRAN value (E''=1045.1 cm^{-1}), the line strength at the reference temperature S(296 K) is then obtained from a one-parameter best fit with an uncertainty of 0.5%. The calculated line strength from HITRAN 2004 is also shown in Fig.3.5b for comparison. The measured line strength is about 3% lower than the HITRAN 2004 value (note the uncertainty listed in HITRAN is 5-10%) [Rothman *et al.* 2005], and our result is 1.6% higher than Toth's value (who stated an uncertainty of 2%) [Toth 1994]. Table 3.1 compares the measured line strength values for H$_2$O transitions at 7185.60 cm^{-1} and 7154.35 cm^{-1} with the HITRAN database and data from Toth [1994]. The line strength for 7154.35 cm^{-1} is taken from the recent measurement by Zhou *et al.* [2005a] using a similar experiment setup in our laboratory.

(a)

(b)
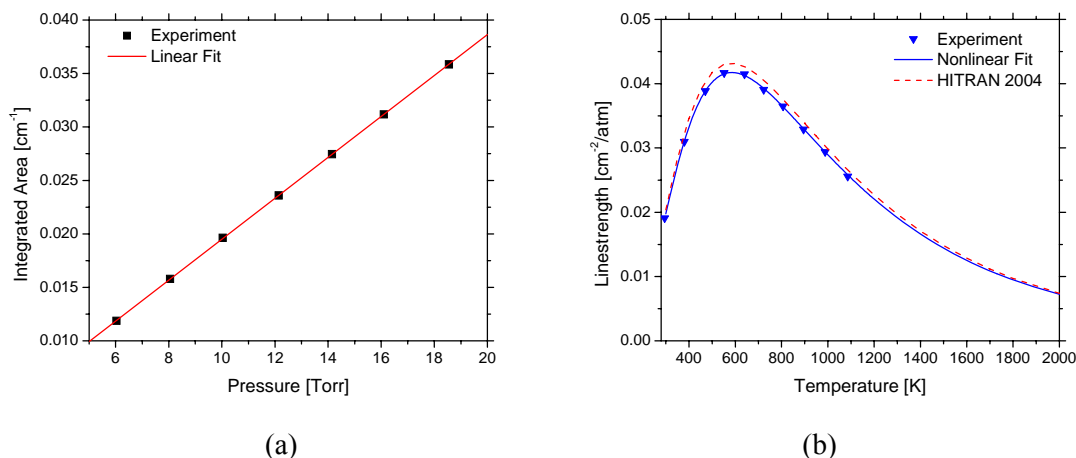
Figure 3.5   Line strength measurements for the H$_2$O transition near 7185.60 cm^{-1}: (a) the measured integrated absorbance versus H$_2$O pressure at *T*=296 K, and the linear fit used to infer the line strength; (b) the measured line strength versus temperature and the one-parameter best fit to infer the line strength at the reference temperature S(296K)=0.0191±0.0001 cm^{-2}/atm.

3.3.2 Self-broadening measurements

The self-broadening coefficient is extracted from the collisional (Lorentzian) FWHM given by the Voigt fit of the measured spectra. At a selected temperature, the values of collisional FWHM at various pressures of pure water vapor are fit to a straight line to infer the self-broadening coefficient, as shown in Fig. 3.6a. The self-broadening coefficient at the 296 K reference temperature, γ_{self}(296 K), and its temperature exponent *n* are inferred from a two-parameter best fit of the measured γ_{self} at various temperatures according to Eq.(2.9), as illustrated by Fig. 3.6b. The measured results are also compared with the HITRAN04 database in Table 3.1.

Three other H$_2$O lines (7164.90, 7417.82, and 7472.06 cm^{-1}) suitable for short path applications are also characterized and listed in Table 3.1. The uncertainties of our measured line strength and self-broadening coefficients come from the uncertainties in gas pressure (0.12%), temperature (0.75%), path length (0.5%), and statistical errors in the baseline and profile fits (0.2%). We suggest using our measured line strengths and self-broadening coefficients in future work.

(a)   (b)
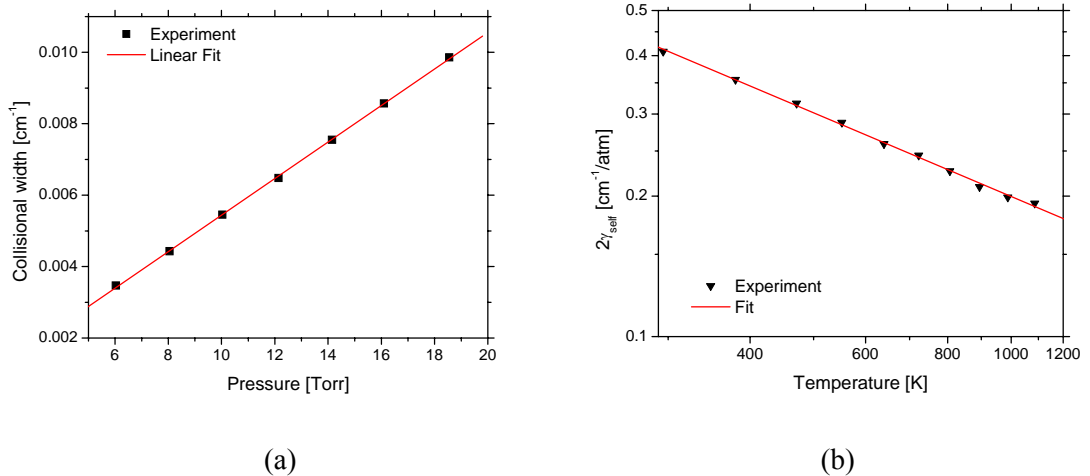
Figure 3.6   Self-broadening coefficient measurements for the H$_2$O transition near 7185.60 cm^{-1}: (a) the measured collisional FWHM versus pressure at T=296 K, and the linear fit to infer $2\gamma_{self}$; (b) the measured $2\gamma_{self}$ versus temperature, and the two-parameter best fit to infer $2\gamma_{self}$(296K)=0.410±0.003 cm^{-1}/atm and n=0.59±0.01.

Table 3.1 Comparison of line strengths and self-broadening coefficients between measurements and databases for H_2O transitions suitable for short-path applications.

v_0 [cm^{-1}]	E'' [cm^{-1}]	S(296K) [cm^{-2}/atm]/uncertainty			γ_{self}(296K) [cm^{-1}/atm]		n
		Measured	HITRAN04	Toth [23]	Measured	HITRAN04	Measured
7154.35	1789.0	3.67E-4 (<3%)	3.85E-4 (5-10%)	3.60E-4 (3%)	0.151 (<3%)	0.177 (5-10%)	0.65 (<3%)
7185.60	1045.1	1.91E-2 (0.5%)	1.97E-2 (5-10%)	1.88E-2 (2%)	0.205 (0.7%)	0.233 (5-10%)	0.59 (1.7%)
7164.90	1394.8	3.55E-3 (2%)	3.65E-3 (5-10%)	3.30E-3 (4%)	/	0.200 (10-20%)	/
7417.82	1079.1	1.07E-2 (2%)	1.07E-2 (5-10%)	1.02E-2 (2%)	/	0.300 (5-10%)	/
7472.06	2952.4	2.66E-6 (3%)	5.25E-6 (5-10%)	3.83E-6 (6%)	/	0.158 (>20%)	/

Uncertainties are given in the parentheses. Data for line 7154.35 cm^{-1} are taken from [Zhou *et al.* 2005a]

3.4 H_2O lines for long-path applications

Nine weak H_2O transitions have been chosen to enable quantitative temperature measurements in coal-fired power plants. The long path lengths (10-20 m) of the facilities limit the choice of H_2O lines for direct absorption measurements. This section presents the quantitative characterization of these nine H_2O transitions and the sample applications in coal-fired power plants through collaboration with Zolo Technologies, Inc.

3.4.1 Linestrength measurements

Line strength measurements for these lines follow the same procedure as last section. However, extra care must be taken to achieve high SNR absorption measurements in the heated cell. In particular, long path length is needed for quantitative measurements of these weak H_2O transitions. A 5-pass configuration is used to establish a long path length (L=381 cm) in the heated cell, as shown in Fig. 3.7. Each mirror captures light from single pass to suppress potential interference. This 5-pass alignment is validated by absorption measurement with well-known strong H_2O lines.
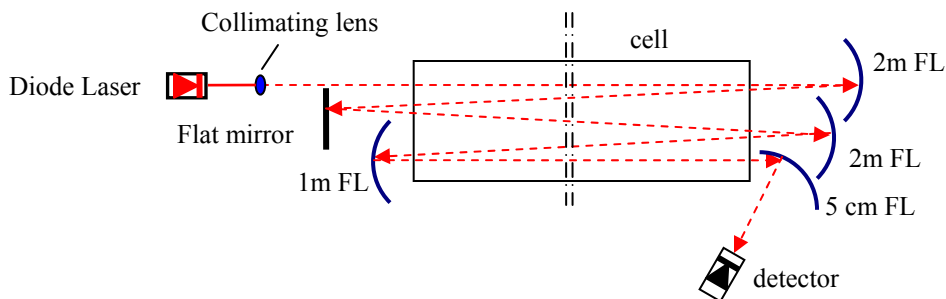
Figure 3.7 5-pass arrangement used to increase the path length in heated cell (FL= focal length).

Figure 3.8 compares the measured spectra in the heated cell for one laser scan with HITRAN/HITEMP simulations with pure H_2O at 1095 K and 20.75 Torr. Position of the strong line at 7411.38 cm^{-1} is identified in HITRAN and verified with a wavemeter. The wavelength scale for the remainder of laser scan is established with the etalon transmission signal. It is clear that lines B and D are present in HITRAN database, while lines A and C are not. There are some additional lines predicted by HITEMP database, but they are not at the observed positions. The measured line strength and line center data for the selected 9 H_2O lines are summarized in Table 3.2.
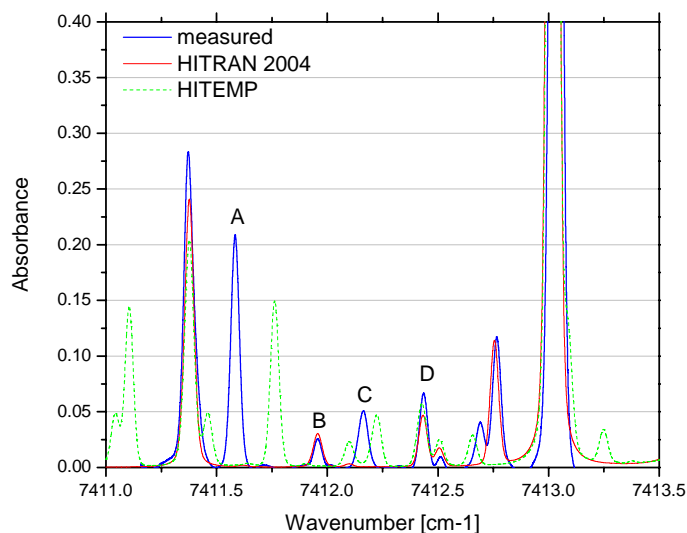
Figure 3.8 Comparison of measured spectra (Lines A-D) with HITRAN 2004/HITEMP simulations. Pure H_2O, T=1095 K, P=20.75 Torr, L=381 cm.

Table 3.2   Spectroscopic data for H_2O transitions for long-path gas temperature sensors

Line	Measured		E" [cm^{-1}]	HITRAN2004/HITEMP		
	Linecenter [cm^{-1}]	S(296K) [cm^{-2}/atm]		Linecenter [cm^{-1}]	S(296K) [cm^{-2}/atm]	E" [cm^{-1}]
A	7411.59	6.93E-8	3655.53	HITEMP: 7411.761	4.14E-08	3655.53
				7411.767	1.38E-08	3655.53
B	7411.96	6.56E-5	1201.92	HITRAN04:7411.957	7.50E-05	1201.92
C	7412.17	6.97E-7	2631.30	HITEMP: 7412.206	1.70E-07	2631.30
				7412.227	5.11E-07	2631.29
D	7412.43	3.96E-6	2254.28	HITRAN04:7412.433	1.22E-05	1806.67
				7412.755	6.14E-06	2254.28
E	7265.08	8.20E-8	3381.66	HITEMP: 7265.062	5.35E-08	3381.66
F	7169.22	2.18E-4	1282.92	HITRAN04:7169.219	2.70E-04	1282.92
G	7169.48	2.22E-5	1524.85	HITRAN04:7169.485	2.80E-05	1524.85
H	7169.64	2.38E-11	5246.80	HITEMP: 7169.634	5.10E-12	5246.80
I	7169.83	8.00E-6	2398.38	HITRAN04:7169.826	1.75E-05	2398.38

Lines A-D are covered by one laser scan; Lines F-I are covered by another laser scan.

3.4.2 Sample applications in coal-fired power plants

A fiber-coupled diode laser sensor system based on direct absorption spectroscopy technique has been developed to non-intrusively measure gas temperature and water vapor concentration in coal-fired power plants with the goal of improving combustion efficiency, reducing emissions, and ensuring consistent operation. This work is built on previous work of Teichert *et al.* [2003] who demonstrated qualitative temperature measurements on a single path using a 813 nm Fabry-Perot laser, and is realized through collaboration with Zolo Technologies, Inc. [Zolo website].

Figure 3.9 shows the schematic of the TDL sensor. Three fiber-coupled DFB diode lasers near 1400 nm are multiplexed for simultaneous measurements of absorption at five H_2O transitions along a common path in the combustion chamber. Lines B, C, E, G, and H in Table 3.2 are selected for the sensor considering the absorption level in the power

plants and interference from neighboring absorption lines. The fiber-coupled sensor facilitates remote control and multiple path/level measurements, and protects lasers/detectors. In addition, wavelength multiplexing enables simultaneous measurements of temperature, H_2O, CO, CO_2, and O_2 along a common path by including additional lasers for CO (~1550 nm), CO_2 (~1550 nm) and O_2 (760 nm).
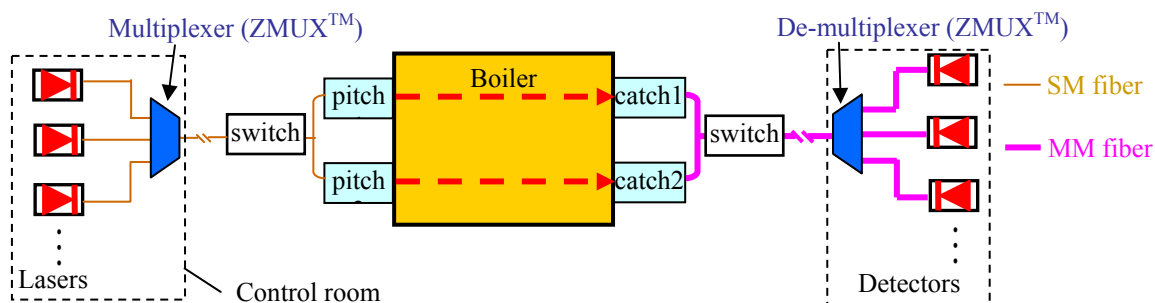
Figure 3.9   Schematic of the TDL sensor for coal-fired power plants. (SM = single mode, MM = multi-mode).

The boiler is a very harsh environment for TDL measurements. Coal dust and fly ash block laser beam transmission and cause signal fluctuations. Turbulence in the boiler causes beam steering. In addition, there is bright background emission from the coal combustion zone. To mitigate these effects, extra care is taken by Zolo Technologies Inc in the optical design of the TDL sensor system. The laser beam is expanded to 1 inch diameter to maximize the transmission. The windows are purged by air to avoid fouling by dust. Multi-mode fibers are used on the catch side to reduce mode noise. In addition, the Zolo de-multiplexer acts as a 1 nm band-pass filter to minimize the effect of background emission on detectors. The laser wavelengths are scanned at 10 kHz to minimize signal fluctuations during one scan. Laser transmission data are then averaged (10 s) to improve SNR.

The sensor system was first demonstrated on a Tennessee Valley Authority (TVA) 280 MW coal fired-power plant. The facility is tangentially fired with a combustion chamber cross section of 9.2 m×7.2 m. Figure 3.10 shows the schematic of the field

measurements. Three different levels (SOFA, bull nose, and economizer) are probed with up to 6 paths on one level to provide spatially-resolved information.
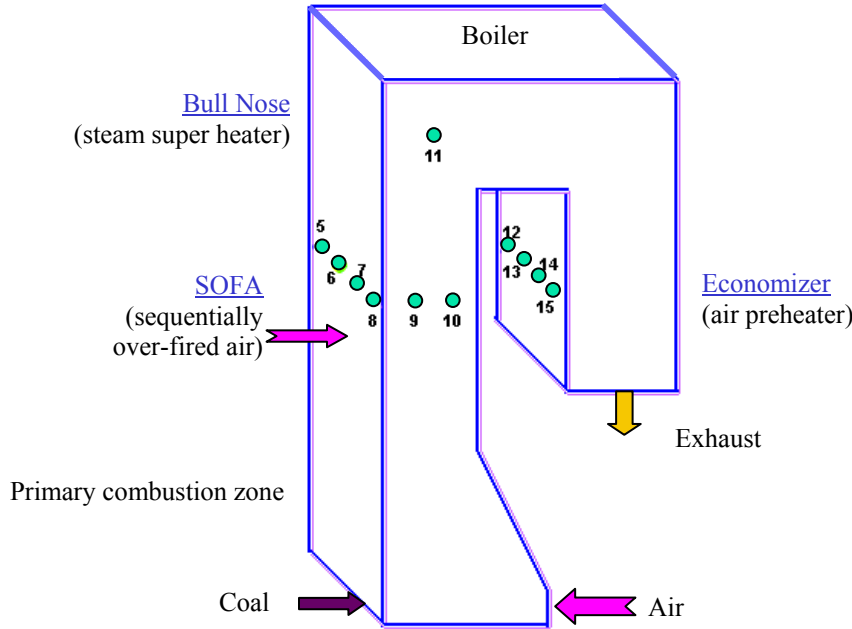
Figure 3.10   Field measurements in a TVA coal-fired power plant. (Through collaboration with Zolo Technologies, Inc.).

Figure 3.11 shows the sample H_2O absorbance data taken in the field measurement. The absorbance data is seen to have a good SNR. Scanned-wavelength strategy allows measurement with low transmission (~1%). The measured absorbance data are best fit using a Voigt profile, with residual shown in the upper panel. The inferred absorption areas from different transitions can be used to determine gas temperature and H_2O concentration using the Boltzmann plot (Fig. 3.12), since

$$\ln\left(\frac{A}{S_0}\right) = \ln\left[Px_{H_2O}L\frac{Q(T_0)T_0}{Q(T)T}\right] + \ln\left[\frac{1-\exp(-\frac{hcv_0}{kT})}{1-\exp(-\frac{hcv_0}{kT_0})}\right] - \frac{hcE''}{k}\left(\frac{1}{T}-\frac{1}{T_0}\right). \quad (3.1)$$

For H_2O lines in the NIR, the second term on the right hand side of the above equation is essentially small enough (~-0.001) to be neglected. Thus, line-of-sight temperature can be determined from the slope of $\ln(A/S_0)$ versus E''. H_2O concentration can then

be inferred from the intercept of the Boltzmann plot. The use of five H_2O absorption lines increases the sensor reliability compared with a two-line thermometry.
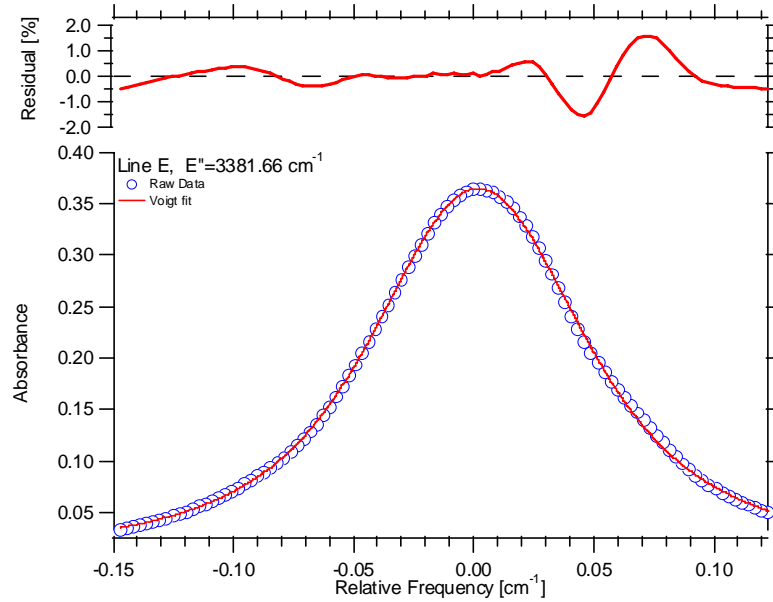
Figure 3.11   Sample H_2O absorbance data from field measurements in a TVA power plant. Laser scan rate 10 kHz, 10 s averaging, location: SOFA, path 5.
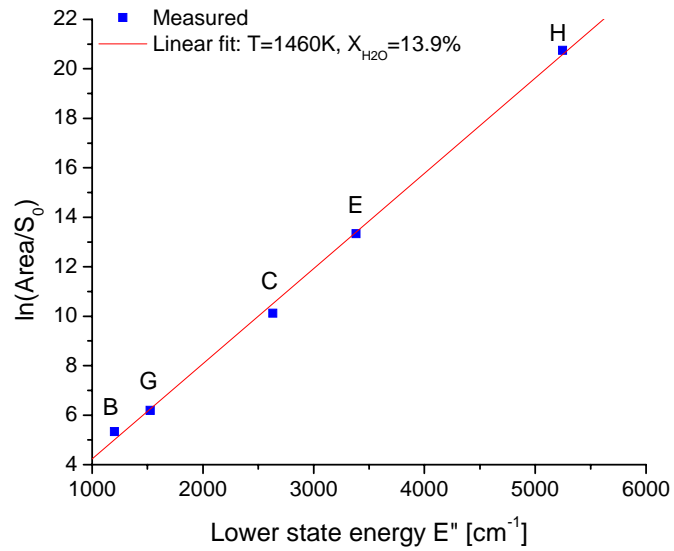
Figure 3.12 Boltzmann plot of the measured H_2O absorption area for path 5 (SOFA) to infer temperature and H_2O concentration.
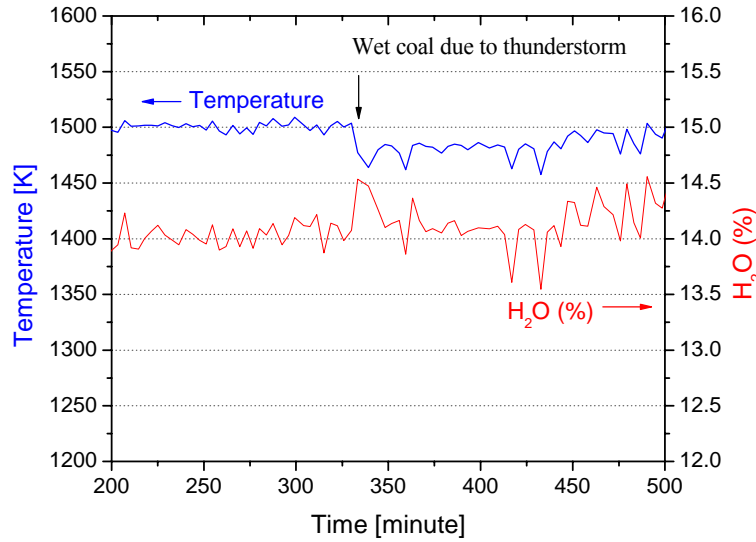
Figure 3.13 Measured temperature and H_2O concentration for path 5 (SOFA) shows the effect of thunderstorm.

Figure 3.13 shows the time history of measured temperature and H_2O concentration for a time span of 300 minutes. The temperature drop (~25 K) is due to wet coal induced by thunderstorms. Figure 3.14 shows the time history of measured temperature and H_2O at different levels in the power plant. Good sensor performance is confirmed by the stable measurement results (temperature scatter <10 K for all paths). Measured temperature of path 11 is in good agreement with acoustic pyrometer measured value (~1500 K, 2-hour averaged) at the same level. Path 6 has higher temperature and lower H_2O concentration than path 11, since combustion is mostly completed before path 11. Path 15 has larger scatter in H_2O concentration due to unstable optics mounted on less rigid walls around the economizer. Path 15 also has lower H_2O concentration due to air leakage into the boiler since pressure inside boiler is lower than ambient atmosphere. Multiple-path measurement on the same level may be used to provide approximate nonuniform distribution of temperature and H_2O concentration using coarse tomography [Zolo website; Zhang *et al.* 2001].
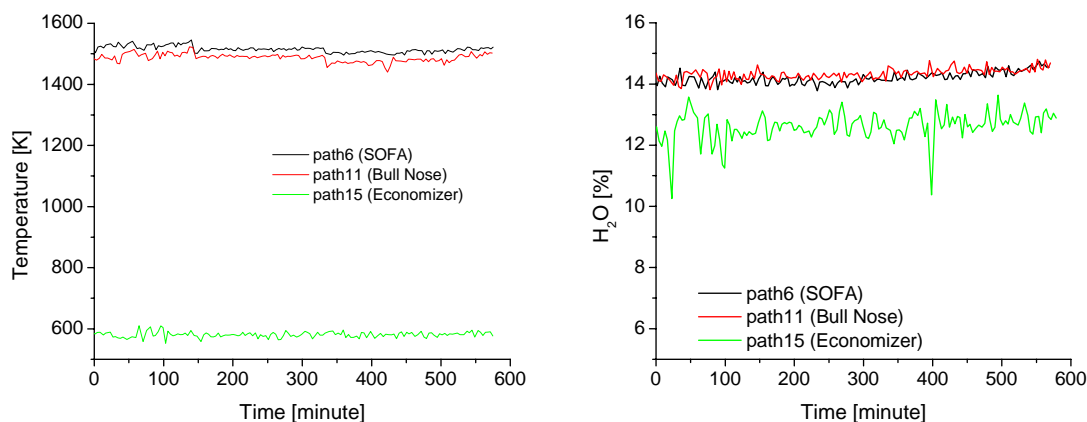
Figure 3.14 Measured temperature and H_2O concentration at different levels in a TVA power plant.

3.5 Ar-broadened H_2O lineshapes

This section presents precise measurements of Ar-broadened absorption lineshapes of two H_2O transitions near 7185.60 and 7154.35 cm^{-1}. These measurements provide a critical spectroscopic database for rapid TDL absorption measurements of temperature and H_2O concentration in Ar-diluted mixtures being used to study combustion kinetics mechanisms (Chapter 5 and 6).

3.5.1 Collisional broadening measurements

To infer the Ar-broadening coefficients for the target transitions, the absorption spectra of H_2O-Ar mixtures at pressures of 200-830 Torr are measured at a series of temperatures between 296 K and 1100 K. Fig. 3.15 plots the Ar-broadened H_2O lineshape near 7185.60 cm^{-1} (P=827 Torr, T=1097 K, 1% H_2O in Ar). The residual of the best 2-line Voigt fit reveals a systematic discrepancy with the experimental data. The observed maximum discrepancy changes with pressure (from 2.3% at 200 Torr to 4.1% at 827 Torr, T=1097 K) and temperature (from 1.5% at 296K to 4.1% at 1097 K, P~827 Torr).

This observation is consistent with the discussion by Varghese and Hanson [1984]. The gull-wing like feature is typically found in the residuals when a Dicke-narrowed lineshape is fit by a Voigt lineshape, and suggests a strong collisional narrowing effect on the H_2O absorption lineshapes by Ar-H_2O collisions [Varghese 1983; Chou *et al.* 1999; Lepere *et al.* 2001]. Lineshape models based on the Galatry and Rautian profile yield best fits with mean-squared error that is ~15 times smaller than that generated by the Voigt profile.
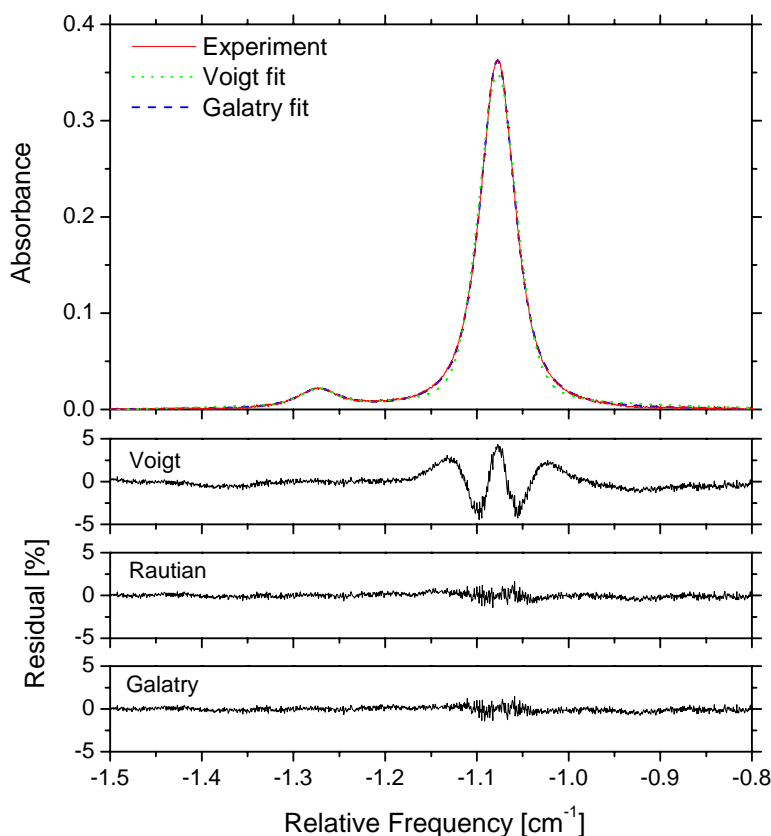
Figure 3.15   Measured Ar-broadened H_2O lineshape of the transition near 7185.60 cm^{-1} with 1% H_2O in Ar, P=827 Torr, and T=1097 K. The gull-wing like feature in the Voigt fit residual suggests a strong collisional narrowing effect. Both Galatry and Rautian profiles reduce the mean-squared error of the fit by ~15 times compared to that of the Voigt profile fit.
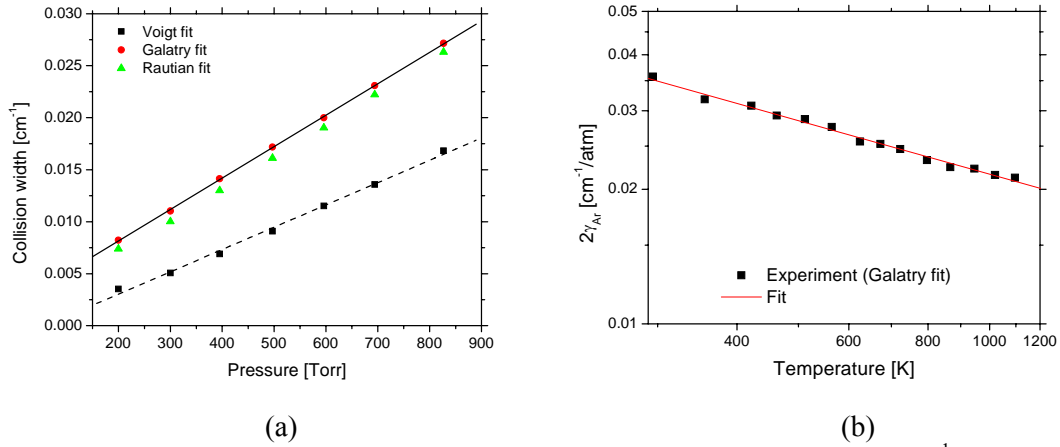
Figure 3.16   Ar-broadening coefficients for the H_2O transition near 7185.60 cm^{-1}: (a) collisional FWHM for various pressures determined by Galatry, Rautian and Voigt fits, T=1097 K; (b) the measured $2\gamma_{Ar}$ versus temperature, and the two-parameter best fit used to infer $2\gamma_{Ar}$(296K)=0.0351±0.0004 cm^{-1}/atm and n=0.40±0.01.

The collisional-narrowing effect on the Ar-broadened H_2O lineshape is readily observable near atmospheric pressure due to the relatively weak pressure broadening induced by Ar-H_2O collisions [Nagali *et al.* 2000]. As a result, the determination of the collisional width from the best Voigt fit to the measured profile underestimates the collisional width by up to 55%. Collisional widths extracted using Voigt, Rautian, and Galatry profiles are plotted in Fig. 3.16a for the Ar-broadened H_2O transition at 7185.60 cm^{-1}. The results from the Galatry and Rautian fits show strong linear pressure dependence while values from Voigt fits deviate from linear dependence, again illustrating the need to include collisional narrowing in the analysis [Chou *et al.* 1999].

The Ar-broadening coefficient can be determined from the slope of the linear fit to the measured collisional width. The inferred values for γ_{Ar}(1097 K) from Fig. 3.16a using the Galatry profile and the Rautian profile agree within 0.6%. Although the H_2O concentration is only 1% in the test mixture, the strong H_2O self-broadening effect contributes significantly to the total collisional widths. The contribution of self-broadening is incorporated in the Ar-broadening coefficient analysis using Eq. (2.8) with the γ_{self} values listed in Table 3.1. Note that 3% uncertainty on the γ_{self} value introduces

only 0.3% uncertainty on the Ar-broadening parameter. The Ar-broadening coefficient at the 296 K reference temperature, γ_{Ar}(296 K), and its temperature exponent n are inferred from a two-parameter best fit of the measured γ_{Ar} at various temperatures according to Eq.(2.9), as illustrated by Fig. 3.16b using the Galatry lineshape. For the H_2O line at 7185.60 cm^{-1}, our measured γ_{Ar}(296 K) value is in good agreement (within 8%) with the measured value (0.0192±0.0004 cm^{-1}/atm) from Lepere *et al.* [2001]. Our measured results for Ar-broadening coefficient using Voigt and Galatry profiles are tabulated in Table 3.3. Note that γ_{Ar} is ~45% of γ_{air} [Rothman *et al.* 2005], and ~10% of γ_{self} for the two investigated H_2O transitions. The Ar broadening inferred with a Voigt fit is comparable to that with a Galatry fit at room temperature, but is much smaller at high temperatures due to collisional narrowing.

Table 3.3 Measured Ar-induced broadening, narrowing and shift coefficients and their temperature dependences for two H_2O transitions.

v_0 [cm^{-1}]	E'' [cm^{-1}]	Voigt profile		Galatry profile					
		γ_{Ar}(296K) [cm^{-1}/atm]	n	γ_{Ar}(296K) [cm^{-1}/atm]	n	β_{Ar}(296K) [cm^{-1}/atm]	N	δ_{Ar}(296K) [cm^{-1}/atm]	m
7185.60	1045.1	0.0185 (±0.0008)	0.70 (±0.01)	0.0176 (±0.0004)	0.40 (±0.01)	0.0407 (±0.0004)	0.59 (±0.02)	-0.0213 (±0.0003)	1.07 (±0.02)
7154.35	1789.0	0.0147 (±0.0005)	0.79 (±0.04)	0.0145 (±0.0004)	0.36 (±0.02)	0.0343 (±0.0005)	0.56 (±0.02)	-0.0241 (±0.0005)	1.11 (±0.03)

Uncertainties are given in the parentheses.

3.5.2 Collisional narrowing measurements

Since the collisional narrowing effect is observable over the investigated temperature (296-1100 K) and pressure range (200-830 Torr), it is important to understand how the collisional narrowing parameter changes with pressure and temperature. Fig. 3.17a plots the dimensionless collisional narrowing parameter z given by the Galatry fit at various pressures (T=1097 K) for the Ar-broadened H_2O transition near 7185.60 cm^{-1}. The linear dependence with pressure is in good agreement with the theoretical prediction [Varghese and Hanson 1984; Chou *et al.* 1999]. The narrowing parameter inferred by fitting the

same set of spectra with a Rautian profile (hard collision model) is different (up to 40%) from the value from Galatry (soft collision model) fits because of the different definitions of the narrowing parameter in these two models. The fit results with the Rautian profile deviate from linear pressure dependence, illustrating the benefit of using the Galatry profile in the data analysis to include Dicke narrowing. Thus, for this collision partner, the Galatry profile is preferred for our test conditions.

(a) (b)
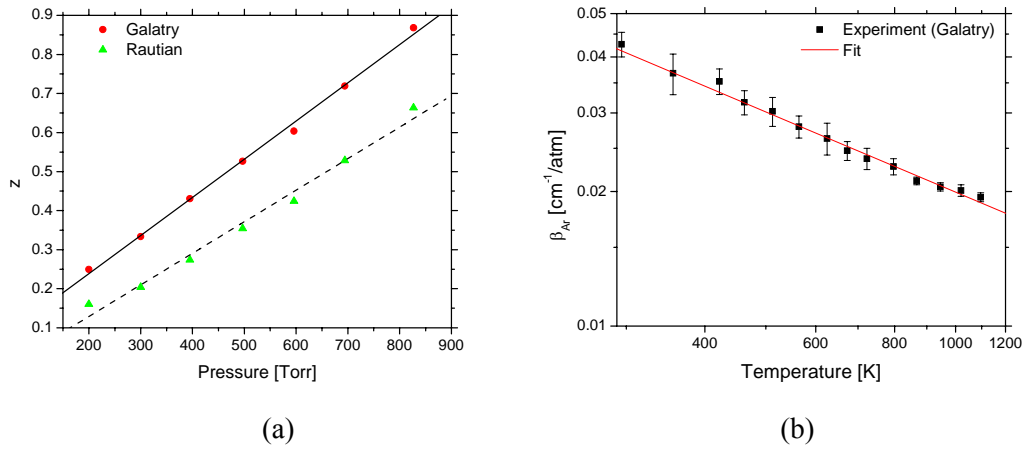
Figure 3.17   Collisional narrowing parameters for the Ar-broadened H_2O transition near 7185.60 cm^{-1}: (a) dimensionless narrowing parameter z for various pressures determined by Galatry fit and Rautian fit at T=1097 K, and their linear fits; (b) the measured β_{Ar} using a Galatry profile versus temperature, and the two-parameter best fit used to infer β_{Ar}(296K)=0.0407±0.0004 cm^{-1}/atm and N=0.59±0.02.

The Ar collisional narrowing parameter at each temperature, β_{Ar}, can be extracted from the slope of the linear fit. It is worth noting that the Galatry function profile has one more variable (narrowing parameter) than the Voigt profile, thus the Galatry fit is computationally more expensive and less robust. The inferred collisional narrowing parameter has larger scatter, especially at lower temperatures (296-400 K) where the Dicke narrowing contribution is small. The measured β_{Ar} are plotted in Fig. 3.17b and exhibit temperature dependence in a similar form to Eq. (2.9). This behavior was also observed in the temperature dependence of He narrowing parameters measured for the R(0) line in the ^{13}CO fundamental band by Henry *et al.* [2002]. The collisional narrowing parameter at the reference temperature β_{Ar}(296 K) and its temperature exponent N are

inferred from a two-parameter best fit analogous to the broadening coefficient. The measured results are also listed in Table 3.3. For the H_2O line at 7185.60 cm^{-1}, our measured β_{Ar}(296 K) is in excellent agreement (within 1.8%) with the measured value (0.040±0.005 cm^{-1}/atm) by Lepere *et al.* [2001] also using a Galatry profile. In addition, our measured values of β_{Ar}(296 K) for both H_2O lines agree reasonably well with the dynamic friction coefficient β_{Diff}(296 K)=0.032 cm^{-1}/atm deduced from Eq. (2.15). The difference between the measured β_{Ar} and β_{Diff} may be reduced by using more advanced line profile models to account for the speed-dependent collisional broadening [Pine and Ciurylo 2001; Wehr *et al.* 2006]. The ratio of our measured collisional broadening and narrowing parameter can be calculated as

$$r = y / z = \gamma_{Ar} / \beta_{Ar} \propto T^{0.19}.$$ (3.2)

The ratio *r* is only weakly dependent on temperature, as predicted by theory [Varghese 1983; Varghese and Hanson 1984].

3.5.3 Line shift measurements

For fixed-wavelength absorption sensing, the linecenter positions are also important. Figure 3.18a plots the relative linecenter position of Ar-perturbed H_2O transition at 7185.60 cm^{-1} (T=296 K). The absorption spectra are consecutively recorded at different pressures over a time period of ~15 minutes for each temperature setting. The stability of the laser wavelength is assured by the linear pressure dependence of the inferred linecenter position. Note that Voigt and Galatry fits yield the same linecenter position. The Ar-induced shift coefficient is determined from the linear fit to the measured linecenter position [Liu *et al.* 2007b]. The small self-pressure shift is neglected here. The Ar-induced shift coefficient at reference temperature δ_{Ar}(296 K) and its temperature exponent *m* are inferred from a two-parameter best fit, as illustrated by Fig. 3.18b. The measured results are also listed in Table 3.3.

(a)   (b)
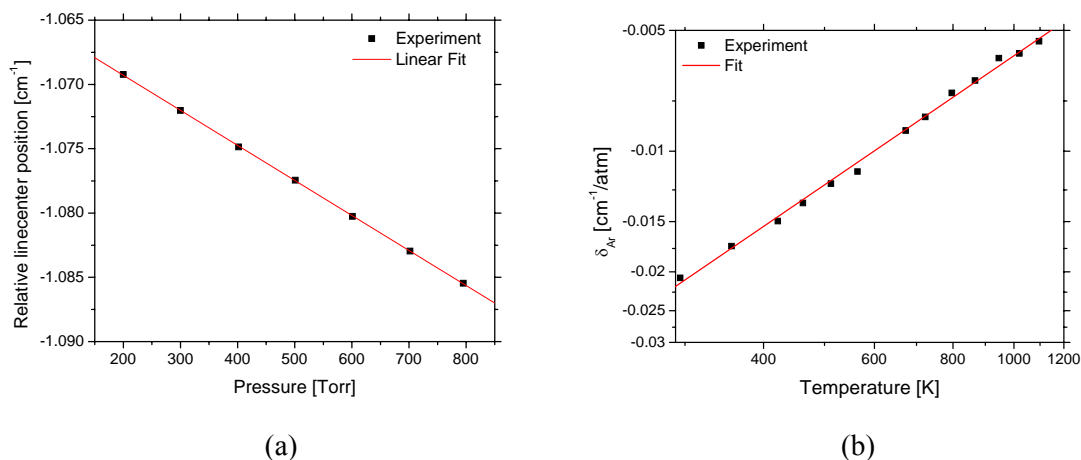
Figure 3.18 Ar-induced shift for the H_2O transition near 7185.60 cm^{-1}: (a) the measured relative position for various pressures, T=296 K; (b) the measured δ_{Ar} versus temperature, and the two-parameter best fit used to infer $\delta_{Ar}(296K)=0.0213\pm0.0003$ cm^{-1}/atm and m=1.07±0.02.

The uncertainties of our measured Ar-induced broadening, narrowing and shift coefficients are mainly from the uncertainties in the Galatry profile fit and the slopes of the measured FWHM or z at various pressures. Uncertainties in H_2O concentration (1%) in the test mixture, gas pressure (0.12%), temperature (0.5%), and pathlength (0.5%) introduce negligible errors.

Chapter 3

Chapter 4

WAVELENGTH MODULATION SPECTROSCOPY

The last two chapters discussed direct absorption techniques and presented a sample application in coal-fired power plants. In general, direct absorption methods are prone to errors for low-absorption applications and less effective for high-pressure applications. Wavelength modulation spectroscopy (WMS), as an extension of absorption spectroscopy, is a well-known technique for improving the SNR and is suitable for high pressure applications. This chapter extends the WMS theory to include real diode laser performance, especially useful for large modulation depth for TDL absorption measurements in high-pressure gases (e.g., IC engines). In these applications, large modulation depths are required for optimum detection of molecular absorption spectra blended by collisional broadening or dense spacing of the rovibrational transitions. Diode lasers have a large and nonlinear intensity modulation when the wavelength is modulated over a large range by injection current tuning. In addition to characterizing this intensity modulation, other laser performance parameters are measured including the phase shift between the frequency modulation and intensity modulation. Following published theory, these parameters are incorporated into an improved model of the WMS signal. The influence of these non-ideal laser effects is then investigated via wavelength-scanned WMS measurements as a function of bath gas pressure on rovibrational transitions of water vapor near 1388 nm.

4.1 Introduction

WMS theory began some forty years ago when Wilson [1963] employed numerical integration to obtain the first three harmonics for Gaussian and Lorentzian absorption

lineshapes. Arndt [1965] developed an analytical solution based on Fourier analysis for all harmonics of a Lorentzian lineshape, with explicit expressions for the 1*f* and 2*f* components. Reid and Labrie [1981] performed the first experimental TDL WMS experiments and measured the second harmonic signals for Lorentzian, Voigt, and Gaussian lineshapes. However, all these early approaches assumed the laser intensity to be independent of laser frequency, and thus are only suitable for small modulation depths when injection current tuned diode lasers are used for the light source.

There is an extensive literature on TDL WMS. This chapter will not attempt further general review, but will focus attention on extending TDL WMS to the large modulation depths needed for measurements with blended or strongly broadened transitions. Such spectra are found for large polyatomic molecules with densely spaced spectra or from smaller target molecular species at high pressures where spectra are broadened and blended by collisional broadening. Fig. 4.1 illustrates absorption of 1% water vapor in air as a function of pressure near 7204 cm^{-1}. Even at atmospheric pressure the three transitions near 7204 cm^{-1} are blended, and pressures of 20 atmospheres blend features more than 5 cm^{-1} away. Optimal WMS detection of such features requires large modulation depths.
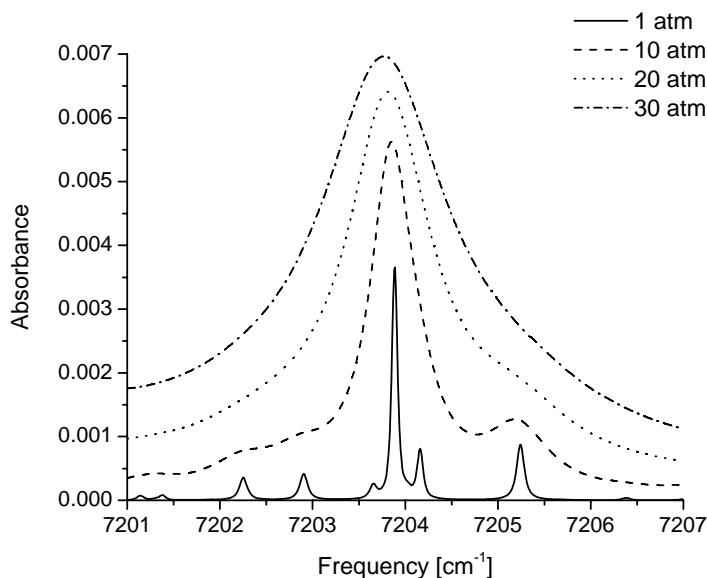
Figure 4.1   Spectral simulation of 1% H_2O in air at 1000 K, 1 cm path length.

Typical TDL WMS is performed by modulating the laser wavelength (frequency) with sinusoidal injection current [Philippe and Hanson 1993; Kluczynski *et al.* 2001a, 2001b; Schilt *et al.* 2003], which produces a simultaneous modulation of the laser intensity. We show here that quantitative TDL WMS with large modulation depths requires consideration of diode laser performance characteristics including simultaneous frequency modulation (FM) and intensity modulation (IM), the phase shift between FM and IM, and nonlinear IM.

A number of refinements to WMS models have been made previously in the literature to include these effects. Philippe and Hanson [1993] extended WMS theory to account for linear laser intensity modulation, and numerically calculated the 1*f* and 2*f* signals by using a Fourier decomposition of a Voigt profile. Kluczynski *et al.* [2001a] derived an expression to include the effect of the FM/IM phase shift for WMS with frequency-doubled light. Independent of their research and using a slightly different formalism, Schilt *et al.* [2003] developed a theoretical model of WMS for a Lorentzian lineshape in the general case of combined IM and FM with an arbitrary FM/IM phase shift. Recently, Gharavi and Buckley [2005] considered the intensity nonlinearity for a low-frequency current ramp used to tune the laser wavelength. This nonlinearity also can be empirically accounted for by performing polynomial fits to the non-absorbing portions of the laser scans [Liu *et al.* 2004a]. Using Fourier analysis, Kluczynski and Axner [1999] developed a general theoretical description of WMS which includes the effect of the FM/IM phase shift, the nonlinear IM associated with the sinusoidal current modulation, and wavelength-dependent transmission. However, their theoretical approach must be simplified and extended for practical gas sensing applications. To our knowledge, no previous work has been done on the implementation of large-modulation-depth WMS to include the effects of real diode laser performance parameters on the WMS signal.

In this chapter, large-modulation-depth WMS with 2*f* detection is extended, following the theoretical work of Kluczynski and Axner [1999], to account for the real diode laser characteristics of FM/IM phase shift and a nonlinear IM. Their equations for the amplitude components of the 2*f* signal are rewritten to provide the magnitude of the 2*f*

signal, thereby eliminating the dependence of the signal on the detection phase. To test the extended WMS theory, TDL WMS validation experiments are performed using pressure-broadened water vapor rovibrational transitions near 1388 nm.

4.2 WMS including real diode laser performance

Following the general theory of Kluczynski and Axner [1999], we rewrite the equations for the WMS signal into a form providing the magnitude of the 2*f* signal. This allows direct comparison with laboratory measurements using a lock-in amplifier. The diode laser injection current is sinusoidally modulated with angular frequency $\omega = 2\pi f$ to produce laser frequency modulation

$$v(t) = \overline{v} + a\cos(\omega t) , \tag{4.1}$$

where $\overline{v}$ is the center laser frequency and a is the modulation depth. The diode laser intensity is simultaneously modulated with an FM/IM phase shift [Philippe and Hanson 1993; Kluczynski and Axner 1999], and the instantaneous laser intensity, $I_0(t)$, varies nonlinearly with the injection current:

$$I_0(t) = \overline{I_0}[1 + \underbrace{i_0\cos(\omega t + \psi_1)}_{1f\ term} + \underbrace{i_2\cos(2\omega t + \psi_2)}_{2f\ term}] . \tag{4.2}$$

The average laser intensity at $\overline{v}$ is given by $\overline{I_0}$, i_0 is the linear (1*f*) and i_2 the nonlinear (2*f*) intensity modulation amplitude (both normalized by $\overline{I_0}$), while ψ_1 is the FM/IM phase shift and ψ_2 the phase shift of the nonlinear IM. Eq. (4.2) could be generalized to include higher order harmonics, but our experimental characterization of commercial diode lasers shows the intensity modulation is well described by a combination of 1*f* and 2*f* terms (Section 4.3).

From the Beer-Lambert relation (Eq.(2.1))

$$\tau(v) = \exp\left[-\alpha(v)\right] = \exp\left[-P\chi_i L\sum_j S_j\varphi_j\right], \tag{4.3}$$

where P [atm] is total gas pressure, χ_i is the mole fraction of the absorbing species, S_j [cm^{-2}/atm] and φ_j [cm] are the line strength and lineshape function of jth absorption feature. The summation accounts for the overlap of adjacent features, which is exacerbated by collisional broadening at higher pressures (Fig. 4.1). The transmission coefficient is a periodic even function in ωt, and can be expanded in a Fourier cosine series:

$$\tau\left(\overline{v} + a\cos(\omega t)\right) = \sum_{k=0}^{\infty} H_k\left(\overline{v}, a\right)\cos\left(k\omega t\right), \tag{4.4}$$

where the functions $H_k\left(\overline{v}, a\right)$ are given by

$$H_0\left(\overline{v}, a\right) = \frac{1}{2\pi}\int_{-\pi}^{\pi}\tau\left(\overline{v} + a\cos\theta\right)d\theta, \tag{4.5}$$

$$H_k\left(\overline{v}, a\right) = \frac{1}{\pi}\int_{-\pi}^{\pi}\tau\left(\overline{v} + a\cos\theta\right)\cos k\theta d\theta. \tag{4.6}$$

For $2f$ detection, a lock-in is used to measure the second-harmonic signal via multiplication of the detector signal by a sinusoidal reference signal at frequency 2ω. It is convenient to first express the resulting signal in component form, i.e. an X component (detector signal $\times\cos\left(2\omega t\right)$) and a Y component (detector signal $\times\sin\left(2\omega t\right)$):

$$X_{2f} = \frac{G\overline{I_0}}{2}\left[H_2 + \frac{i_0}{2}\left(H_1 + H_3\right)\cos\psi_1 + i_2\left(H_0 + \frac{H_4}{2}\right)\cos\psi_2\right], \tag{4.7}$$

$$Y_{2f} = -\frac{G\overline{I_0}}{2}\left[\frac{i_0}{2}\left(H_1 - H_3\right)\sin\psi_1 + i_2\left(H_0 - \frac{H_4}{2}\right)\sin\psi_2\right], \tag{4.8}$$

where G is the optical-electrical gain of the detection system. The absolute magnitude of the $2f$ signal is then given by

$$R_{2f} = \sqrt{X_{2f}^2 + Y_{2f}^2}. \tag{4.9}$$

Note that the $2f$ signal also depends on H_0 and H_4 terms due to the nonlinear intensity modulation. In this derivation we have assumed there is no phase shift between the detector signal and the reference signal, as the $2f$ magnitude of interest is independent of this detection phase shift. To our knowledge, most WMS applications utilize the X

component of the 2*f* signal after adjusting the detection phase shift to zero [Cassidy and Reid 1982; Bomse *et al.* 1992; Wang *et al.* 2000; Liu *et al.* 2004a]. However, this is cumbersome and not accurate for large-modulation-depth WMS used for high-pressure applications, since the 2*f* signal becomes a combination of five Fourier components (H_0 through H_4) with phase shifts (ψ_1 and ψ_2). Instead, we use a lock-in to measure the 2*f* magnitude to simplify the implementation and remove the issue of detection phase. If the intensity modulation is linear, $i_2 = 0$, and Eq. (4.9) is reduced to the model of Philippe and Hanson [1993], which includes the FM/IM phase shift only.

When there is no absorption, H_0=1, H_k=0, Eqs. (4.7)-(4.9) become

$$X_{2f}^0 = \frac{G\overline{I_0}}{2} i_2 \cos\psi_2, \tag{4.10}$$

$$Y_{2f}^0 = -\frac{G\overline{I_0}}{2} i_2 \sin\psi_2, \tag{4.11}$$

$$R_{2f}^0 = \frac{1}{2} G\overline{I_0} i_2. \tag{4.12}$$

This is the background 2*f* signal, which is often referred to as the residual amplitude modulation (RAM) [Kluczynski and Axner 1999; Liu *et al.* 2004a, 2004b]. Note that RAM is a result of the nonlinear behavior of laser intensity modulation. This term becomes more pronounced for large-modulation-depth WMS with 2*f* detection (see section 4.3.2).

In large-modulation-depth WMS measurements, the background 2*f* signal (X_{2f}^0, Y_{2f}^0) needs to be measured and vector subtracted from the 2*f* signal (as shown in Eq.(4.13)) to yield the absorption-based 2*f* signal. The magnitude of the absorption-based 2*f* signal, S_{2f}, is also independent of the detection phase, and given by

$$S_{2f} = \left[\left(X_{2f} - X_{2f}^0 \right)^2 + \left(Y_{2f} - Y_{2f}^0 \right)^2 \right]^{1/2}$$

$$= \frac{G\overline{I_0}}{2} \left\{ \left[H_2 + \frac{i_0}{2} \left(H_1 + H_3 \right) \cos\psi_1 + i_2 \left(H_0 - 1 + \frac{H_4}{2} \right) \cos\psi_2 \right]^2 \right. \tag{4.13}$$

$$\left. + \left[\frac{i_0}{2} \left(H_1 - H_3 \right) \sin\psi_1 + i_2 \left(H_0 - 1 - \frac{H_4}{2} \right) \sin\psi_2 \right]^2 \right\}^{1/2} .$$

If the intensity modulation is assumed to be linear ($i_2 = 0$), Eq. (4.13) is reduced to

$$S_{2f} = \frac{G\overline{I_0}}{2} \left\{ \left[H_2 + \frac{i_0}{2} \left(H_1 + H_3 \right) \cos\psi_1 \right]^2 + \left[\frac{i_0}{2} \left(H_1 - H_3 \right) \sin\psi_1 \right]^2 \right\}^{1/2} . \tag{4.14}$$

If the FM/IM phase shift is further assumed to be π, Eq. (4.14) becomes

$$S_{2f} = \frac{G\overline{I_0}}{2} \left| H_2 - \frac{i_0}{2} \left(H_1 + H_3 \right) \right| . \tag{4.15}$$

This is the 2*f* signal magnitude which is given by the simple model commonly used in atmospheric pressure gas sensing [Philippe and Hanson 1993; Liu *et al.* 2004a].

Using the same procedure as Eqs. (4.7)-(4.9), the magnitude of 1*f* signal can be calculated as

$$R_{1f} = \frac{G\overline{I_0}}{2} \left\{ \left[H_1 + i_0 \left(H_0 + \frac{H_2}{2} \right) \cos\psi_1 + \frac{i_2}{2} \left(H_1 + H_3 \right) \cos\psi_2 \right]^2 \right. \tag{4.16}$$

$$\left. + \left[i_0 \left(H_0 - \frac{H_2}{2} \right) \sin\psi_1 + \frac{i_2}{2} \left(H_1 - H_3 \right) \sin\psi_2 \right]^2 \right\}^{1/2} .$$

For optically thin samples ($\alpha(v) < 0.1$), $1 \approx H_0 \gg H_1, H_2, H_3$, and the 1*f* signal simplifies to

$$R_{1f} = \frac{G\overline{I_0}}{2} \left| H_1 - i_0 \left(H_0 + \frac{H_2}{2} \right) \right| \approx \frac{G\overline{I_0}}{2} i_0 \left[1 - P\chi_i Lf(T,P) \right] . \tag{4.17}$$

The major contribution to the 1*f* signal is generated by the inherent linear intensity modulation (1*f* term in Eq. (4.2)) when modulating the injection current. If contributions from absorption to the 1*f* signal can be neglected, the magnitude of 1*f* signal can be approximated by the 1*f* signal with no absorption:

$$R_{1f}^0 = \frac{1}{2}G\overline{I_0}i_0 . \tag{4.18}$$

For optically thin samples, the transmission coefficient can also be approximated as

$$\tau(v) = \exp\left[-\alpha(v)\right] \approx 1 - \alpha(v) = 1 - P\chi_i L\sum_j S_j \varphi_j , \tag{4.19}$$

and the functions $H_k(\overline{v},a)$ are given by

$$H_0(\overline{v},a) = -\frac{P\chi_i L}{2\pi}\int_{-\pi}^{\pi}\sum_j S_j \varphi_j(\overline{v} + a\cos\theta)d\theta , \tag{4.20}$$

$$H_k(\overline{v},a) = -\frac{P\chi_i L}{\pi}\int_{-\pi}^{\pi}\sum_j S_j \varphi_j(\overline{v} + a\cos\theta)\cos k\theta d\theta . \tag{4.21}$$

H_k is proportional to the product of species concentration χ_i and path length L when the lineshape functions do not vary for the range of gas composition found in the applications.

4.3 Characterization of real diode lasers

To exploit the WMS theory developed in the last section, a diode laser must be characterized to determine the parameters in Eq. (4.2) (i_0, i_2, ψ_1, and ψ_2) for specific modulation frequency and modulation depth. To illustrate these characterization measurements, we examine a telecommunication grade fiber-coupled DFB diode laser (NEL), which is temperature tuned to lase near 1388 nm with a constant bias injection current (~100 mA) using a commercial laser mount (ILX Lightwave, LDM-4980) and current and temperature controller (ILX Lightwave, LDC-3900). The dc injection current is summed with a sinusoidal modulation at 50 kHz and the amplitude of the modulation adjusted to produce the desired modulation depth (see below). To measure the laser characteristics, the laser output is divided by a fiber splitter: the first arm goes to a detector and the other goes through a fiber ring etalon with a free spectral range of 0.0277 cm^{-1} onto a second detector (Thorlabs PDA 400, 10MHz, InGaAs); the detector signals are simultaneously sampled at 100 MHz (GageScope). Figure 4.2 illustrates the experimental setup.
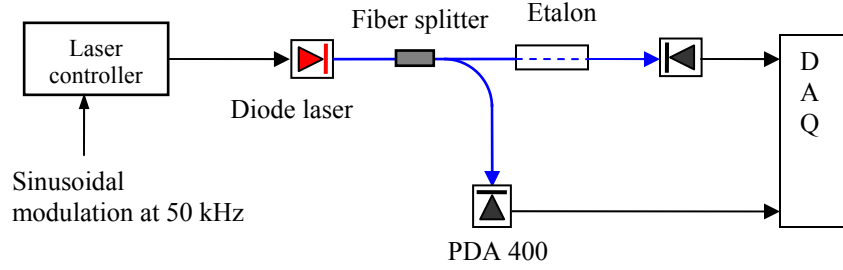
Figure 4.2 Experimental setup for diode laser characterization.

4.3.1 Determination of FM/IM phase shift

The FM/IM phase shift is extracted as shown in Fig. 4.3 from the measured modulation of intensity and frequency; when the laser injection current is sinusoidally modulated, the light intensity is nearly simultaneously modulated, but some delay is observed in frequency modulation [Schilt and Thevenaz 2004]. With the 0.0277 cm^{-1} FSR ring etalon, we find that the laser frequency is well described by a sinusoidal modulation when the diode laser is driven with a pure sine wave injection current. As laser frequency decreases the intensity increases, and most published WMS assumes this FM/IM phase shift is exactly π [Philippe and Hanson 1993; Wang *et al.* 2000; Liu *et al.* 2004]. However, as illustrated in Fig. 4.3, this FM/IM phase shift can be significantly different from π; at a modulation frequency $f = 50$ kHz and modulation depth $a = 0.65$ cm^{-1}, the measured value for this laser is $\psi_1 = 1.21\,\pi$. For the same laser, no variations in FM/IM phase shift are observed with the variations of the diode laser temperature or bias current used in the measurements. However, for a similar laser at a different wavelength (1345 nm), the FM/IM phase shift is measured to be $1.17\,\pi$ at the same modulation frequency and modulation depth. Thus, the value of FM/IM phase shift varies with the specific laser.
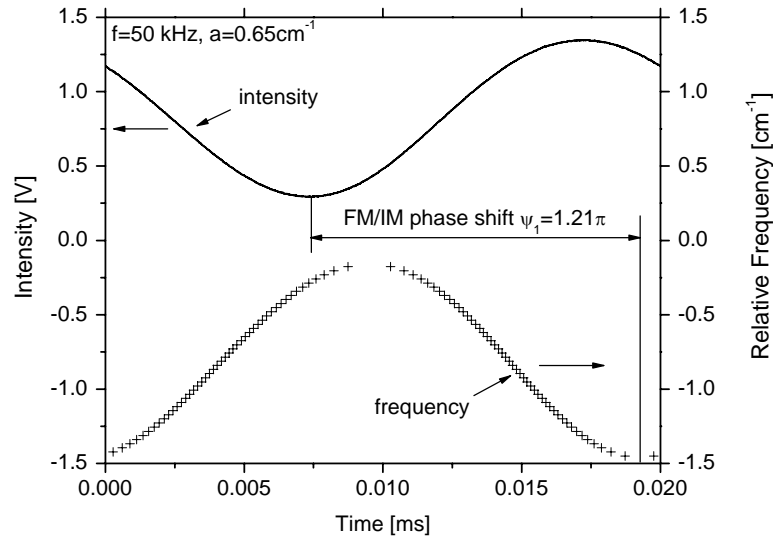
Figure 4.3 Schematic for determining FM/IM phase shift. Solid line: reference laser intensity (without etalon); +: fringe centers determined from the interference signal.

The modulation depth can be adjusted by varying the modulation amplitude of the injection current; note that the modulation depth is defined to be half of the peak-to-peak frequency modulation. Fig. 4.4 shows that the FM/IM phase shift ψ_1 is a weak function of modulation depth a. However, the FM/IM phase shift depends strongly on modulation frequency, as shown in Fig. 4.4b. As modulation frequency decreases, the phase shift decreases, and approaches a value of π at low modulation frequencies.
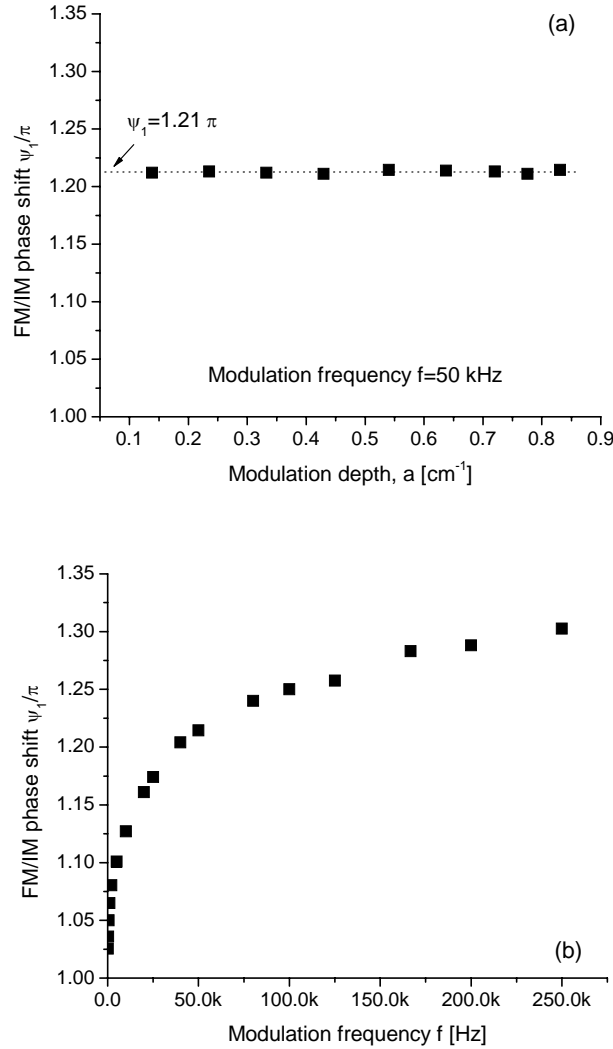
Figure 4.4 Measured FM/IM phase shift ψ_1 of a typical DFB diode laser at: (a) different modulation depths; (b) different modulation frequencies.

4.3.2 Determination of the nonlinear intensity-modulation term

The laser intensity $I_0(t)$ is fit with sinusoidal waveforms to obtain the $1f$ and $2f$ terms. The first panel of Fig. 4.5 shows the best $1f$ fit for the intensity modulation data from Fig. 4.3. The second panel shows the residual of this fit is nearly sinusoidal at twice the modulation frequency. This residual is subsequently fit to obtain the $2f$ nonlinear

Chapter 4

modulation term. It is found that the measured diode laser intensity modulation is well characterized by this combination of 1*f* and 2*f* terms. The nonlinear IM is the source of the background 2*f* signal (RAM). Although the amplitude of the nonlinear IM is small (~2%) compared to linear IM, the induced RAM can be on the same order of the absorption-based 2*f* signals (Section 4.4). This background signal can be suppressed by adding a second-harmonic component to the pure sinusoidal injection current modulation [Liu *et al.* 2004b], or it can be measured and vector-subtracted from the 2*f* signal.
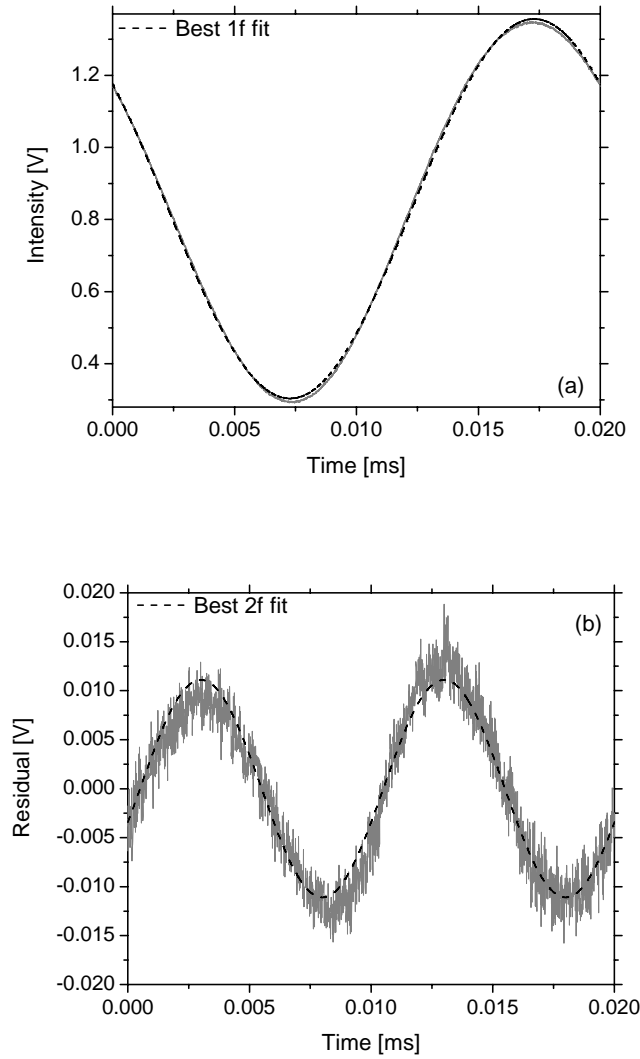
Figure 4.5 (a) Best 1*f* and (b) best 2*f* fit to the laser intensity modulation in Fig. 4.3 (modulation frequency *f* = 50 kHz, modulation depth *a* = 0.65 cm^{-1}).

A plot of the linear intensity modulation amplitude (i_0) versus modulation depth, as shown in Fig. 4.6, indicates that i_0 is proportional to modulation depth. However, the nonlinear IM amplitude, i_2, is a quadratic function of modulation depth, as shown in Fig. 4.7. Thus, as the modulation depth increases, the ratio of i_2/i_0 increases, indicating that the nonlinear effects become more pronounced at large modulation depths. Knowing the FM/IM phase shift ψ_1, the phase shift of the nonlinear IM term ψ_2 can also be determined from the laser intensity fitting. As shown in Fig. 4.8, the nonlinear IM phase decreases gradually with modulation depth at a fixed modulation frequency.
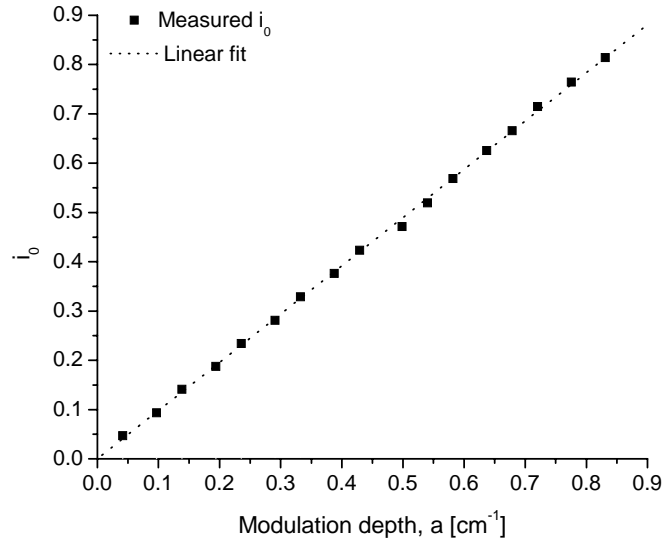
Figure 4.6 Linear laser intensity modulation amplitude versus modulation depth for the laser used in this study. Modulation frequency f = 50 kHz. A best linear fit to the measured data is shown as well.
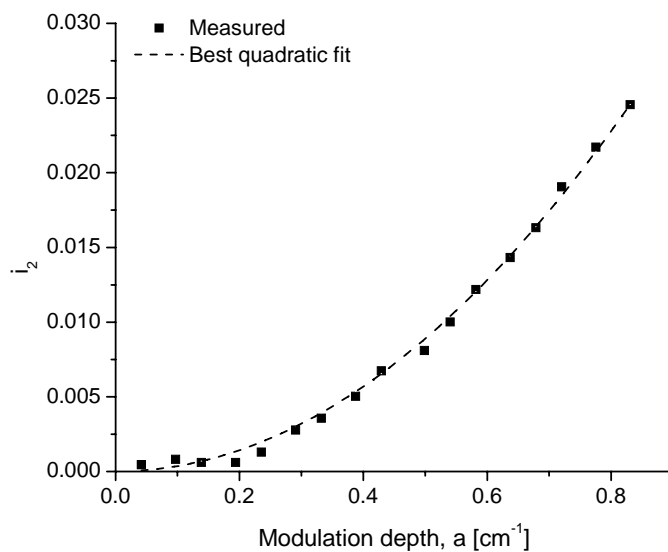
Figure 4.7 Nonlinear intensity modulation amplitude versus modulation depth for the laser used in this study. Modulation frequency f = 50 kHz. A best quadratic fit to the measured data is shown as well.
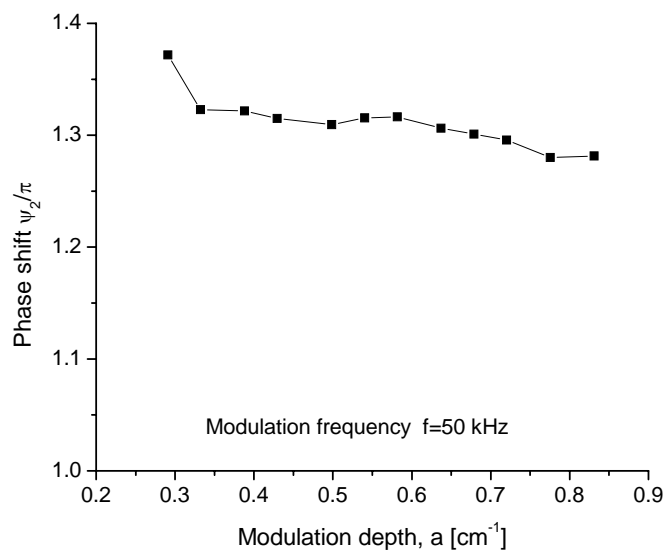
Figure 4.8 Nonlinear term phase shift ψ_2 versus modulation depth for the laser used in this study.

In summary, the normalized laser intensity of the laser used in this study is given for f = 50 kHz and a = 0.65 cm^{-1} as:

$$I_0(t)/\overline{I}_0 = 1 + 0.634\cos(50\text{k} \times 2\pi t + 1.21\pi) + 0.014\cos(100\text{k} \times 2\pi t + 1.31\pi). \qquad (4.22)$$

For the same laser, no variations in these parameters are observed with the variations of diode laser temperature used in this study. After examining four similar lasers at two different nominal wavelengths, we found that these parameters are typical for NIR DFB diode lasers manufactured by NEL and mounted in fiber-coupled butterfly packages. However, these parameters are a strong function of the modulation frequency and specific for individual lasers.

4.4 Validation measurements

4.4.1 Experimental setup

The WMS $2f$ signal model including the diode laser performance parameters (Eq. (4.13)) is tested using the NEL diode laser characterized in Section 4.3 for measurements of the pressure-broadened water vapor features near 1388 nm. Fig. 4.9 illustrates the experimental setup. The light from the diode laser is divided into three paths by fiber splitters: (1) for the first path, light is collimated into free space and the beam passes through a gas cell (with wedged windows) and is focused onto an InGaAs photodetector (PDA 400); for the second path, the light is directed onto a reference detector; and for the third path, the laser wavelength is monitored by a wavemeter (Burleigh WA-1000) when the modulation is removed. A static cell with a 100.5 cm path length is used for room temperature measurements at pressures of 1 atm and 10 atm. Test gas mixtures are prepared by filling a small compressed gas cylinder with pure water vapor and then diluting with compressed dry air to the required pressure. The mixture is mechanically mixed by shaking the gas cylinder in which Teflon beads are placed to aid the stirring process and reduce the mixing time required for a uniform mixture. The free-space optical path external to the gas cell is purged by N_2 to avoid absorption interference from the ambient water vapor.
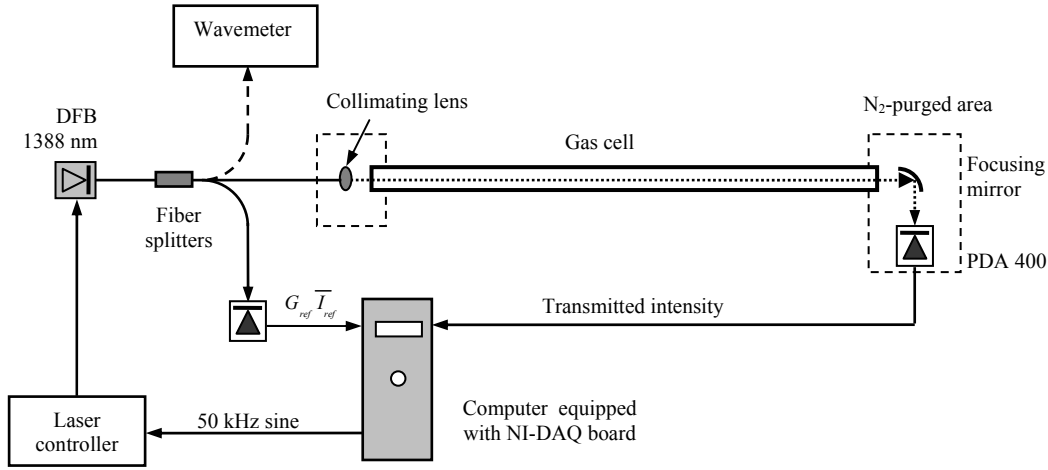
Figure 4.9 Experimental setup for validating the improved 2*f* model.

The detector signals are sampled at 5 MHz, and the *X* and *Y* components of the 2*f* signal are extracted using a digital lock-in program on LabVIEW with an infinite impulse response (IIR) cascade filter. The average laser intensity on the reference detector $G_{ref}\overline{I}_{ref}$ (analogous to $G\overline{I}_0$) is recovered using a low-pass filter with time constant of 1 kHz. For the 2*f* spectrum measurements, the laser center wavelength is set by temperature, and the bias injection current is held constant near 100 mA. For each temperature setting, the laser wavelength (with modulation off) is recorded by using the wavemeter. Without modulation, the diode laser wavelength is repeatable with temperature and bias injection current settings. When the modulation is added, the center laser wavelength is red-shifted due to a laser heating effect from the ac modulation current. The shift is determined by matching measured 2*f* signal with spectral simulations. The cell is initially filled with dry N_2 to the desired pressure to measure the background 2*f* signal (X_{2f}^0, Y_{2f}^0) versus laser center wavelength. Then the cell is filled with test gas mixture to the same pressure to measure the 2*f* signal with absorption. The absorption-based 2*f* magnitude is determined by vector subtracting the background (Eq.

(4.13)). In order to account for the wavelength-dependent average laser intensity $G\overline{I}_0$, the absorption-based 2*f* magnitude is normalized by the measured reference laser intensity $G_{ref}\overline{I}_{ref}$. The reference laser intensity $G_{ref}\overline{I}_{ref}$ is determined to be about twice that of the transmitted laser intensity $G\overline{I}_0$ when there is no absorption. Note this normalization strategy is only employed for the static cell measurements where the goal is limited to WMS model validation. For practical gas sensing applications in harsh environments, laser transmission fluctuations in measurement path must be accounted for, and hence we need a different normalization strategy (see Section 4.5).
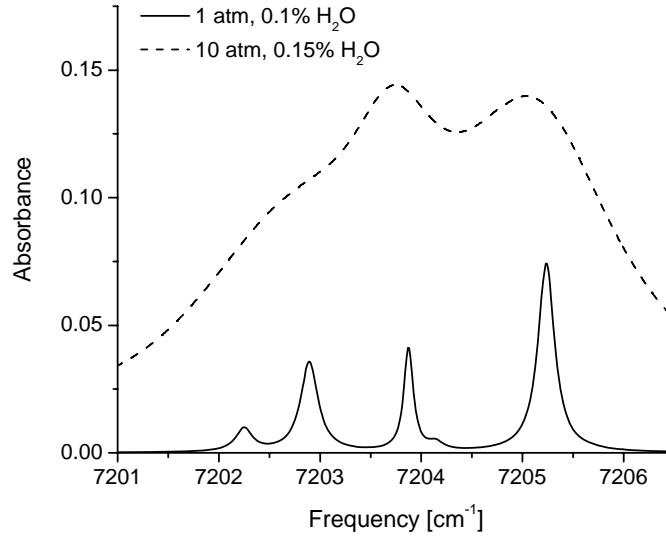
Figure 4.10 Spectral simulation of water vapor in air: T=296 K, L=100.5 cm.

4.4.2 Results

WMS experiments with 2*f* detection are conducted to test the theory developed in Section 4.2 for large-modulation-depth measurements with diode lasers. The 2*f* simulations are based on the HITRAN/HITEMP database [Rothman *et al.* 2003, 2005] updated with precise parameters recently measured [Liu *et al.* 2007b] for the four strong features between 7202 and 7205.5 cm^{-1} (see Fig. 4.10). For the measurements reported here, a

modulation depth of 0.65 cm^{-1} is used for all conditions. Although $a = 0.65$ cm^{-1} over-modulates the laser frequency at a pressure of one atmosphere, we anticipate applications with varying pressure and temperature where an 'optimum' a can not be selected [Zhou *et al.* 2005b]. For such an application, some conditions will be over-modulated while some will be under-modulated, thus requiring an accurate expression to simulate the WMS 2*f* signals.
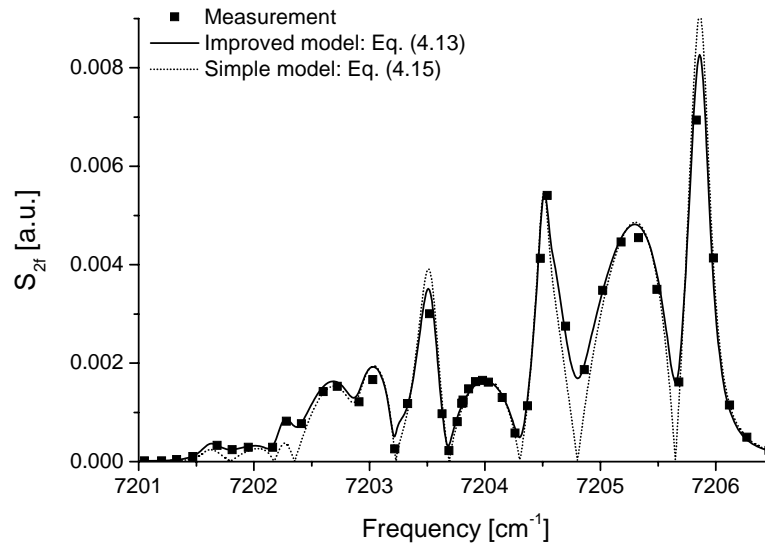
Figure 4.11 Measured and simulated 2*f* spectra at T=296 K, P=1 atm, L=100.5 cm. Test gas: 0.10% H_2O in air.

Simulations including real laser performance (improved model, Eq. (4.13)) provide much better agreement with measurements at one atmosphere pressure, as shown in Fig. 4.11. The water vapor concentration is determined by direct absorption measurements of the strong transition at 7205.3 cm^{-1}. The measured WMS 2*f* signal has been frequency shifted by -0.10 cm^{-1} to match the simulated spectra. Simulations with the improved model and the model with FM/IM phase shift only (assuming linear IM) are virtually identical, indicating that the nonlinear IM is not significant at this condition. In this case, the absorption features are relatively narrow and isolated (Fig. 4.10), thus there is no

significant interference on 2*f* signal from neighboring features. The laser frequency is highly over-modulated at this condition: modulation index $m = a/\Delta\nu \sim 12$ (where $\Delta\nu$ is the half width at half maximum of the absorption line at 7202.9 cm^{-1}). When the laser frequency is modulated at optimum *a* (~0.12 cm^{-1}) for room T and P, the difference in simulated 2*f* spectra between the improved model and the simple model is small enough to be negligible. Thus, the FM/IM phase shift and the nonlinear IM are not significant for small-modulation-depth WMS for isolated transitions at atmospheric pressure with this diode laser.

The measured background 2*f* signal is about 0.0036 when normalized by the measured reference laser intensity $G_{ref}\overline{I}_{ref}$. This is in good agreement with the value predicted by Eq. (4.12), $R_{2f}^0 / G_{ref}\overline{I}_{ref} = 0.0035$. This background value is on the same order of the absorption-based 2*f* signal.

Fig. 4.12 shows the comparison between simulated and measured 2*f* signal magnitudes at 10 atm, where pressure broadening blends the absorption features and the FM/IM phase shift and nonlinear IM effects are both important for quantitative agreement between measurement and model. For this condition, the laser frequency is under-modulated. The influence of the FM/IM phase shift and the nonlinear IM is relatively small at the center of a dominant line, but these effects are large for laser center frequencies off the peak. In addition, the local 2*f* peak position has moved from 7203.51 cm^{-1} to 7203.66 cm^{-1}. Thus, fixed-wavelength WMS schemes for variable pressure applications will be shifted from the low pressure line center by pressure shift effects as well as by blending of neighboring features. The expression for the 2*f* signal must account for the FM/IM phase shift and the nonlinear IM for accurate measurements in the wings of the transitions.
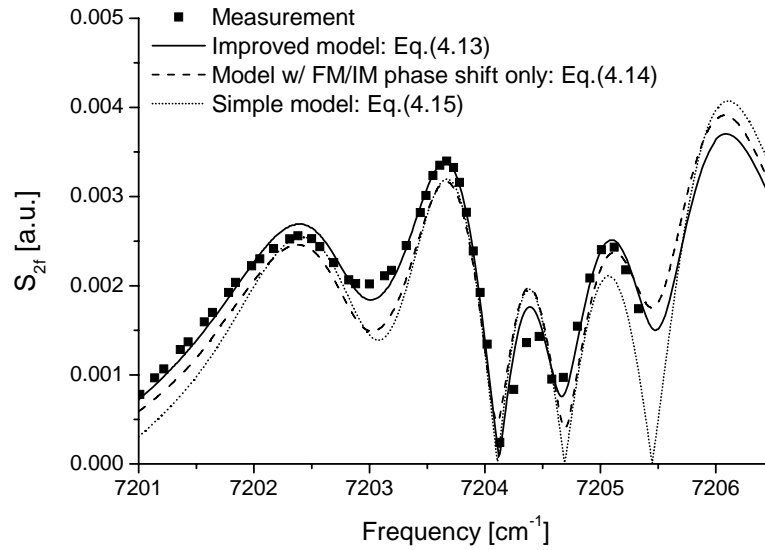
Figure 4.12 Measured and simulated $2f$ spectra: T=296 K, P=10 atm, L=100.5 cm. Test gas: 0.15% H_2O in air.

4.5 WMS with 1f-normailzed 2f detection

There is much discussion in the literature that recognizes the need for transmission corrections for WMS measurements in harsh environments [Cassidy and Reid 1982; Iseki *et al.* 2000; Wannier *et al.* 2002; Fernholz *et al.* 2002; Liu *et al.* 2004a 2004b]. For WMS absorption measurements of optically thin absorption transitions ($\alpha(v) < 0.05$), the change in the 1f signal by absorption may be neglected, and the 1f signal becomes an effective normalization signal accounting for losses from scattering, beam steering, mechanical misalignments, soot, and window fouling. The simulated magnitude of the 1f signal (using Eq. (4.16)) for 1% H_2O in air at 1000 K with 1 cm path length is shown in Fig. 4.13 using the laser parameters characterized in Section 4.3 (Eq. (4.22)). Note that the 1f signal has been normalized by the 1f signal without absorption, R_{1f}^0 (Eq. (4.18)). The maximum deviation of the 1f signal from R_{1f}^0 is approximately the value of the absorbance (Fig. 4.1). Hence if the absorbance is 5%, the error induced by neglecting

contributions from absorption to the $1f$ signal will be less than 5%. For optically thick samples, it is necessary to perform full simulation using Eq. (4.16).
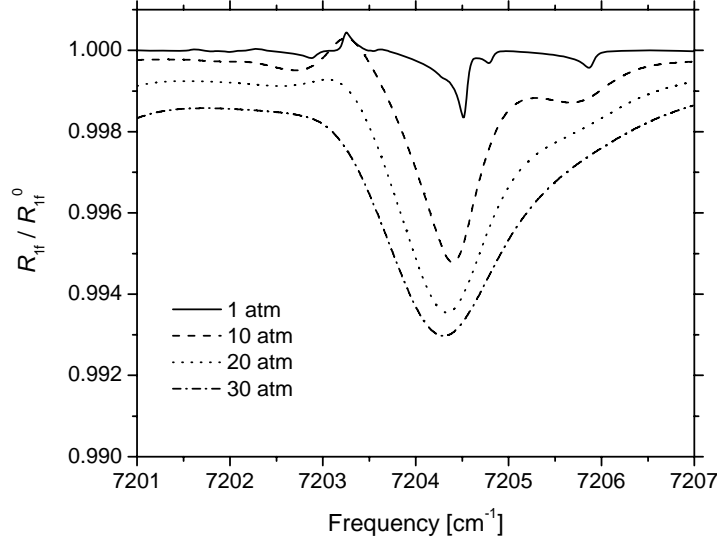
Figure 4.13 Simulated $1f$ spectra (normalized by the $1f$ signal without absorption) of 1% H_2O in air at T=1000 K, 1 cm pathlength (modulation depth $a = 0.65$ cm^{-1}).

From Eqs. (4.13) and (4.18), the $1f$-normalized absorption-based $2f$ magnitude is given by

$$C = \frac{S_{2f}}{R_{1f}}$$

$$\approx \frac{1}{i_0} \left\{ \left[H_2 + \frac{i_0}{2}(H_1 + H_3)\cos\psi_1 + i_2\left(H_0 + \frac{H_4}{2}\right)\cos\psi_2 \right]^2 + \left[\frac{i_0}{2}(H_1 - H_3)\sin\psi_1 + i_2\left(H_0 - \frac{H_4}{2}\right)\sin\psi_2 \right]^2 \right\}^{1/2}.$$

(4.23)

C is proportional to the product of species concentration χ_i and path length L when the lineshape functions (and thus H_k) do not vary for the range of gas composition found in the applications. By normalizing the $2f$ signal magnitude with the $1f$ signal magnitude, common terms such as laser output intensity, optical-electrical gain, and laser transmission variations are eliminated. The $1f$-normalized absorption-based $2f$ magnitude is a function of laser parameters (i_0, i_2, ψ_1, ψ_2, and a via $H_k(\bar{v}, a)$) and gas parameters

(within H_k terms) only. The laser parameters can be characterized for the diode lasers used in measurements (Section 4.3), and if this is done, no calibration is needed to scale the simulations to the measurements. Note these measurements have been appropriately corrected for RAM. For example, if the total pressure P is known from an external pressure transducer reading, the gas temperature can be inferred by comparing the measured ratio of 1f-normalized absorption-based 2f signal magnitudes at two selected wavelengths with simulations. After the temperature is known, the species concentration can be determined from either of the C signals. The theory developed in this thesis accounts for real diode laser performance and enables "calibration free" WMS-2f measurements. This 2f ratio thermometry and species concentration measurement strategy is discussed in detail in Chapter 5 and in Rieker *et al.* [2007a, 2007b].

Chapter 5

RAPID TDL SENSOR FOR TEMPERATURE AND H_2O IN A SHOCK TUBE

In this chapter, a fast-response (100 kHz) TDL absorption sensor is developed for measurements of temperature and H_2O concentration in shock tubes for studies of combustion chemistry. Gas temperature is determined from the ratio of fixed-wavelength laser absorption of two H_2O transitions near 7185.60 cm^{-1} and 7154.35 cm^{-1}, which are selected using design rules for the target temperature range of 1000-2000 K and pressure range of 1-2 atm. WMS is employed with second-harmonic detection (WMS-2f) to improve the sensor sensitivity and accuracy. Normalization of the second-harmonic signal by the first-harmonic signal is used to remove the need for calibration and minimize interference from emission, scattering, beam steering, and window fouling. The laser modulation depth for each H_2O transition is optimized to maximize the WMS-2f signal for the target test conditions. The WMS-2f sensor is first validated in mixtures of H_2O and Ar in a heated cell for the temperature range of 500-1200 K. Shock wave tests with non-reactive H_2O-Ar mixtures are then conducted to demonstrate the sensor accuracy and response time at higher temperatures (1200-1700 K, P=1.3-1.6 atm).

5.1 Introduction

Chemical kinetics studies in the controlled pressure and temperature environment of shock tubes provide important reaction rate parameters as well as validation of complete combustion mechanisms [Bowman and Hanson 1979; Curran *et al.* 1998; Hanson and Davidson 2001]. When the heat release of the post-shock chemistry is small compared to

the heat capacity of the gas mixture, the post-shock temperatures are given precisely by the measured shock velocity and the standard shock wave relations. However, it is desirable to test chemical mechanisms of combustible mixtures that provide significant heat release. For these chemical kinetics shock tube experiments, a temperature sensor with fast time-response providing accurate temperature time-histories would improve the quality of kinetic data. Here we report the development of a TDL sensor for nonintrusive measurements of gas temperature and H_2O concentration behind reflected shock waves, with a 100 kHz bandwidth, thus providing a new diagnostic tool to study the combustion mechanisms of hydrocarbon fuels over a wide range of conditions. In cases where H_2O is not naturally present or is not a reasonable additive, other infrared-active tracers such as CO_2 may be used instead.

The WMS technique is used in the sensor design to improve SNR. In this technique, the laser wavelength is rapidly modulated (typically hundreds of kHz), and the second harmonic of the laser transmission signal (WMS-2*f* signal) is recorded by a lock-in amplifier. Gas temperature can be inferred from the ratio of the WMS-2*f* signals of two transitions. This technique is sensitive to absorption lineshape curvature rather than the absorption magnitude alone, and is insensitive to low-frequency noise. Thus WMS-2*f* offers benefits over direct absorption in terms of noise resistance and sensitivity. For example, in the case of weak absorbance, the baseline fitting which is required in the scanned-wavelength direct absorption measurements is a large source of uncertainty. This problem is eliminated in the WMS measurements. The lock-in amplifier also serves as a band-pass filter and rejects noise outside the lock-in bandwidth. Finally, normalization of the WMS-2*f* signal with the 1*f* signal can remove the need for calibration and account for the laser transmission variations due to beam steering, scattering and window fouling [Li *et al.* 2006; Rieker *et al.* 2007a]. These benefits make WMS with second-harmonic detection an attractive technique for combustion measurements. Scanned-wavelength WMS-2f has been successfully demonstrated in various applications [e.g., Philippe and Hanson 1993; Liu *et al.* 2004a] with typical bandwidth of several kHz; a fixed-wavelength WMS-2*f* technique has been demonstrated in IC engines with a bandwidth of

7.5 kHz [Rieker *et al.* 2007a]. In shock tube studies of combustion mechanisms of hydrocarbon fuels, the typical test time ranges from several tens microseconds to a few milliseconds, and the desired sensor bandwidth is ~100 kHz. Hence fixed-wavelength WMS-2*f* is used in the TDL sensor design to achieve the needed high bandwidth. To our knowledge, this is the first realization of a temperature sensor with a 100 kHz bandwidth using a WMS-2*f* technique.

Water vapor is a major combustion product of hydrocarbon fuels and has a strong and broad absorption spectrum. Furthermore, the rovibrational spectrum of water vapor in the NIR overlaps with well-developed telecommunication laser technology. Therefore, H_2O has been chosen as the target absorbing species to be probed in the shock tube. In subsequent applications, the gas temperature inferred from the absorption ratio of two H_2O transitions can provide useful information of heat release, while the H_2O concentration will serve to indicate the completeness of combustion.

5.2 Fixed-wavelength WMS-2*f* thermometry

The theory of WMS including real diode laser performance has been described in detail in Chapter 4. In fixed-wavelength WMS measurements, the background 2*f* signal needs to be measured in the absence of absorption and vector-subtracted from the 2*f* signal (as shown in Eq. (4.13)). For the small modulation depths (a~0.06 cm^{-1}, $i_2 \sim 0.002, i_0 \sim 0.26$) used in this chapter, the contribution of nonlinear laser IM to the absorption-based WMS-2*f* signal near the line center of discrete spectra can been neglected, and the FM/IM phase shift ψ_1 can be assumed to be π [Li *et al.* 2006]. However, the background 2*f* signal introduced by the nonlinear laser IM is about several percent of the measured 2*f* signal, and thus needs to be subtracted to infer the absorption-based 2*f* signal. The commonly used simple model can be used for the absorption-based WMS-2*f* and the WMS-1*f* signal:

$$S_{2f}(\overline{v}) = \frac{G\overline{I}_0}{2}\left|H_2 - \frac{i_0}{2}(H_1 + H_3)\right|. \tag{5.1}$$

$$R_{1f}(\overline{v}) = \frac{G\overline{I}_0}{2}\left|H_1 - i_0\left(H_0 + \frac{H_2}{2}\right)\right|. \tag{5.2}$$
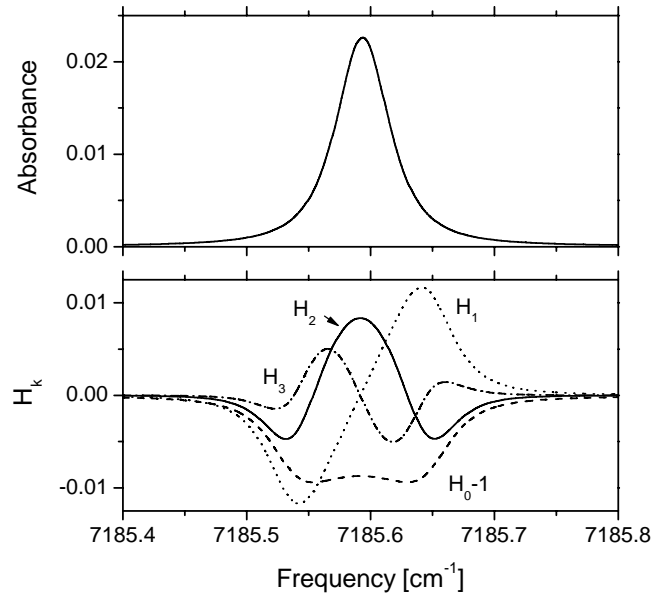
Figure 5.1 Simulated absorption lineshape for the H$_2$O line near 7185.60 cm^{-1} and the corresponding coefficients H_k in the Fourier cosine series for P=1.5 atm, 0.5% H$_2$O in Ar, L=15 cm, and a=0.058 cm^{-1}. Neighboring features have been neglected.

The hardware-related parameters and transmission losses can thus be accounted for by normalizing the absorption-based WMS-2f signal with the WMS-1f signal:

$$C = \frac{S_{2f}}{R_{1f}} = \frac{\left| H_2 - i_0 \left(H_1 + H_3 \right)/2 \right|}{\left| H_1 - i_0 \left(H_0 + H_2/2 \right) \right|}. \tag{5.3}$$

Gas temperature can be obtained from the ratio of the 1f-normalized WMS-2f signals near the line center of two transitions

$$R = \frac{C_2}{C_1} = \frac{\left(S_{2f}/R_{1f} \right)_{\bar{\nu}_2}}{\left(S_{2f}/R_{1f} \right)_{\bar{\nu}_1}}, \tag{5.4}$$

which is closely related to the ratio of absorption line strengths.

Figure 5.1 illustrates the first four Fourier components obtained for the H$_2$O line near 7185.60 cm^{-1} for P=1.5 atm, 0.5% H$_2$O in Ar, and L=15 cm. It can be seen that H_1 and H_3 are zero-valued and H_2 is maximized at line center in the case of an isolated absorption

feature. Thus, the second Fourier component, H_2, is the dominant term for the WMS-2f signal near line center. In addition, H_0 is close to unity, and is the dominant term for the WMS-1f signal near line center (close to $G\bar{I}_0 i_0 / 2$). Therefore, the laser wavelengths of the TDL sensor will be fixed near the line center of selected H_2O transitions.

5.3 WMS-2f sensor design

5.3.1 Selection of spectral lines

Selection of optimum absorption transitions is the first important step in the development of two-line thermometry based on WMS-2f detection. Systematic line-selection criteria for absorption-based thermometry have been developed in the literature [Zhou *et al.* 2003; Zhou *et al.* 2005b; Liu *et al.* 2006]. Here, we briefly discuss the design rules to evaluate the choices and choose the optimum H_2O lines for combustion temperature measurements in near-atmospheric-pressure shock tube experiments. This procedure is similar to that used in [Liu *et al.* 2006] and can be extended to high-pressure applications [Zhou *et al.* 2005b].

The first criterion is to limit the wavelength range to the spectral region of 1.3-1.5 μm, where the $2\nu_1$, $2\nu_3$ and $\nu_1+\nu_3$ bands of H_2O absorption spectrum overlap with the telecommunication band. In this region, robust fiber-coupled single-mode diode lasers and fiber optics are readily available. There are 6435 H_2O lines listed in the HITRAN 2004 database [Rothman *et al.* 2005] within this region.

The second criterion is to ensure sufficient absorption for high SNR measurements over the expected conditions in the shock tube: T=1000-2000 K, P=1-2 atm, χ_{H2O}=0.001-0.02, and L=15 cm. Here we assume a minimum detectable absorbance of 0.0002 (which is estimated from the actual WMS-2f experiments) and a desired SNR ≥10. Thus, the peak absorbance is required to be larger than 0.002. The line center absorption for each H_2O transition in the 1.3-1.5 μm region is calculated with the spectroscopic parameters provided by HITRAN 2004, and is found to be less than 0.12 for the expected conditions.

Thus, no upper limit for the peak absorption is necessary for our sensor design. This criterion reduces the possible lines from 6435 to 139 potential candidates.

The third criterion is to minimize the absorption interference from ambient water vapor. For a H_2O transition with strong absorption at room temperature (i.e., with a small value of lower-state energy E''), great care must be taken in purging the region outside the target measurement path length with nitrogen or dry air [Zhou *et al.* 2003]. This difficulty can be mitigated by using H_2O transitions with $E''>1000$ cm^{-1}. This criterion reduces the number of candidate lines to 90.

The fourth criterion is freedom of significant interference from nearby transitions to minimize the uncertainty in the analysis of WMS-2*f* measurements over the expected conditions in the shock tube. The absorption spectra for the remaining 90 candidates are simulated at T=1000 K and 2000 K, P=1.5 atm, with the parameters from HITRAN 2004 to investigate the potential interference from neighboring transitions. Only features free from strong interferences within ± 0.3 cm^{-1} of their line center frequencies are retained. This criterion reduces the number of candidate transitions to 17.

For WMS-2*f* measurements, accurate information of the spectral lineshapes and their temperature dependences are needed. The HITRAN 2004 database provides a good reference for sensor design. However, the spectroscopic parameters of the selected transitions must be validated before use in a combustion sensor. In addition, some spectral parameters needed here are not listed in the HITRAN database: temperature exponents for self-broadening and shift parameters, and Ar-broadening and -narrowing parameters [Li *et al.* 2007c]. Experiments in a well-controlled environment (e.g., a heated static cell with temperature up to 1200 K) are usually conducted to determine these important spectroscopic parameters [Zhou *et al.* 2003; Liu *et al.* 2006]. Thus, the fifth criterion, to be free of significant interference from nearby transitions for the temperature range of 500-1200 K, minimizes the uncertainty in the measurements of spectroscopic parameters in the heated static cell. This criterion further reduces the number of candidate transitions to five as listed in Table 5.1.

Table 5.1 Candidate H$_2$O lines for NIR TDL sensor for shock tube. Line selection based on the HITRAN2004 database

Line	Wavelength [nm]	Frequency [cm^{-1}]	S(296K) [cm^{-2}/atm]	E" [cm^{-1}]
A	1397.75	7154.35	3.85E-4	1789.04
B	1391.67	7185.60	1.97E-2	1045.06
C	1342.11	7450.93	5.38E-4	1690.66
D	1341.48	7454.44	1.83E-4	1962.51
E	1339.08	7467.77	1.27E-5	2551.48
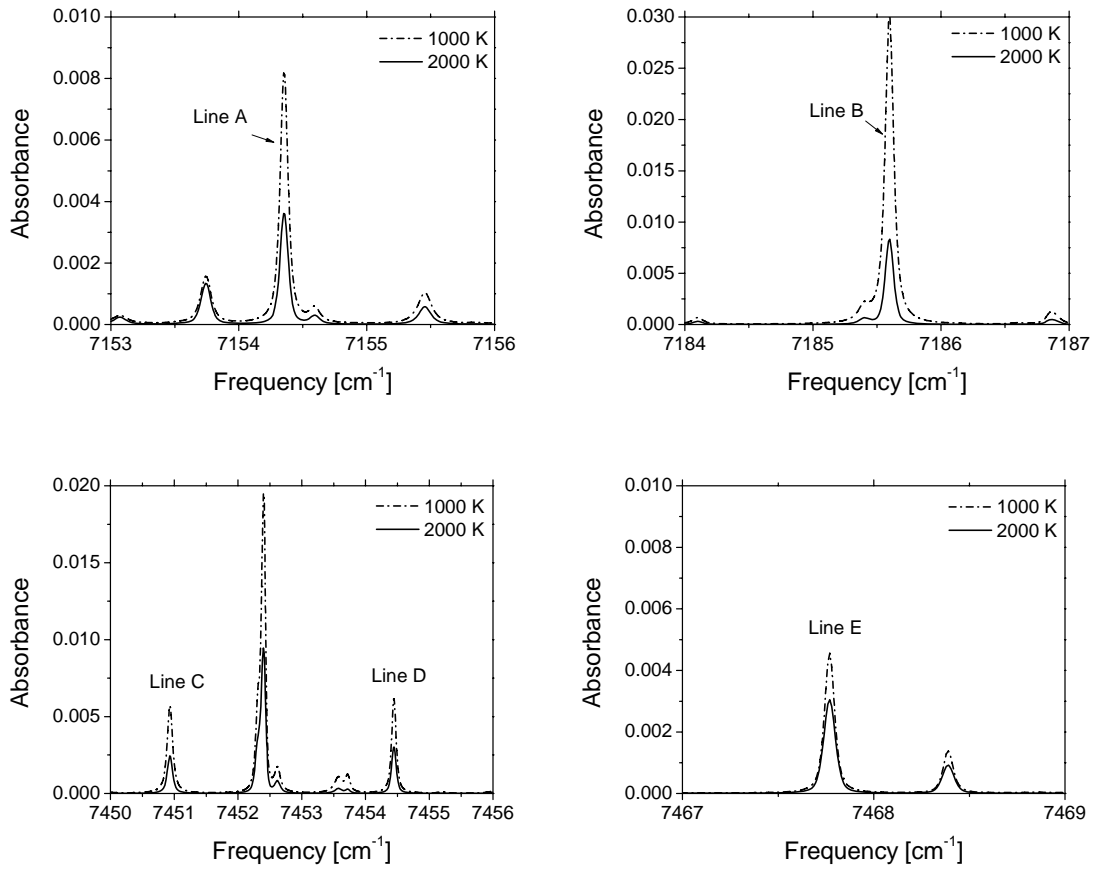
Figure 5.2 Simulated absorption spectra for the five selected H$_2$O lines in the 1.4 μm region using the HITRAN2004 database for *P*=1.5 atm, 0.5% H$_2$O in air, *L*=15 cm

The sixth criterion is that the two H_2O lines should have sufficiently different lower state energy E" to yield a good temperature sensitivity. As shown by Eq. (2.19), the larger the difference of the lower state energy, the better the temperature sensitivity. A constraint on minimum lower state energy difference of 700 cm^{-1} is used in the line selection [Zhou 2005c]. There are 5 possible line pairs satisfying this criterion: AB, AE, BD, BE, and CE.

Figure 5.2 shows the simulated H_2O (0.5%) absorption spectra for the five selected lines based on HITRAN 2004 parameters. It can be seen from Fig. 5.2 that lines C, D and E are weaker than lines A and B for the target temperature range of 1000-2000 K. Therefore, the two H_2O transitions near 7154.35 cm^{-1} (line A) and 7185.60 cm^{-1} (line B) are selected for the WMS-2*f* temperature sensor to optimize the SNR in shock tube measurements. If the absorbance is larger (i.e., in applications with higher water concentration or longer path length), the line pair BE could be employed to improve the temperature sensitivity for high temperature measurements (*T*~ 2000 K).
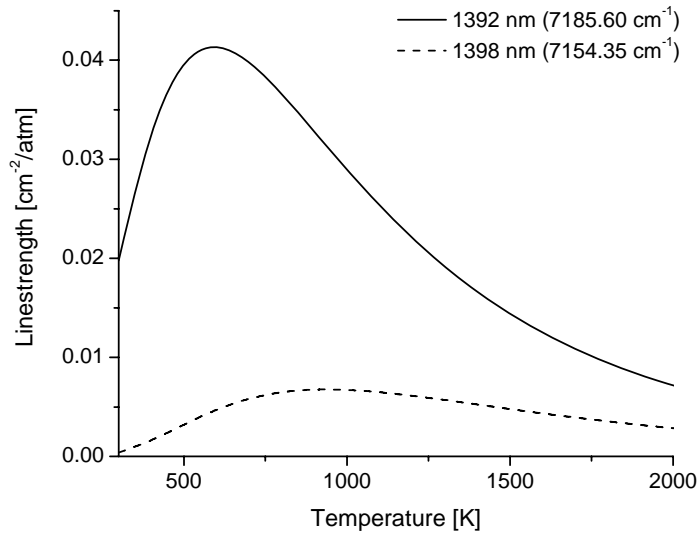
Figure 5.3 Line strength as a function of temperature for H_2O lines at 1392 nm and 1398 nm, using validated parameters (Table 3.1 and 3.3).

The spectroscopic parameters for the two selected H_2O transitions were systematically measured in a heated static cell and are summarized in Table 3.1 and 3.3. The measured high-resolution, Ar-broadened, H_2O absorption lineshapes deviated significantly form the commonly used Voigt profile because of collisional narrowing [Dicke 1953]. Therefore, the Galatry lineshape function [Galatry 1961] was utilized to include the collisional-narrowing effects induced by Ar-H_2O collisions. Note that the Galatry profile is computationally more expensive than the relatively simple Voigt profile [Varghese and Hanson 1984]. Detailed discussion can be found in section 3.5. Figure 5.3 plots the measured line strength versus temperature for these two H_2O transitions.

5.3.2 Optimization of modulation depth

As can be seen from Eq. (4.21), the WMS-2*f* peak height is dependent on the lineshape function, which can potentially cause difficulties in the temperature measurements using WMS-2*f* spectroscopy. Fortunately, this effect can be mitigated by choosing an optimum modulation depth, as discussed by Liu *et al.* [2004a].
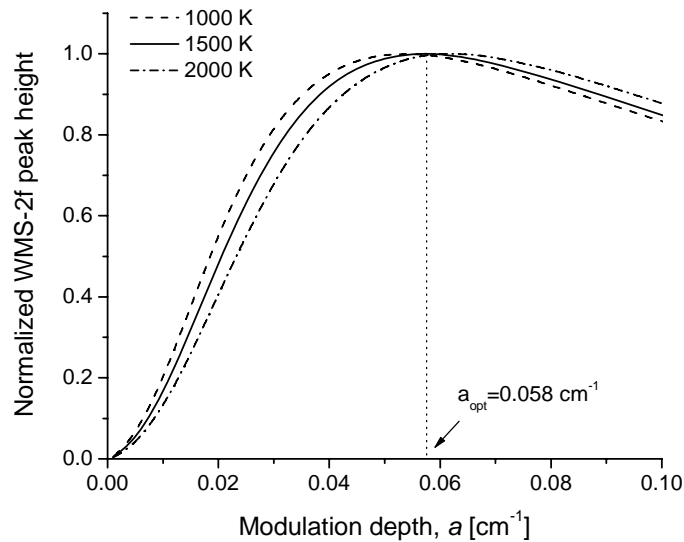
Figure 5.4 Simulated WMS-2*f* peak height for the H_2O transition near 7189.60 cm^{-1} versus modulation depth *a*; *P*= 1.5 atm, 1% H_2O in Ar, and *L*=15 cm.

Figure 5.4 plots the simulated WMS-2f peak height (which is essentially the normalized value of $\int_{-\pi}^{\pi} \varphi(\bar{v} + a\cos\theta)\cos 2\theta d\theta$) of the H_2O transition near 7185.60 cm^{-1} versus modulation depth at three temperatures (T=1000, 1500, and 2000 K; P= 1.5 atm, 1% H_2O in Ar, and L=15 cm). The Galatry lineshape function with the spectroscopic parameters listed in Table 3.1 and 3.3 is used in the numerical simulation. For these conditions, the FWHM of the absorption lineshape is ~0.052cm^{-1}. The maximum values of WMS-2f peak signal occur at modulation index m~2.2 for all three temperatures, which is consistent with previous work using Gaussian, Lorentzian and Voigt lineshapes [Arndt 1965; Reid and Labrie 1981; Liu *et al.* 2004a]. Furthermore, the WMS-2f peak height varies very slowly for modulation depths with m near 2.2. By choosing the optimum modulation depth a_{opt}=0.058 cm^{-1} with m=2.2 at T=1500 K and P=1.5 atm, the integral remains relatively constant for the target temperature range of 1000-2000 K. Thus, the ratio of two WMS-2f peak heights is mainly a function of the well-known line strengths of the selected absorption features. Similarly, the optimum modulation depth for the H_2O transition near 7154.35 cm^{-1} is determined to be 0.055 cm^{-1} for the range of expected test conditions in the shock tube. These selected modulation depths are suitable for WMS measurements with the pressure range of 1.2-1.8 atm and temperature range of 1000-2000 K. For significantly different pressures and temperatures, different modulation depths can be determined using the same procedure.

For the fixed-wavelength WMS-2f sensor, the laser wavelengths are chosen near the line center of the two H_2O transitions, and gas temperature is determined by comparison of the measured 1f-normalized WMS-2f signal ratio with simulations at the measured pressure by a pressure transducer. Figure 5.5 illustrates the simulated WMS-2f signal ratio for 7154.35 cm^{-1}/7185.60 cm^{-1} line pair as a function of temperature for various pressures with optimum modulation depths for the two H_2O transitions (1% H_2O in Ar). The WMS-2f signal ratio is closely related to the ratio of absorption line strengths, and is only a weak function of pressure. For example, at T=1300 K, a 12.5% change in total gas pressure induces only a small change (1.3%) in the inferred gas temperature. Thus, the changes in the measured WMS-2f ratio primarily reflect the changes of gas temperature.
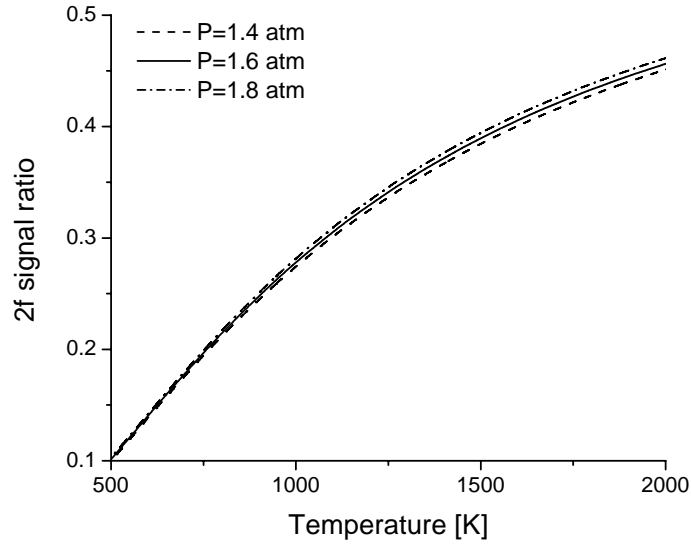
Figure 5.5 Simulated WMS-2*f* signal ratio for 7154.35 cm^{-1}/7185.60 cm^{-1} line pair as a function of temperature for various pressures; 1% H_2O in Ar, modulation depth *a*=0.055 cm^{-1} and 0.058 cm^{-1} for line 7154.35 cm^{-1} and 7185.60 cm^{-1}, respectively.

5.4 Sensor validation in heated cell

5.4.1 Experimental setup

The TDL sensor is first validated in a 3-section heated static cell, before being used in shock-heated gases. Figure 5.6 illustrates the experimental setup, which has also been used for the spectroscopy measurements of the two H_2O transitions used in the TDL sensor (Chapter 3). The center section of the cell is filled with H_2O-Ar test mixture, while the outer sections are in vacuum to avoid interference from ambient water vapor. The gas pressures are measured by a 1000 Torr MKS Baratron pressure transducer with an accuracy of ±0.12% of reading.
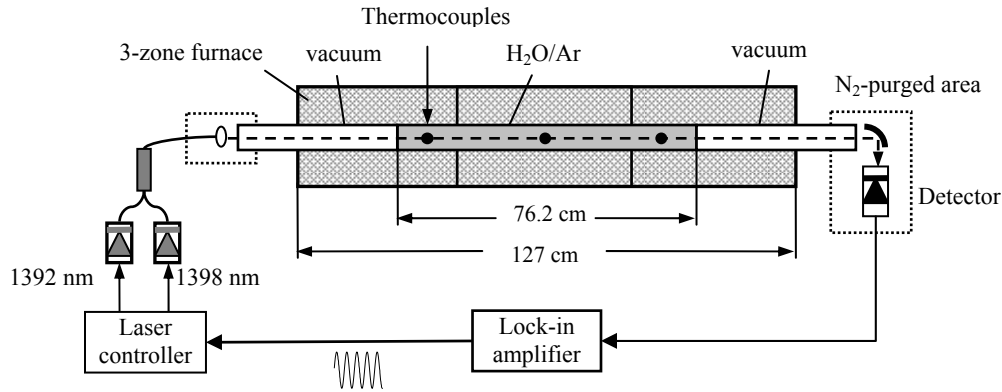
Figure 5.6 Schematic of the experimental setup used for WMS-2f sensor validation.

Two fiber-coupled distributed-feedback (DFB) diode lasers (NEL NLK1E5E1AA, 10 mW) operating near 1392 nm and 1398 nm are multiplexed into a single-mode fiber. The laser center wavelengths are tuned to 1391.673 nm (7185.596 cm^{-1}) and 1397.751 nm (7154.350 cm^{-1}), respectively, using a Burleigh WA-100 wavemeter. These two wavelengths are near the line center of the two H_2O transitions for the test conditions. Each laser wavelength is modulated by a sinusoidal current modulation: f=200 kHz and a=0.062 cm^{-1} for laser 1392 nm, f=550 kHz and a=0.057 cm^{-1} for laser 1398 nm. The laser modulation depths are inferred by sinusoidally fitting the fringe centers in the interference pattern produced by a fiber-ring etalon with a free spectral range of 0.0277 cm^{-1}. These modulation depths are adjusted to the optimal values for cell conditions. The amplitude of laser IM (i_0) is determined by fitting the laser intensity signal without absorption. The laser beam is collimated by a lens, directed across the cell, and focused by a spherical mirror onto an InGaAs detector (PDA 400, 10 MHz). The optics and detector are enclosed by plastic bags purged by dry N_2 to avoid absorption interference from ambient water vapor. The detector signal is demodulated by a Perkin-Elmer lock-in amplifier (model 7280) to recover the 1f and 2f signals with a time constant of 10 µs.

In the validation tests, the diode lasers are turned on one at a time to probe the two H_2O transitions. The heated static cell is first evacuated and the background 1f signal (magnitude S_{1f}^0) and 2f signal (X and Y components for vector-subtraction, see Eq.(4.13))

are taken for each laser. The cell is then filled with H_2O-Ar mixture to *P*= 1 atm, and the 1*f* and 2*f* signals with absorption are recorded for each laser. The background-subtracted 1*f*-normalized WMS-2*f* signal is compared with simulations (Fig. 5.5) to infer gas temperature and H_2O concentration in the cell. For the test conditions (1% H_2O in Ar, P=1 atm, T=500-1200 K) in the cell, the background 2*f* signal is less than 1.5% and 8% of the absorption-based 2*f* signal for laser 1392 and 1398 nm, respectively. The 1392 nm laser is injection current tuned with a 100 Hz linear ramp (with sinusoidal modulation off) across the absorption feature near 7185.60 cm^{-1} to determine the actual H_2O concentration in the test mixture for comparison.

5.4.2 Results

Figure 5.7 shows the measured H_2O absorption spectrum in the H_2O-Ar mixture at the experimental conditions of *T*=1047 K, *P*=1 atm. The experimental profiles are best-fit using a Galatry profile, and the residual (difference between data and fit normalized by peak absorbance) is shown in the upper panel. The H_2O mole fraction in this test mixture is inferred to be 0.0105 using the integrated absorbance area for the H_2O transition near 7185.60 cm^{-1} with the line strength data listed in Table 3.1. The H_2O concentration varies (by up to ±5%) from one fill to another due to adsorption in the mixing tank and the gas handling system [Rieker *et al.* 2007c].

The left panel of Fig. 5.8 compares the thermocouple measurements with the temperatures from the WMS-2*f* sensor measurements (sensor bandwidth 100 kHz, no averaging). The temperatures determined from the WMS-2*f* sensor are in good agreement with the thermocouple readings (standard deviation=1.9%) over the entire temperature range of 500-1200 K. The right panel of Fig. 5.8 shows the ratio of the H_2O mole fraction measured by the WMS-2*f* sensor using the high *E″* line at 7154.350 cm^{-1} ($\chi_{Measured}$) and the mole fraction measured by direct absorption with the transition near 7185.60 cm^{-1} (χ_{Actual}). The standard deviation between the measured and actual H_2O mole fraction is 1.4% over the tested temperature range. The excellent agreement between measured and actual values confirms the accuracy of the WMS-2*f* sensor for both temperature and H_2O concentration measurements. The errors in Fig. 5.8 primarily come from the uncertainties

in the measured spectroscopic data (3%), temperature measurements by thermocouple (0.75%), and errors in the baseline and profile fits (0.5%) in the direct absorption measurements.
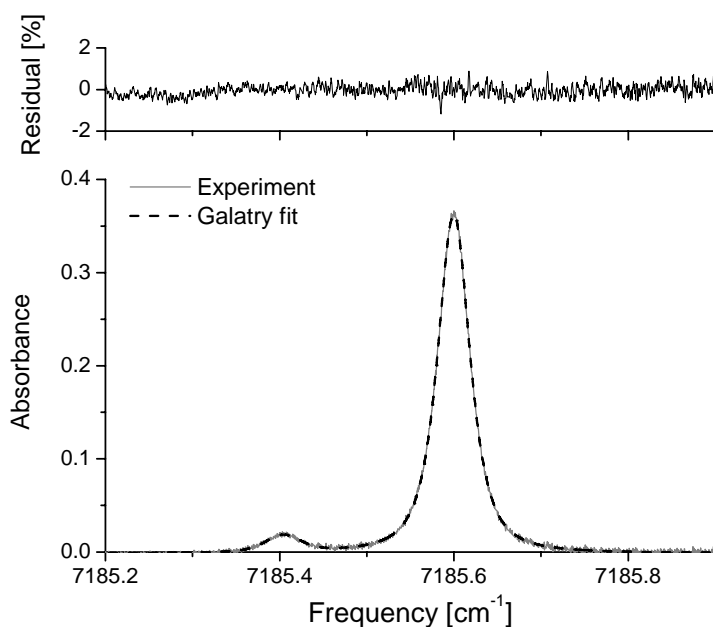
Figure 5.7 Measured absorption spectrum in the heated cell with *P*=1 atm and *T*=1047 K. A least-squares two-line Galatry fit yields X_{H2O}=0.0105. The residual is the difference between data and fit normalized by peak absorbance.
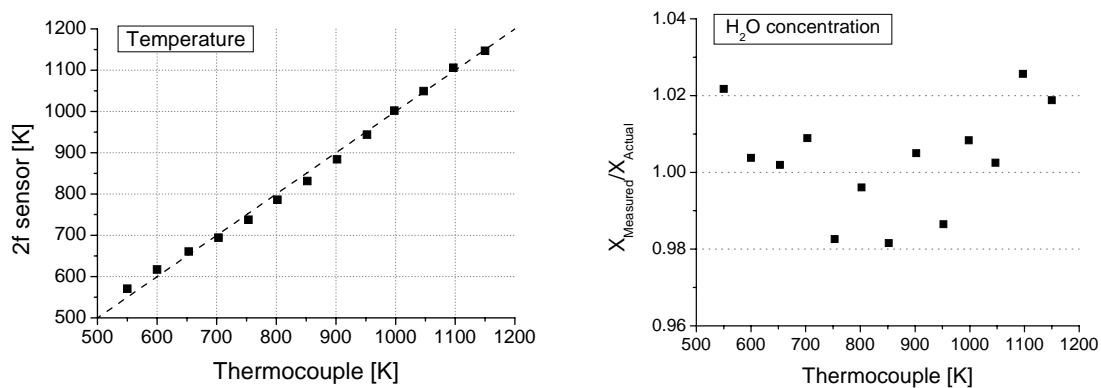
Figure 5.8 Validation measurements of the TDL WMS-2*f* sensor in the well controlled static cell. *P*=1 atm, ~1.0% H_2O in Ar, *L*=76.2 cm. Sensor bandwidth 100 kHz, no averaging.

5.5 Measurements in H$_2$O/Ar shocks

5.5.1 Experimental setup

To illustrate the potential of the WMS-2f sensor for monitoring gas temperature and H$_2$O concentration in studies of the combustion mechanisms of hydrocarbon fuels, shock tube tests are conducted with dilute H$_2$O-Ar mixtures to validate the sensor accuracy and response at combustion temperatures. Figure 5.9 is a schematic of the experimental setup. Experiments are performed behind reflected shock waves in a helium-pressure-driven stainless-steel shock tube, which has been used in previous studies of reaction kinetics [Song *et al.* 2000; Vasudevan *et al.* 2005]. The driven section is 10.5 m long and has an inner diameter of 15.24 cm. Incident shock velocities are measured over four intervals using five piezoelectric pressure transducers (PCB model 11A36) and four counters (Fluke PM6666), allowing accurate determination of the velocity at the shock tube endwall. The pre-shock initial mixture pressure is measured using a 100 Torr MKS Baratron pressure transducer. Reflected shock temperature is calculated from these measured velocities and one-dimensional shock wave relations, assuming vibrational equilibrium and frozen chemistry. The estimated uncertainty in reflected shock temperature is less than ±20 K at 2000 K [Song *et al.* 2000].
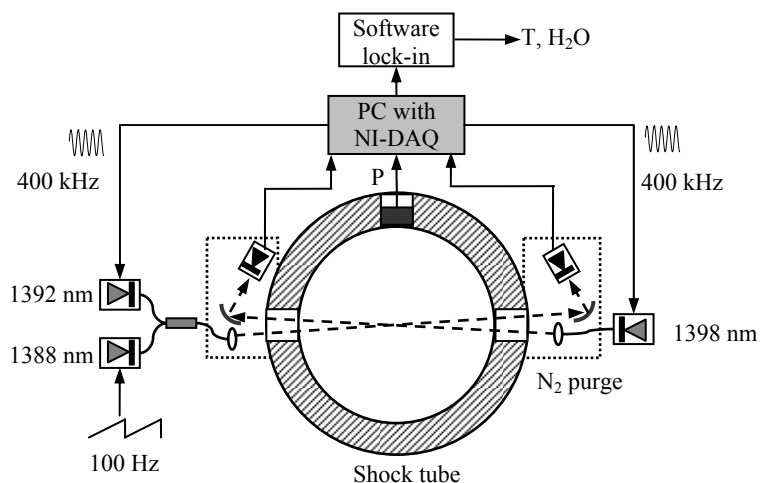
Figure 5.9 Experimental setup for shock tube measurements with the WMS-2f sensor.

TDL measurements are made at a location 2 cm from the endwall. The two diode lasers near 1392 nm and 1398 nm are sinusoidally modulated by 400 kHz digital waveforms generated by a PC running a 10 MHz National Instruments data-acquisition (NI-DAQ) system. The NI-DAQ system consists of a PCI-6115 DAQ board (12-bit A/D conversion) and a BNC-2110 analog I/O block. The modulation depths are adjusted close to the optimal values (section 5.3.2): a=0.059 cm^{-1} for laser 1392 nm and 0.056 cm^{-1} for laser 1398 nm. The corresponding laser intensity modulation amplitude is i_0=0.26 for both lasers. The light from each laser is collimated, transmitted through the shock tube with opposite directions, and focused onto an InGaAs detector (PDA 400). This optical configuration is based on the assumption that the gas properties across the shock tube are uniform. The H_2O concentration in the initial test mixture is determined by direct absorption before the shock for comparison. An additional laser near 1388 nm is used to scan over an absorption feature near 7205.25 cm^{-1} which is strong at room temperature (S(296 K)=0.246 cm^{-2}/atm) [Liu *et al.* 2007c]. The optics and detectors are enclosed in plastic bags purged by dry N_2. The detector signals are recorded at 10 MHz using the same computer. The detector signal is demodulated by a digital lock-in program [Liu *et al.* 2004a; Rieker *et al.* 2007a] on LabVIEW with a low-pass filter bandwidth of 100 kHz to extract the 1f and 2f (X and Y component) signals. An additional Kistler transducer is used to record the pressure time-history at the same location during shock tests.

The test procedure is similar to the one described earlier in last section. Prior to each experiment, the shock tube is evacuated by a turbomolecular pump. The background 1f signal and 2f signal are taken for the lasers 1392 and 1398 nm, and the baseline signal for a direct absorption scan of laser 1388 nm is also taken (with laser 1392 nm off). The shock tube is then filled with the H_2O-Ar mixture to P_1=0.04-0.08 atm. The direct absorption scan for laser 1388 nm is recorded and normalized with the baseline signal to infer the H_2O mole fraction (χ_{Actual}). For this, the laser 1388 nm is then turned off and the laser 1392 nm is turned on. The DAQ system is triggered by the pressure transducer to record pressure and transmission signals for both the 1392 and 1398 nm lasers during the shock heating to infer the time-history of gas temperature and H_2O concentration.

5.5.2 Results

Figure 5.10 shows the measured time-history of pressure and temperature during a shock with initial H_2O-Ar mixture at P_1=0.08 atm and T_1=295 K. The WMS-2f sensor is seen to have a fast response and a good SNR for temperature measurements. The rise time of the sensor is ~6 µs, which approaches the time for the ~1 mm/µs reflected shock wave to across the 2 mm diameter laser beam. The average measured temperature over the time interval 0.1-1 ms (where T and P are expected to be virtually constant) is 1226 K with a standard deviation (i.e., fluctuation) of 14 K (1.1%). This is in excellent agreement (within 1.2 %) with the value calculated from the ideal shock relations, T_5=1211 K. The sensor can also measure the gas temperature after the arrival of the rarefaction wave at about 1.85 ms. The temperature measurement by the WMS-2f sensor is not sensitive to the noise in the measured pressure (as discussed in Section 5.3.2). Thus, the noise in the temperature measurement mostly comes from the laser and detection system.
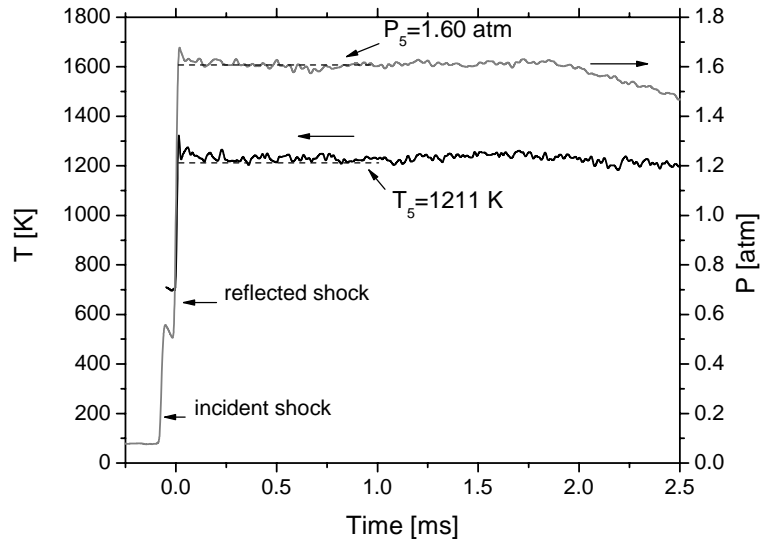
Figure 5.10 Measured temperature and pressure trace during a shock with H_2O-Ar mixture. Initial conditions: P_1=0.08 atm and T_1=295 K; incident shock conditions (calculated): P_2=0.46 atm and T_2=696 K; reflected shock conditions (calculated): P_5=1.60 atm and T_5=1211 K. The decay of pressure and temperature beginning at 1.85 ms is due to arrival of the rarefaction wave.
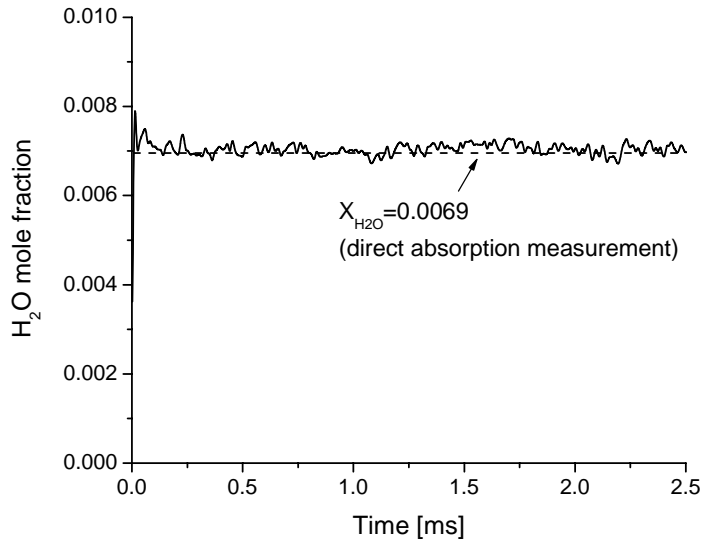
Figure 5.11 Measured water mole fraction by the WMS-2*f* sensor during the same shock as Figure 10 (H_2O-Ar mixture).

Figure 5.11 plots the measured H_2O mole fraction during the same shock test with the WMS-2*f* sensor. The average value measured by both lasers is 0.00702 with a standard deviation of 0.00014. This is in good agreement (within 1.7%) with the direct absorption measurement (0.0069) before the shock. The scatter on the H_2O concentration in Fig. 5.11 comes from the noise in the individual laser signals as well as in the measured temperature and pressure (Fig. 5.10). If T_5 and P_5 are used instead of the measured temperature and pressure, the inferred H_2O mole fraction recovers the expected value with a smaller scatter (0.00008).

Similar tests were performed at different temperatures. Fig. 5.12 provides comparisons of the temperature measured by the WMS-2*f* sensor (averaged over the time 0.1-1 ms) with the calculated T_5. They are in good agreement (within 1.5%) over the tested temperature range of 1200-1700 K. Fig. 5.12 also shows the ratio of the H_2O mole fraction measured by the WMS-2*f* sensor ($\chi_{Measured}$) and the measured mole fraction by direct absorption with the laser 1388 nm before the shock (χ_{Actual}). They agree within 1.4% over the tested range. These results validate the sensor accuracy for temperature

and H$_2$O measurements at combustion temperatures, and illustrate the potential for applications in combustion studies with varying temperature and H$_2$O concentration. The errors in Fig. 5.12 primarily come from the uncertainties in measured spectroscopic data (3%), calculated post-shock temperature T_5 (1%), and errors in the baseline and profile fits (0.5%) in the direct absorption measurements.
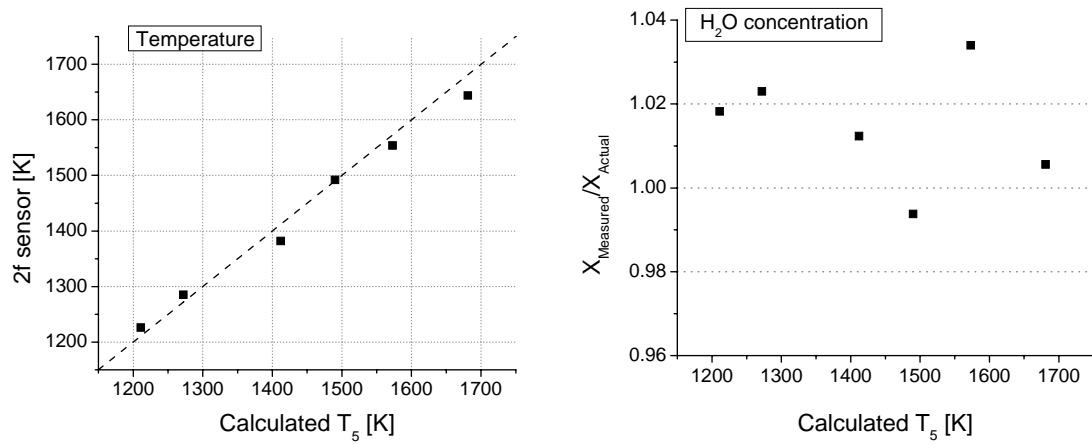
Figure 5.12 Demonstration measurements of the WMS-2*f* sensor in a shock tube with H$_2$O-Ar mixtures. Left: comparison of measured temperature by the WMS-2*f* sensor with calculated T_5; right: comparison of measured H$_2$O by the WMS-2*f* sensor with direct absorption measurement before the shock. P_5=1.3-1.6 atm, ~0.70% H$_2$O in Ar, L=15.24 cm.

Chapter 6

CHEMSHOCK MODEL FOR GAS PROPERTIES
BEHIND REFLECTED SHOCK WAVES

In this chapter, a simple gasdynamic model, called CHEMSHOCK, is developed to predict the temporal evolution of combustion gas temperature and species concentrations behind reflected shock waves with significant energy release. CHEMSHOCK provides a convenient simulation method to study various-sized combustion mechanisms over a wide range of conditions. The model consists of two successive sub-operations that are performed on a control mass during each infinitesimal time step: (1) first the gas mixture is allowed to combust at constant internal energy and volume; (2) then the gas is isentropically expanded (or compressed) at frozen composition to the measured pressure. The CHEMSHOCK model is first validated against results from a one-dimensional reacting computational fluid dynamics (CFD) code for a representative case of heptane/O_2/Ar mixture using a reduced mechanism. The CHEMSHOCK simulation results are then compared to experimental results, for gas temperature and water vapor concentration, obtained using the fast TDL sensor developed in the last chapter. The accuracy of the model is demonstrated for mixtures with no energy release (H_2O/Ar mixture), small energy release (H_2/O_2/Ar mixture), and large energy release (heptane/O_2/Ar mixture).

6.1 Introduction

Well-controlled measurements behind reflected shock waves in a shock tube have been used extensively to provide reaction rate parameters needed to construct new mechanisms and to validate existing models [Curran *et al.* 1998; Hanson and Davidson 2001]. When the heat release of the post-shock chemistry is relatively small, the temperature change due to chemical reactions is insignificant, and the post-shock temperatures are given with sufficient precision by the measured shock velocity and a constant-volume constraint (see [Davidson and Hanson 2004] for detailed discussion). However, it is desirable to test chemical mechanisms for combustible mixtures with significant heat release. For these chemical kinetics shock tube experiments, there is a need for a fast computational model that can provide accurate temperature and species concentrations time-histories, thus enabling quantitative use of experimental data and inference of reaction rate information. This chapter reports the development and validation of such a model called CHEMSHOCK. This model is capable of accurately and efficiently predicting combustion gas temperature and species concentrations behind reflected shock waves. The resulting model provides a convenient simulation method to study various combustion mechanisms over a wide range of conditions.

Ignition delay and flow reactor calculations are often conducted using the CHEMKIN software package [Kee *et al.* 1989; Reaction Design website] with some assumptions, e.g., adiabatic, constant internal energy/volume (U,V) or constant temperature/pressure (T,P) [Davis *et al.* 2005; Saxena and Williams 2006]. However, in reflected shock wave tests, a model which only accounts for constant-U,V or -T,P chemical reactions will be invalid for combustible mixtures that provide significant heat release [Davidson and Hanson 2004]. It is necessary to incorporate resulting gasdynamic changes such as expansion or compression in actual shock tube experiments for times beyond the ignition delay time. In order to deal with this coupling between the combustion and fluid mechanics, an alternative modeling strategy is to employ one-dimensional (1-D) reacting CFD [Owens and Hanson 2007]. While this strategy has the advantage of providing both spatial and temporal profiles, it comes at significant (in 2007) computational expense.

Compared to the 0-D CHEMKIN approach, the CFD approach will be at least *N* times more expensive, where *N* is the number of grid points. The cost of both the 0-D CHEMKIN and 1-D CFD approaches scales nearly quadratically with the number of chemical species in the combustion mechanism. Consequently, the CFD method is only feasible for small chemical mechanisms like the hydrogen/oxygen mechanism, but becomes prohibitively expensive for large combustion mechanisms representative of hydrocarbon fuels, such as heptane.

The simple CHEMSHOCK model preserves the necessary coupling between combustion and gasdynamics, while remaining as computationally inexpensive as the 0-D CHEMKIN approach. The proposed CHEMSHOCK model is essentially an augmentation of the constant-U,V CHEMKIN approach in that it allows for isentropic expansion (or compression) during infinitesimal time steps in addition to the constant-U,V reaction. In order to model the gasdynamics component, we utilize a measured pressure history from the shock tube experiment. Pressure is chosen since it is generally the easiest thermodynamic parameter to measure. By incorporating the experimental pressure data into the model, it is possible to circumvent the complexity and computational expense of the CFD approach. In addition, non-ideal effects such as incident-shock attenuation and boundary layer growth [Petersen and Hanson 2002] are automatically coupled into CHEMSHOCK via inclusion of the measured pressured trace. Provided these non-ideal phenomena only influence the gaseous state at the measurement location via isentropic compressions or expansions, the CHEMSHOCK model remains valid.

6.2 Model development

In this section, three different modeling strategies are discussed for gas temperature and species concentrations behind reflected shock waves, as outlined in Table 6.1. The simplest model will be referred to as the constant-U,V CHEMKIN model, which assumes constant-U,V reaction with negligible gasdynamic interaction. The next, slightly more complex model is CHEMSHOCK, which assumes constant-U,V reaction coupled with

isentropic gasdynamics via a measured pressure trace. The last and most computationally intensive is the 1-D reacting CFD model. Rather than discussing each of these models in order of increasing complexity, the CFD model will be discussed first followed by CHEMSHOCK and then the constant-U,V CHEMKIN model.

In the reacting CFD approach used here, a uniformly-spaced, 1-D grid is used with a reflective wall boundary condition at one end and an extrapolation-based outflow condition at the opposite end. The initial condition is specified by assigning the post-reflected shock state (i.e., T_5, P_5, and gas flow velocity $s_5=0$) to the grid point closest to the reflective wall boundary, while the remainder of the domain is initialized using the state behind the incident shock (i.e., T_2, P_2, and s_2). Different states are shown schematically in Fig. 6.1 on an x-t diagram. The chemical composition of the gas mixture at all grid points is initialized to the pre-combustion state. The simulation is advanced in time until the reflected shock reaches the outflow boundary. As a result, the outflow boundary condition has no impact on the simulated flow field. Using this technique, the computational domain only needs to be long enough to provide the test time of interest, and the expense of modeling the full length of a shock tube is circumvented. However, this technique precludes observing phenomena resulting from the reflected shock interacting with the contact surface or rarefaction wave.

Table 6.1 Comparison of three modeling strategies for combustion gas properties behind reflected shock waves

Model	Chemistry	Gasdynamics	Inputs
Constant-U,V CHEMKIN	Constant-U,V	None	Initial T_5, P_5
CHEMSHOCK	Constant-U,V	Isentropic	Initial T_5, measured pressure
1-D reacting CFD	Constant-U,V	Euler equations	Initial T_5, P_5
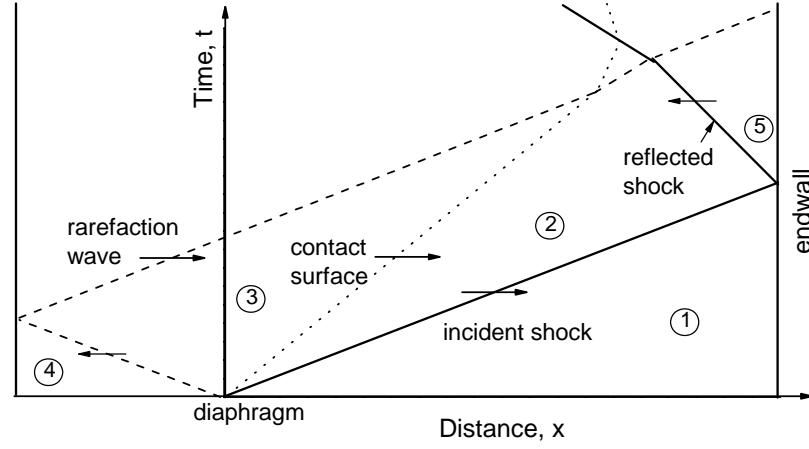
Figure 6.1 Schematic x-t diagram defining parameters in the various regions in a shock tube.

A more detailed description of the numerical methods and equations solved by the 1-D reacting CFD model can be found in [Owens and Hanson 2007]. In brief, the unsteady, 1-D, compressible Euler equations are used to model the gasdynamics with a continuity equation included for each chemical species. The fluid is considered to be mixture of thermally perfect gases. The combustion is modeled using an operator-splitting approach so that during each time step a control volume of motionless fluid is first allowed to react at constant-U,V, and then subsequently a non-reacting fluid is allowed to convect. This operator-splitting strategy has been used successfully by Strang [1968] and Fedkiw *et al.* [1997].

The CHEMSHOCK model developed here also utilizes the same operator-splitting strategy. Each infinitesimal time step *dt* is divided into to two sub-steps. In the first sub-step, the motionless mixture is allowed to react at constant-U,V, as described by the system of differential equations below:

$$\frac{dT}{dt} = -\frac{1}{\rho \bar{C}_v} \sum_{i=1}^{ns} u_i\left(T,Y\right) \dot{w}_i(T,\rho,Y)$$

$$\frac{dY_i}{dt} = \frac{\dot{w}_i(T,\rho,Y)}{\rho}, \quad i=1,...,ns$$

(6.1)

Here T is temperature, Y is a vector of mass fractions, ρ is density, $\overline{C}_v$ is the mixture-averaged specific heat at constant volume, u is the vector of internal energies, $\dot{w}$ is a vector of chemical production rates for all species, and ns is the total number of chemical species. The chemical source term $\dot{w}$ is computed with the aid of a reaction mechanism which consists of a set of elementary chemical reactions of the form:

$$\sum_{i=1}^{ns} v'_{i,n} A_i \Leftrightarrow \sum_{i=1}^{ns} v''_{i,n} A_i \qquad (6.2)$$

Here $v'_{i,n}$ is the stoichiometric coefficient for species A_i and reaction n. The chemical production term for each species can be evaluated by summing the creation and destruction rates in each of the relevant reactions [Owens and Hanson 2007]. In practice, the chemical production rates and other necessary thermodynamic data can be obtained with the aid of the CHEMKIN gas-phase subroutine library [Kee *et al.* 1989; Reaction Design website]. Different chemical mechanisms and species data written in the CHEMKIN format can be easily integrated into the solver.

The characteristic time scales describing the evolution of each of the chemical species can often differ by several orders of magnitude, and consequently Eq. (6.1) needs to be integrated using a stiff ordinary differential equation solver such as LSODE [Brown 1989]. To initialize the integration of Eq. (6.1), the temperature, density, and mass fractions at time t are specified as T_t, ρ_t, and Y_t. By definition, ρ is held constant while Eq. (6.1) is advanced from time t to $t+dt$. After integrating, we obtain new temperature T' and vector of mass fractions Y_{t+dt}, which can be used to define a corresponding pressure P' and a specific heat ratio γ (assuming vibrational equilibrium, which will be used in the next sub-step).

The next sub-step in the CHEMSHOCK model is to let the gas isentropically expand (or compress) from P' to the measured pressure (P_{meas}) while holding the composition frozen at Y_{t+dt}. Assuming vibrational equilibrium, the gas temperature at time $t+dt$ can be determined by:

$$T_{t+dt} = T'\left(\frac{P_{meas}}{P'}\right)^{\frac{\gamma-1}{\gamma}}$$
(6.3)

In Eq.(6.3), P_{meas} has been obtained from the measured pressure history, while all other dependent variables are available from the constant-U,V reaction sub-step. Subsequently, the density is updated to ρ_{t+dt} with known T_{t+dt}, P_{meas}, and Y_{t+dt}. The cycle above can then be repeated with T_{t+dt}, ρ_{t+dt}, and Y_{t+dt} serving as the inputs to the constant-U,V reaction in the next time step. Initially the cycle is started at t=0 by using the calculated temperature and pressure (T_5, P_5) behind the reflected shock as well as the test gas composition.

In the CHEMSHOCK model, the time step dt should be chosen to resolve the fastest occurring phenomena in the system whether this is associated with the combustion reactions or unsteady gasdynamics. In practice, an acceptable dt can be obtained by performing a convergence study to identify the level at which the solution is independent of the time step. During the reaction sub-step, the solution is integrated using the LSODE package, which if necessary will automatically take sub-time steps to meet predefined error criteria. Therefore, it is not necessary to consider the stability criteria of the numerical method used to solve Eq. (6.1) when selecting dt. In the present work, a nominal time step of 1 μs is used throughout.

Lastly, the simplest of the three models is the constant-U,V CHEMKIN model which simply involves integrating Eq. (6.1) over the time of interest. This model does *not* account for compression or expansion of the fluid during reaction. The applicability of this model is thus limited to cases with very small energy release.

In contrast to the 1-D CFD model, both CHEMSHOCK and the constant-U,V CHEMKIN models are 0-D, and consider only a control mass at a specific location in a shock tube. Gasdynamic interactions are neglected in the constant-U,V CHEMKIN model, whereas in CHEMSHOCK they are incorporated through the isentropic relation and the use of pressure data taken at the measurement location. The CHEMSHOCK model is based on the fact that the flow is virtually stagnant behind the reflected shock

wave, and assumes that the compression or expansion of the test gas occurs isentropically and gas properties in the cross section are nearly uniform. The 1-D CFD calculation needs to consider a large flowfield in the shock tube and thus is computationally expensive, while the calculation time of CHEMSHOCK is nearly identical to that of the constant-U,V CHEMKIN model.

6.3 Model Validation

To validate the CHEMSHOCK model, we consider post-reflected-shock reaction in a mixture of 0.2% heptane/2.2% O_2/Ar balance (equivalence ratio ϕ=1), using a reduced heptane mechanism with 49 species and 272 reactions [San Diego mechanism]. Figure 6.2 compares the simulated pressure, temperature, OH concentration, and H_2O concentration behind a typical reflected shock wave (T_5=1350 K, P_5=1.4 atm, produced by an incident shock of speed 0.765 mm/μs propagating into the test gas at T_1=294 K, P_1=40.3 Torr) using the constant-U,V CHEMKIN model and 1-D reacting CFD model. The simulated pressure and temperature by the CFD model are significantly lower than the constant-U,V CHEMKIN simulation due to the gas expansion caused by energy release behind the reflected shock. The inability of the constant-U,V CHEMKIN model to account for gas expansion also causes an earlier rise of OH and H_2O concentrations (though with nearly identical plateau values for H_2O) compared to the CFD results. Clearly, the constant-U,V CHEMKIN simulation overpredicts the gas temperature, pressure, and OH concentration, while slightly underpredicting the ignition time, and thus is not appropriate for cases with large energy release.

In order to make a direct comparison, the simulated pressure using the 1-D CFD model is used as the input to CHEMSHOCK as the pseudo-measured trace. As shown in Fig. 6.2, the predicted temperature and species concentrations (OH and H_2O are shown as representative) by CHEMSHOCK are nearly identical to those simulated by the CFD model. Hence, the application of Eq. (6.3) during each time step is essentially equivalent to the gasdynamic model in the CFD calculations. Similar agreement between CHEMSHOCK and the CFD model has been obtained over a wide range of conditions.
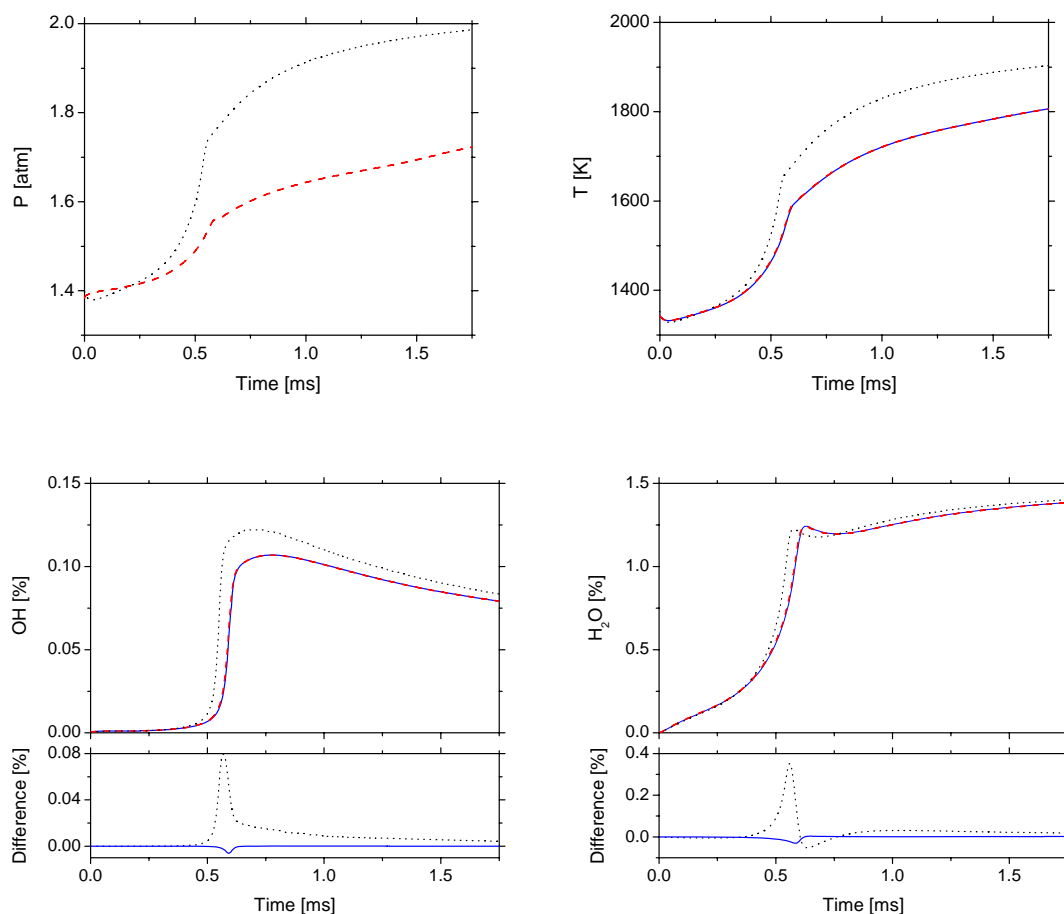
Figure 6.2 Comparison of simulated pressure, temperature, OH concentration, and H_2O concentration behind a reflected shock wave using constant-U,V CHEMKIN (dotted lines), 1-D reacting CFD (dashed lines), and CHEMSHOCK (solid lines; uses the simulated pressure from the 1-D CFD model, see text). Also shown are the differences in the simulated OH and H_2O concentrations between constant-U,V CHEMKIN and CFD (dotted lines), between CHEMSHOCK and CFD (solid lines). Simulation conditions: 0.2% heptane/2.2% O_2/97.6% Ar, P_5=1.40 atm, T_5=1350 K; uses P_2=0.37 atm, T_2=763 K, and gas flow velocity s_2= 482 m/s in the 1-D CFD calculation. San Diego reduced heptane mechanism.

The simulations in Fig.6.2 are conducted on a computer with 3.06 GHz Intel Xeon CPU and 3.0 GB RAM. The simulation time step is 1 μs (with same results obtained for a time step of 10 μs). The computational time for the CFD model is about 24 hours (with 3000 grid points, computational domain 1.5 meters), while the CHEMSHOCK model

takes only ~10 seconds, which is comparable to the constant-U,V CHEMKIN simulation. The CHEMSHOCK model thus reduces the computational time by a factor of ~10^4 compared to the CFD model in this case. This time-savings is especially valuable for reflected shock calculations with large combustion mechanisms. For example, using the same computer, the estimated computational time is ~360 hours for the CFD model and only 2 minutes for CHEMSHOCK when using the reduced heptane mechanism developed by Seiser *et al*. [2000] with 190 species and 1674 reactions.

6.4 Comparison with experimental results

In conjunction with the development of CHEMSHOCK for predicting gas temperature and species concentrations behind reflected shock waves, we have developed a TDL sensor for accurate measurements of temperature and H_2O concentration in Chapter 5. The combination of these tools allows combustion mechanisms of hydrocarbon fuels to be studied. The sensor has been validated in a heated static cell and shock tests with H_2O-Ar mixtures, yielding an overall accuracy of 1.9% for temperature and 1.4% for H_2O concentration measurements over the range of 500-1700 K. In this chapter, the sensor bandwidth is reduced to 25 kHz to improve the SNR in combustion measurements.

Experiments are performed behind reflected shock waves in a helium-pressure-driven stainless-steel shock tube, which has been described in section 5.5. Temperature and pressure behind the reflected shock wave are calculated from the initial temperature and pressure of the reactant gas mixture and the shock speed measured over four intervals using five piezoelectric pressure transducers (PZT), assuming vibrational equilibrium and frozen chemistry. TDL measurements are made at a location 2 cm from the endwall. An additional Kistler PZT is used to record the pressure time-history at the same location during shock tests. The uncertainty in the measured pressure is estimated to be ±1%. As shown in section 5.3, the temperature measured by the TDL sensor is not sensitive to the measured pressure, unlike the measured H_2O concentration. For example, at T=1500 K and P=1.4 atm, a 1% change in gas pressure induces only a 0.1% change in measured temperature, but a 0.5% change in measured H_2O concentration.

6.4.1 H_2O/Ar shocks

Shock tube tests with H_2O-Ar mixtures are first conducted to test the CHEMSHOCK model for a case with no energy release. Figure 6.3 compares the measured and simulated temperature profile during a shock with 0.7% H_2O in Ar as the initial mixture at P_1=59.3 Torr and T_1=295 K. The measured pressure trace (solid curve) is used to infer the actual pressure (dash-dotted curve) by smoothing and removing the artificial overshoot arising from non-ideal gauge response immediately after the reflected shock wave. In the following experiments, the same procedure is used to obtain the pressure needed to determine the gas temperature and H_2O concentration from the absorption sensor measurements. The simulated temperature by CHEMSHOCK (essentially Eq. (6.3) without chemical reaction) using the measured pressure is in excellent agreement (within 1.5%) with the measured temperature behind the reflected shock wave. Note that CHEMSHOCK also successfully predicts the gas temperature in the period following the arrival of the rarefaction wave (at about 1.85 ms).
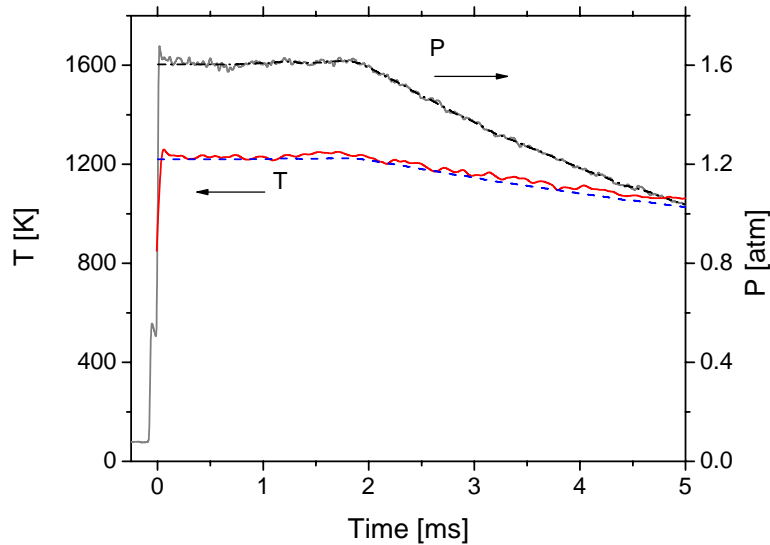
Figure 6.3 Comparison of measured (solid line) and CHEMSHOCK simulated temperature (dashed line) profile during an inert shock with 0.7% H_2O/99.3% Ar mixture. The measured pressure (solid line) is used to infer the actual pressure (dash-dotted line). Initial conditions: P_1=59.3 Torr, T_1=295 K; incident shock conditions (calculated): P_2=0.46 atm, T_2=696 K; reflected shock conditions (calculated): P_5=1.60 atm, T_5=1211 K.

6.4.2 H$_2$/O$_2$/Ar shock

CHEMSHOCK is next applied in a preliminary study of combustion in H$_2$/O$_2$/Ar mixtures in the shock tube to demonstrate its utility for cases with small energy release. Figure 6.4 shows the measured temperature and H$_2$O concentration (solid curves) during a shock with 1.0% H$_2$ and 0.625% O$_2$ in Ar (ϕ=0.8) as the initial mixture. The measured results are compared with simulations using: 1) the hydrogen mechanism developed by Conaire *et al.* [2004]; and 2) the modified GRI-Mech 3.0 [1999] with the measured reaction rate for H+O$_2$+M$\rightarrow$HO$_2$+M by [Bates *et al.* 2001]. This reaction rate is also recommended by Baulch *et al.* [2005], and is in good agreement with the data of [Michael *et al.* 2002]. The heat of formation value for OH from [Herbon *et al.* 2002] is also used in the modified GRI mechanism. In this case, the simulation results for both mechanisms have been artificially shifted by 35 μs to match the measured H$_2$O rise. It is suspected that this early rise is due to impurities in the shock tube, as the high temperature ignition times of H$_2$/O$_2$/Ar are very sensitive to impurities [Davidson and Hanson 2004] (the time shift is actually accomplished by adding 40 ppb of H in the kinetics calculations). This time shift does not affect the post-ignition T, P, or species concentrations values.

It can be seen from Fig. 6.4 that the measured temperature behind the reflected shock wave is in excellent agreement (within 1.5%) with the CHEMSHOCK simulations using both mechanisms. The measured temperature at the early stage is not shown in Fig. 6.4 due to low absorption with small H$_2$O concentrations. Simulation with the modified GRI mechanism provides better agreement with the measured H$_2$O and temperature profiles. Simulated temperatures using these two mechanisms are within 1%, while simulated H$_2$O concentrations differ by 9% around t= 1 ms and by 3% after 5 ms. Again, CHEMSHOCK also successfully predicts gas temperature and species concentrations after the rarefaction wave, illustrating another potential use of CHEMSHOCK and an advantage over the constant-U,V CHEMKIN or the 1-D CFD calculations.
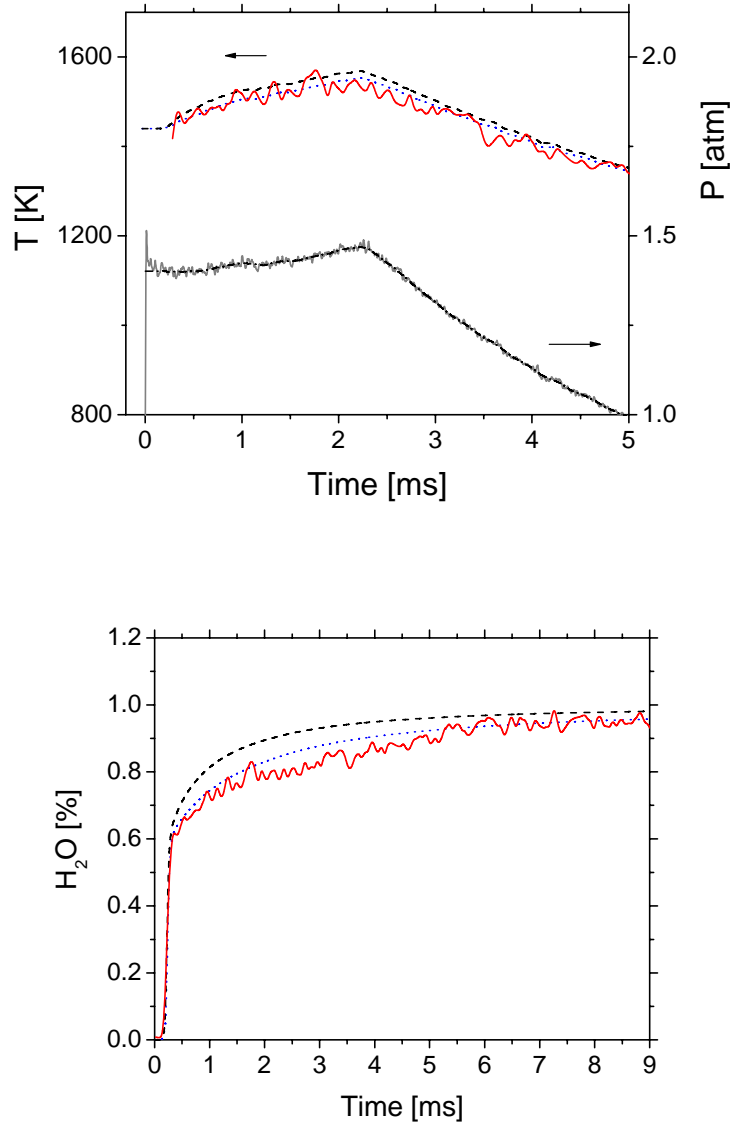
Figure 6.4   Comparison of measured (solid lines) and CHEMSHOCK simulated temperature and H_2O profile during a shock with mixture: 1.0% H_2/0.625% O_2/98.375% Ar; simulations using two mechanisms are shown for comparison: [Conaire *et al.* 2004] (dashed lines) and modified GRI (dotted lines). Initial conditions: P_1=39.0 Torr, T_1=294 K; incident shock conditions (calculated): P_2=0.37 atm, T_2=793 K; reflected shock conditions (calculated): P_5=1.40 atm, T_5=1440 K.

Results from sensitivity analysis for temperature and H_2O concentration using the Aurora 4.1 package [Reaction Design website] and the modified GRI mechanism are shown in Fig. 6.5 for the experimental conditions of Fig. 6.4. The calculated temperature and H_2O profiles are sensitive to the same sets of reactions for these conditions. At the early stage of reaction, T and H_2O are most sensitive to the chain branching reaction $H+O_2<=>O+OH$ (R4). The rate of this reaction is well-known in the temperature range of the present work [Baulch *et al.* 2005]. During the later stages of reaction ($t> 1$ ms), T and H_2O are more sensitive to third-order reactions such as $H+O_2+M<=>HO_2+M$ (R1), $H+OH+M<=>H_2O+M$ (R2), and $2H+M<=>H_2+M$ (R3). Note that the simulated H_2O concentration is about 4 times more sensitive to these reactions than temperature. The rates for these reactions (R1, R2 and R3) also have larger uncertainties. Table 6.2 compares the rate parameters for these three reactions from the two mechanisms (with M=Ar). At T=1500 K, the reaction rates differ by a factor of 1.6 for R1 and a factor of 2.0 for R2. Baulch *et al.* [2005] recommended the same rates for these three reactions as the modified GRI mechanism with different uncertainties. The measured H_2O profile is easily within the uncertainty of the simulation result with the modified GRI mechanism.
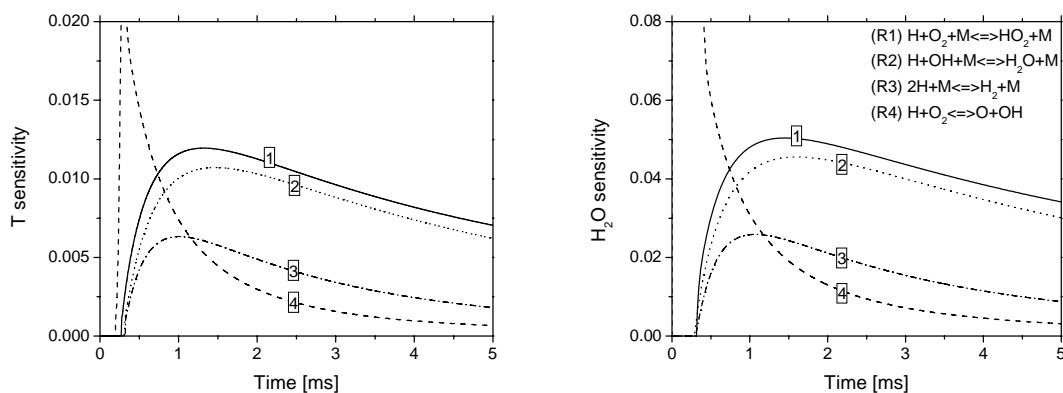
Figure 6.5 Temperature and H_2O sensitivity analysis for the conditions of Fig. 6.4: 1.0% H_2/0.625% O_2/98.375% Ar, P_5=1.40 atm, T_5=1440 K. Modified GRI mechanism. The four most sensitive reactions are shown.

Table 6.2   Comparison of reaction rates from two mechanisms

Reaction	Conaire 2004	Modified GRI[a]	Ratio at 1500K[b]	Baulch 2005[c]
1. $H+O_2+Ar \rightarrow HO_2+Ar$	$2.33\times10^{16}T^{-0.41}\exp(1115/RT)$	$6.80\times10^{18}T^{-1.2}$	1.6	uncertainty 1.5×
2. $H+OH+Ar \rightarrow H_2O+Ar$	$1.71\times10^{22}T^{-2.0}$	$8.36\times10^{21}T^{-2.0}$	2.0	uncertainty 2×
3. $2H+Ar \rightarrow H_2+Ar$	$1.15\times10^{20}T^{-1.68}\exp(-820/RT)$	$6.3\times10^{17}T^{-1.0}$	0.96	uncertainty 3.2×
4. $H+O_2 \rightarrow O+OH$	$1.92\times10^{14}\exp(-16440/RT)$	$2.65\times10^{16}T^{-0.67}$ $\times\exp(-17041/RT)$	1.2	uncertainty 0.3×

[a] with reaction 1 rate from [Bates *et al.* 2001]
[b] ratio of the reaction rate from [Conaire *et al.* 2004] to that from modified GRI
[c] recommended the same rates as modified GRI for the first three reactions, and similar rate for R4

6.4.3 Heptane/O$_2$/Ar shock

Lastly, CHEMSHOCK is applied in an example study of combustion in heptane/O$_2$/Ar mixtures, representing a case with large energy release. Figure 6.6 shows the measured temperature and H$_2$O concentration during a shock with 0.2% heptane and 1.85% O$_2$ in Ar (ϕ=1.2) as the initial mixture. The measurement results are compared with CHEMSHOCK simulations using: 1) the reduced heptane mechanism from [Seiser *et al.* 2000], and 2) the reduced heptane mechanism from [Seiser *et al.* 2000] combined with the hydrogen mechanism from the modified GRI mechanism mentioned above. The measured temperature is in good agreement (within 2.5%) with CHEMSHOCK simulations using both mechanisms (slightly better with the simulation using the mechanism from [Seiser *et al.* 2000]). The measured H$_2$O concentration agrees better with simulation using the hybrid mechanism (Seiser 2000 + modified GRI) for *t*>1.2 ms. This is consistent with the observation in the H$_2$/O$_2$/Ar shock described above. The discrepancy between measurements and simulation results are mostly due to uncertainty in the TDL sensor data [Li *et al.* 2007c] as well as the uncertainties of reaction rates in the mechanism. The noise in the measured temperature in Fig. 6.6 is primarily attributed to the noise in the individual laser signals, while the noise in the measured H$_2$O profile mainly comes from the measured temperature. Further work is needed to reduce the noise and uncertainty in these measurements. For example, improved SNR is anticipated by using stronger H$_2$O absorption features near 2.7 μm [Farooq *et al.* 2007].
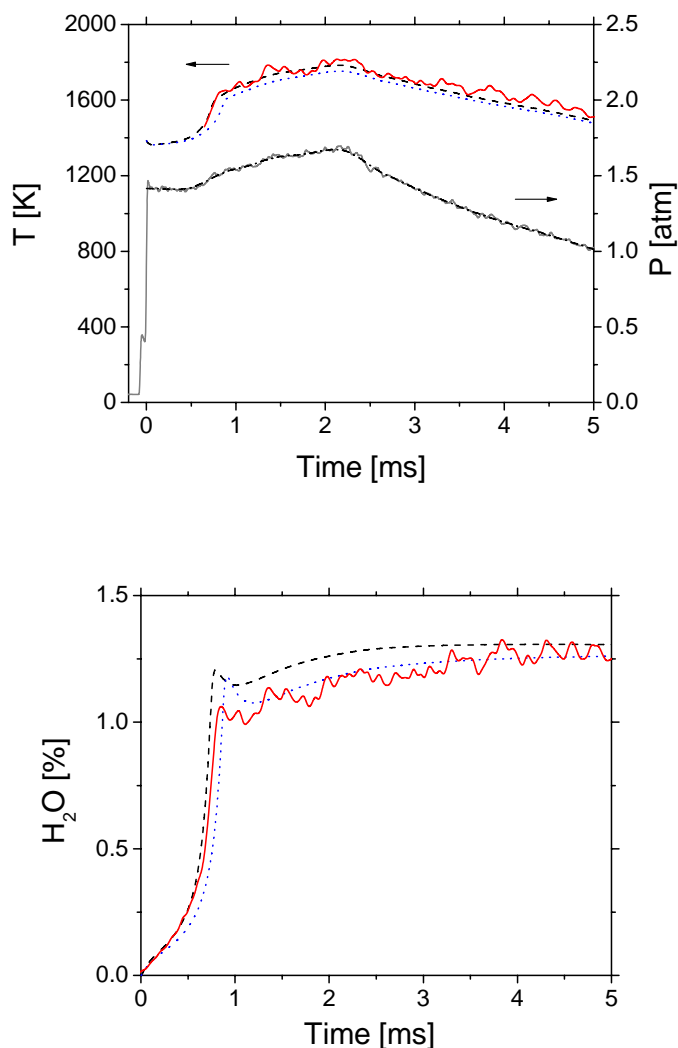
Figure 6.6 Comparison of measured (solid lines) and CHEMSHOCK simulated temperature and H_2O profile during a shock with initial mixture: 0.2% heptane/1.85% O_2/97.95% Ar; simulations using two mechanisms are shown for comparison: [Seiser *et al.* 2000] (dashed lines) and hybrid mechanism (Seiser 2000 + modified GRI, dotted lines). Initial conditions: P_1=39.4 Torr, T_1=294 K; incident shock conditions (calculated): P_2=0.37 atm, T_2=776 K; reflected shock conditions (calculated): P_5=1.42 atm, T_5=1385 K.

Sensitivity analysis for temperature and H_2O concentration using the Aurora 4.1 package and the heptane mechanism from [Seiser *et al.* 2000] are shown in Fig.6.7 with the three most sensitive reactions. Both temperature and H_2O are sensitive to the branching reaction $H+O_2=>O+OH$ and decomposition reactions like C_3H_5-A=>C_3H_4-

A+H. The simulated H_2O concentration is about a factor of 6 more sensitive to these reactions than temperature. As shown in Table 6.2, at T=1500 K, the reaction rates for $H+O_2 \Rightarrow O+OH$ differ by a factor of 1.2 in the two mechanisms. Refinement of the combustion mechanism with reduced uncertainties for these sensitive reactions may improve the agreement with the measurement in Fig. 6.6. Diagnostics for other species such as OH and CO_2 can also be incorporated into the experiments to provide additional information for testing or improving combustion mechanisms, especially for those sensitive reactions.
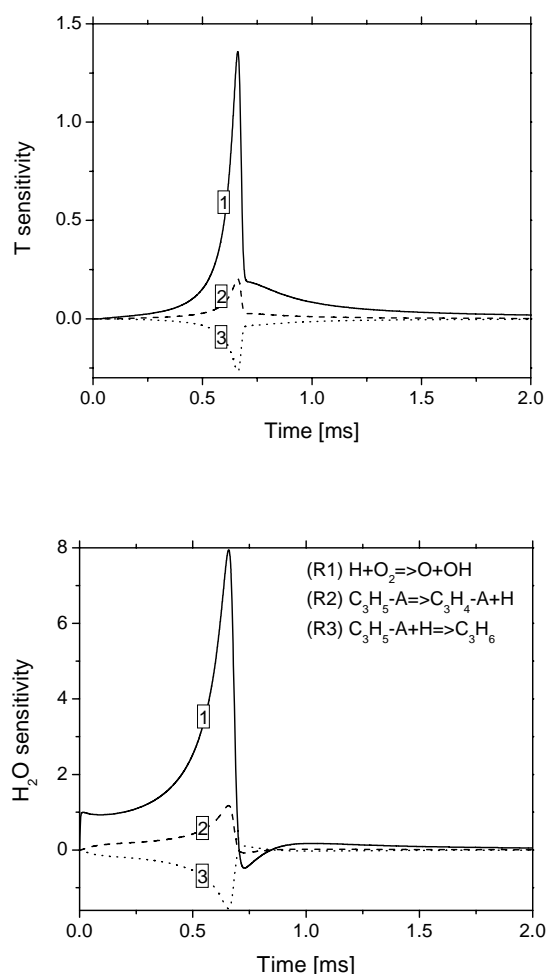
Figure 6.7 Temperature and H_2O sensitivity analysis for the conditions of Fig.6.6: 0.2% heptane/1.85% O_2/97.95%Ar, P_5=1.42 atm, T_5=1385 K. The three most sensitive reactions are shown. Reduced heptane mechanism from [Seiser *et al.* 2000].

Chapter 6

Chapter 7

INSTABILITY CONTROL IN SWIRL-STABILIZED COMBUSTORS

In addition to providing valuable diagnostics for fundamental studies of combustion chemistry, tunable diode laser absorption sensors can also be used for active combustion control. In this chapter, thermoacoustic instability and lean blowout (LBO) are monitored in propane/air flames in a swirl-stabilized combustor using a TDL sensor for gas temperature using wavelength-scanned laser absorption of two neighboring H_2O transitions near 1.4 µm. Detailed experiments are conducted to optimize the position of the sensor line-of-sight in the flame for thermoacoustic instability and LBO sensing. The intensity of low-frequency temperature fluctuations measured by the TDL sensor is used to predict the proximity to LBO and this parameter is used as a control variable for feedback LBO suppression without knowing the LBO fuel/air ratio limit. The TDL sensor results are also compared with traditional pressure and emission sensors. The work presented in this chapter is an extension of the initial work by Zhou [2005c].

7.1 Introduction

Recent efforts to improve power and propulsion systems are mostly directed towards cleaner and more environmentally friendly power generation [Lieuwen *et al*. 2001]. Emissions legislation has motivated the development of combustors that operate at lean fuel/air equivalence ratios, where lower flame temperatures reduce the production of NOx [Martin and Brown 1990; Lefebvre 1999]. In addition, these lean operating conditions reduce engine maintenance because the lower combustion temperatures

increase the lifetime of engine components [Lefebvre 1999]. However, fuel-lean combustion is susceptible to instabilities in the form of thermoacoustic oscillations and LBO, which pose a serious problem for the operation of low-emission gas turbine combustors.

Thermoacoustic instabilities refer to self-sustained combustion oscillations at or near the acoustic frequency of the combustion chamber, which are the result of the closed-loop coupling of unsteady heat release to pressure oscillations (Rayleigh criterion [Rayleigh 1945]). Unstable combustion may lead to decreased combustion efficiency, increased pollutant emissions, and system performance degradation [Lefebvre 1999]. Intensive experimental and theoretical work has been performed during the past decade to understand the driving mechanisms of thermoacoustic instabilities and to develop effective approaches to suppress these instabilities in laboratory-scale or full-scale combustors [Neumeier and Zinn 1996; Lieuwen *et al.* 2001; Dowling and Morgans 2005]. It is well known that heat release fluctuations produce pressure fluctuations; however, the mechanisms whereby pressure fluctuations result in heat release fluctuations are not well understood [Lee and Santavicca 2003]. Equivalence ratio fluctuation [Lieuwen *et al.* 2001; Duan *et al.* 2005] and flame-vortex interaction [Paschereit *et al.* 1998; Lee and Santavicca 2003] are considered to be the most important of these mechanisms in fuel-lean gas turbine combustion systems. Because of the complex physical and chemical interactions involved in thermoacoustic instabilities, it is difficult to predict this unstable combustion behavior. Therefore, typically combustion instabilities have been reduced or eliminated in industrial combustors by passive or active control mechanisms [Paschereit *et al.* 1998; Dowling *et al.* 2005]. Active control strategies utilizing fuel modulation [Neumeier and Zinn 1996] and acoustic forcing [Paschereit *et al.* 1998;] have been successfully demonstrated to decouple the pressure and heat release fluctuations.

LBO usually occurs at lower equivalence ratios or during rapid transient processes, and is also a major concern in modern, highly-loaded land-based and aeroengine combustors. In a stationary gas turbine engine, such blowout events require a time-

consuming system shutdown and restart procedure, which increases maintenance costs and reduces engine lifetime [Thiruchengode *et al*. 2003]. Currently, LBO is prevented by operating the combustor with a wide safety margin above the uncertain LBO equivalence ratio limit. This LBO limit varies with many operating parameters including the air and fuel flow rates, fuel composition, and combustor age [Ateshkadi *et al*. 2000; Thiruchengode *et al*. 2003]. Consequently, NOx emission could be reduced and engine performance could be improved by operating with a narrower LBO safety margin.

A large amount of previous work has been performed to investigate the mechanisms of LBO as equivalence ratio is reduced, with the general finding of a transition between stable flames and LBO that is characterized by an intermediate stage with large-scale unsteadiness, and local extinction and reignition events [Chao *et al*. 2000; Nair *et al*. 2005]. Bradley *et al*. [1998] showed that the flame is stabilized by hot gas in both the inner and outer recirculation zones at steady combustion, whereas the unstable flame near LBO is stabilized only by the hot gas in the inner zone. Several studies showed that if this large-scale unsteadiness is reduced, the LBO limit can be extended to lower equivalence ratios. Based on detection of LBO precursors using OH* chemiluminescence, Thiruchengode *et al.* [2003] extended the LBO limit by modifying the fuel fraction injected into the flame stabilization zone. Gutmark *et al*. [1993] extended the LBO limit of a premixed dump combustor by generating small-scale vortices using shear layer forcing, whereas Sturgess *et al*. [1993] found that the LBO limit can be extended by exit blockage. Durbin and Ballal [1996] observed that the LBO limit was reduced by increasing the outer swirl intensity if the inner swirl is stronger than the outer swirl.

Practical operation of low-emission gas turbine combustors will require real-time active control mechanisms to suppress thermoacoustic instabilities and avoid LBO. An important part of any control strategy is a robust sensor to measure a meaningful control variable. Most frequently used methods for instability sensing include acoustic detection using a microphone or pressure sensor, and emission measurement from OH*, CH*, or CO_2* as a qualitative measure of the heat release rate [Lieuwen *et al*. 2001; Lee and Santavicca 2003; Thiruchengode *et al*. 2003; Duan *et al*. 2005]. However, these are

volume sensors and hence their spatial resolution is generally quite different from the line-of-sight (LOS) diode laser sensor. In addition, microphone sensors for pressure fluctuations are sensitive to background noise (from vibration or flow), and emission sensors may have interference from emissions of other radicals in the flame.

Gas temperature is a key parameter of the combustion process, and thus has potential for use as a control variable in physics-based control strategies. Non-intrusive temperature measurements based on diode laser absorption are particularly attractive and have been demonstrated in a variety of flow fields. In previous work in our laboratory, a wavelength-multiplexed TDL sensor was used in a real-time adaptive control system to increase combustion efficiency and reduce emissions in a waste incinerator [Furlong *et al*. 1996, 1998]. TDL temperature sensors offer potential for improved thermoacoustic instability and LBO control (relative to emission or acoustic sensors) owing to better spatial resolution and insensitivity to background noise and luminosity.

In this chapter, a 2 kHz real-time (i.e., no post-processing) temperature sensor using a single TDL near 1.4 μm is used to detect thermoacoustic instability and the proximity to LBO along an optimized LOS in a swirl-stabilized combustor, which serves as a model of gas turbine combustors. Although gas composition and temperature are not uniform along the LOS, it will be shown that the TDL temperature sensor clearly identifies the high-frequency (hundreds of Hz) periodic oscillations and low-frequency (~10 Hz) fluctuations near LBO. The single-laser temperature sensor is first described, and then used to monitor thermoacoustic instability and characterize the flame behavior near LBO.

7.2 Single-laser temperature sensor

The development of the fast, single-laser temperature sensor for combustion gases has been described in detail previously [Zhou *et al*. 2005a; Zhou 2005c]. In brief, a H_2O line pair near 1.4 μm is targeted for non-intrusive measurements of gas temperature using a scanned-wavelength technique combined with WMS-2f detection. Gas temperature is inferred from the ratio of WMS-2f peak heights of the two selected H_2O lines. The background 2f signal introduced by nonlinear IM is neglected for the small modulation

depth (a~0.047 cm^{-1}) used in this sensor and large amount of H_2O (~10%) encountered in combustion control experiments. The combination of scanned-wavelength and wavelength-modulation minimizes interference from flame emission and beam steering. By using WMS-2f detection, the measurement sensitivity is improved by shifting the detection to higher frequencies where laser excess noise and detector noise are both much smaller. In addition, WMS-2f detection using a lock-in amplifier simplifies data analysis and enables real-time measurements, resulting in a robust temperature sensor that is useful for combustion control applications. Real-time thermometry at 2 kHz has been demonstrated in gas- and liquid- fueled swirl-stabilized flames [Zhou 2005c; Zhou *et al.* 2007].

Figure 7.1 illustrates the simulated WMS-2f spectra for the selected H_2O line pair of the TDL temperature sensor at four temperatures (T=300 K, 1000 K, 1500 K, and 2000 K, P=1 atm, 10% H_2O in air, L=15 cm, a=0.047 cm^{-1}). The selected H_2O line pair has large values of lower state energy: E''=1789.0 cm^{-1} for the line at 7154.35 cm^{-1} and 2552.9 cm^{-1} for the line at 7153.75 cm^{-1}, respectively. This line selection minimizes the interference from ambient water vapor and cold boundary layers, and ensures that the temperature changes measured by the TDL sensor primarily reflect temperature fluctuations in the hottest regions of the burned gas [Zhou 2005c; Li *et al.* 2007b].

Gas temperature can be obtained from the WMS-2f peak height ratio of the two H_2O transitions, and is closely related to the ratio of absorption linestrengths, i.e.,

$$R_{2f} = \frac{S_{2f}(\overline{v}_1)}{S_{2f}(\overline{v}_2)} = \frac{I_0(\overline{v}_1)H_2(\overline{v}_1)}{I_0(\overline{v}_2)H_2(\overline{v}_2)} = \frac{I_0(\overline{v}_1)S_1(T)}{I_0(\overline{v}_2)S_2(T)} \frac{\int_{-\pi}^{\pi}\varphi(\overline{v}_1+a\cos\theta)\cos2\theta d\theta}{\int_{-\pi}^{\pi}\varphi(\overline{v}_2+a\cos\theta)\cos2\theta d\theta}. \quad (7.1)$$

As can be seen from the preceding equation, the WMS-2f peak height ratio is not only a function of temperature through the linestrength ratio, but also a function of gas composition through the effects of the lineshape function. Figure 7.2 plots the simulated WMS-2f peak ratio of the selected line pair as a function of temperature for various values of H_2O mole fraction (P=1 atm). A 20% change in H_2O mole fraction produces a negligible change (1.8%) in the inferred gas temperature. Thus, for combustion gas

conditions, a reliable determination of R_{2f} yields an accurate determination of gas temperature.
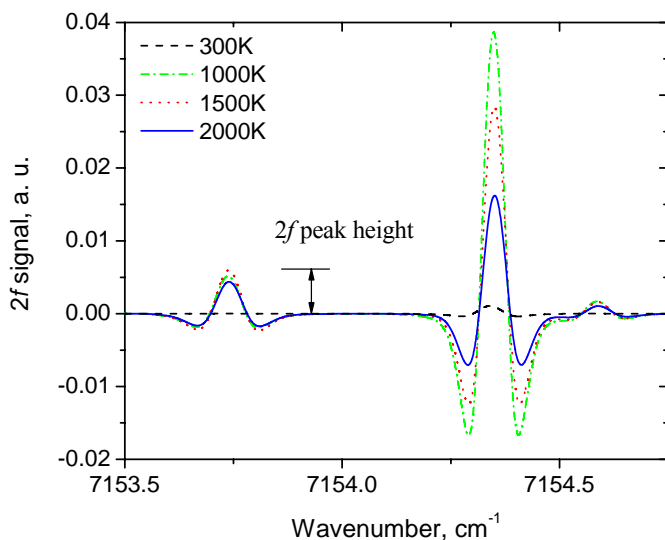
Figure 7.1 Simulated H_2O WMS-2f spectra at 300 K, 1000 K, 1500 K and 2000 K for the TDL sensor. P=1 atm, 10% H_2O in air, L=15 cm, modulation depth a=0.047 cm^{-1}.
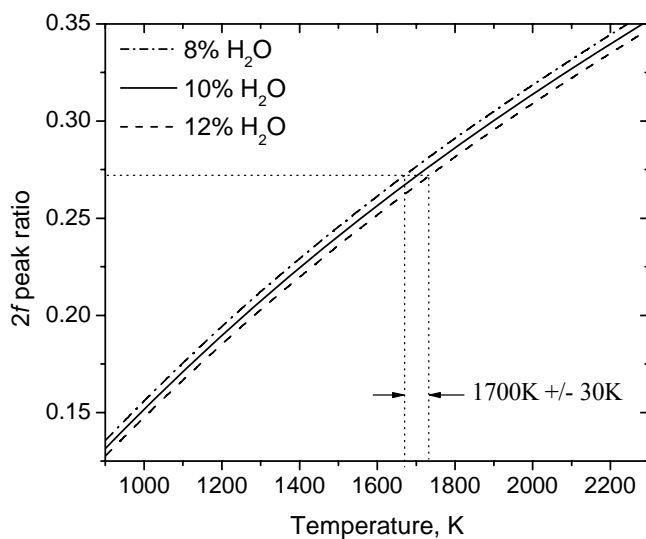
Figure 7.2   Simulated WMS-2f peak ratio for the 7153.75 cm^{-1} /7154.35 cm^{-1} line pair as a function of temperature for various values of H_2O mole fraction. P=1 atm, modulation depth a=0.047 cm^{-1}.

It should be noted that use of the TDL sensor for precise temperature measurements may be complicated by the assumption of uniform gas composition and temperature along the LOS. For the control applications presented here, temperature changes and fluctuations of the flame are more important than the absolute values of temperature. The Fourier power spectrum of a time series of the detected WMS-2f peak ratio R_{2f} provides an excellent measure of temperature fluctuations in the hot burned gases. Furthermore, the WMS-2f peak ratio is insensitive to any signal transmission losses common to the two closely spaced wavelengths of the water vapor transitions. For example, the ratio is insensitive to scattering losses from liquid droplets or transmission losses from window fouling. Therefore, the WMS-2f peak ratio is used in this work as a control variable for both thermoacoustic instability and LBO control experiments.

7.3 Experimental setup

7.3.1 Swirl-stabilized combustor

The atmospheric pressure, swirl-stabilized dump combustor is propane-fueled with a thermal power ranging from 20 to 60 kW, and shown schematically in Fig. 7.3. The combustor configuration was designed as a model of a lean, partially premixed turbine combustor that includes a triple annular research swirler (TARS); the details of this burner design are reported in [Li and Gutmark 2003; Zhou 2005c]. The flow is from bottom to top. A combination of honeycomb and mesh screens is used to create a uniform air flow in the air conditioning chamber. Four identical loudspeakers (75 Watts each) are mounted at the air conditioning chamber for thermoacoustic instability control. The TARS has three air passages and the fuel injection points are uniformly distributed between the outer and intermediate swirlers (see the inset of Fig. 7.3). The diameter of the swirler exit nozzle is d=5.0 cm. An outer (radial, swirler angle 55º in counter clockwise direction), intermediate (axial, 0º), and inner (axial, swirler angle 45º in counter clockwise direction) swirler configuration is used for the current work. The combustion chamber is bounded by a quartz tube (D=9.0 cm diameter, of 45-cm length

for thermoacoustic instability experiments and 20-cm length for LBO experiments), which permits uncooled operation of the combustor and provides optical access for the TDL sensor. The fuel flow and air flow rates are independently controlled by valves and measured using calibrated flow meters. The measurement uncertainty of the equivalence ratio (ϕ) is estimated to be 0.01.
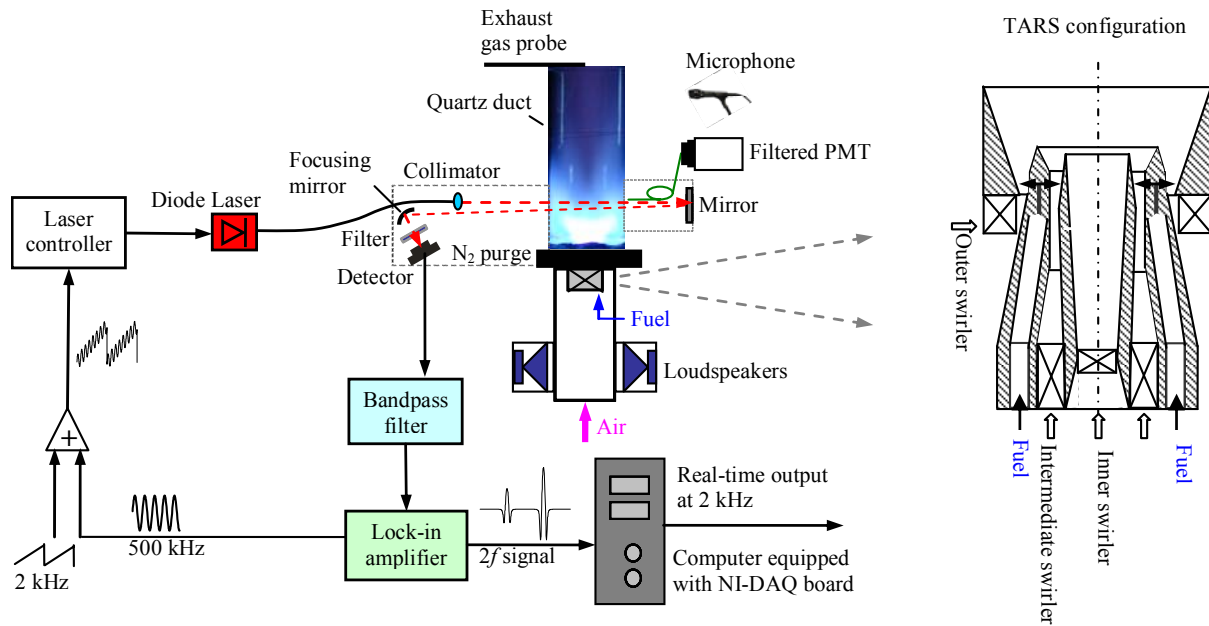
Figure 7.3 Schematic diagram of the real-time TDL temperature sensor and the swirl-stabilized combustor; burner described in detail in [Li and Gutmark 2003].

7.3.2 Measurement techniques

Details of the TDL sensor were described previously [Zhou 2005c], and are only briefly described here. A DFB, fiber-coupled diode laser (NEL, NLK1E5E1AA) operating near 1.4 μm is driven by an external current modulation: a 2 kHz linear current ramp, yielding wavelength tuning over ~2 cm^{-1}, summed with a 500 kHz sinusoidal current modulation generating a=0.047 cm^{-1}. The laser beam is lens collimated and directed across the flame at a height of 5 cm (h/d=1) above the dump plane, which is defined as height h=0. The laser beam is intentionally aligned (2.5 cm, r/d=0.5) off the centerline (r=0) of the duct to maximize the sensitivity of the TDL sensor for instability sensing (see Sections 6.4 and

6.5 for detail). A flat mirror provides a double-pass configuration to improve SNR (total pathlength ~15 cm in the flame). The transmitted laser beam passes through a narrow bandpass filter (NB-1400-030-B, Spectrogon), and is monitored by an InGaAs detector (3 mm diameter active area, 4MHz, Electro-optical Systems). The free space light paths external to the combustion chamber are purged by dry nitrogen to remove interference absorption by ambient water vapor in the room air. The detected signal is filtered with a 320 kHz high-pass filter and a 1.28 MHz low-pass filter (Frequency Devices, Inc.) to remove unwanted frequency components. The second harmonic component of the detector signal is measured with a Perkin-Elmer lock-in amplifier (Model 7280) with a time constant of 1 μs. 2 kHz real-time data processing, including peak finding and ratio calculation, is achieved by a fast PC combined with a laboratory code written in C++ [Zhou 2005c].

Acoustic signals from the flame are measured by a Brüel & Kjær microphone (Model 4939-A-011) located 0.3 m away from the combustion chamber. CH* chemiluminescence is also detected to qualitatively monitor the time-varying heat release. The light emitted by the flame is collected by a fused silicon fiber (placed ~5 cm above the dump plane, shown in Fig. 7.3) in a cone angle of about 23º. The light is filtered by a 10-nm bandpass filter centered at 430 nm, and detected with a photomultiplier tube (PMT, Hamamatsu R928).

The CO and NOx concentrations in the exhaust gas are measured by gas sampling (choked-flow) with a water-cooled quartz probe horizontally placed at the center of the exhaust plane of the combustion chamber. The probe has a tip diameter of 0.6 mm [Schmidt 2001]. The samples are drawn through a cooled water trap (maintained at 3 ºC) and a drying column (filled with indicating DRIERITE desiccant) to reduce the water mole fraction. The dry CO and NOx concentrations are measured with commercial analyzers: MLT NGA2000 analyzer (Rosemount Analytical) and a chemiluminescence NOx analyzer (Teledyne Instruments, model 200E), respectively. Both gas analyzers are zeroed by N_2 and calibrated by span gases before the combustion measurements.

7.4 Monitoring Thermoacoustic instability

In the swirl-stabilized combustor, the flame is stabilized by the recirculation zones in the flow field: a central recirculation zone (CRZ) created by the swirl and an outer recirculation zone (ORZ) created by the sudden expansion [Bradley *et al.* 1998]. Figure 7.4 illustrates the schematic of the flow field and flame structure in our combustor. The recirculation zones produce a region of low velocity with long residence time which allows the flame to propagate into incoming fresh mixture, and thus serve as a source of continuous ignition for combustible fuel-air mixture [Sturgess *et al.* 1992]. In stable combustion, most of the chemical reactions occur between the two hot recirculation zones (see the flame picture in Fig. 7.3), and the flame tip is about 5 cm (h/d=1) above the dump surface.

Since the TDL sensor is a LOS measurement, it is important to optimize the positioning of the laser beam. To investigate the effect of laser positioning, a 100 Hz oscillation was introduced in the flame by modulating the intake air flow with four loudspeakers attached to the air conditioning chamber (Fig. 7.3). To optimize the sensor LOS, measurements were conducted at different horizontal and vertical locations in the forced flame with an air flow rate of 400 SLM [standard liters per minute] and propane flow rate of 9.9 SLM (ϕ=0.58).
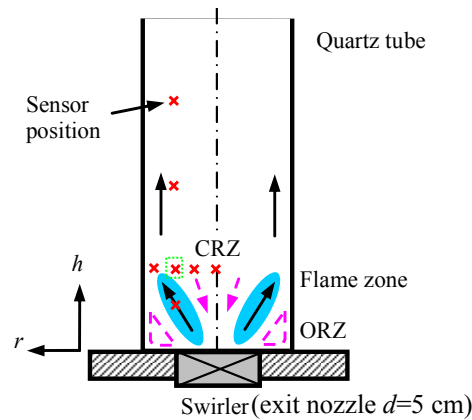
Figure 7.4 Schematic of the stable flame structure with central (CRZ) and outer recirculation zone (ORZ) in the flow field. Also indicated are the investigated TDL sensor locations in the flame. The optimal sensing location is indicated by the green box.

The measured FFT power spectra of the TDL sensor at four horizontal locations ($h=d=5$ cm) are shown in Fig. 7.5. At positions very near wall ($r/d>0.75$), TDL sensor measurements are contaminated by additional low-frequency temperature fluctuations in the boundary layer. At positions near the centerline ($r/d=0.02$), the TDL sensor poorly identifies the temperature oscillation at 100 Hz, because different regions along the sensor LOS oscillate at different phases and the strength of the oscillation is reduced in the path-integrated TDL measurement. We find excellent identification of the flame oscillation in the region $0.2<r/d<0.7$, and hence we selected the location $r/d=0.5$ as the best position for the TDL sensor LOS to monitor temperature oscillations.
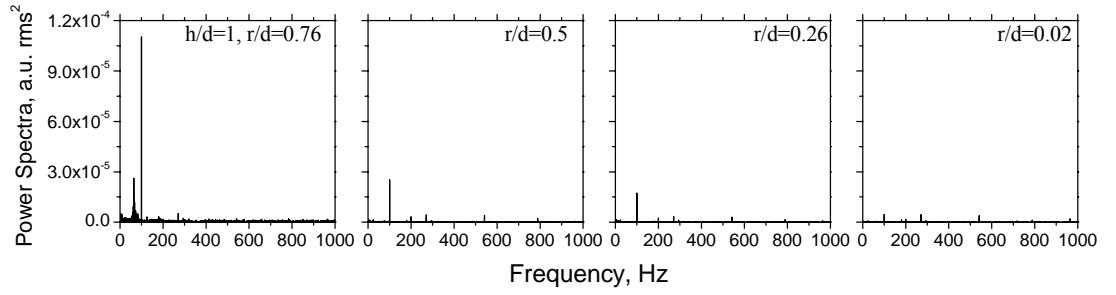
Figure 7.5 Measured FFT power spectra of TDL sensor at 4 horizontal locations in the forced flame, *h/d*=1.
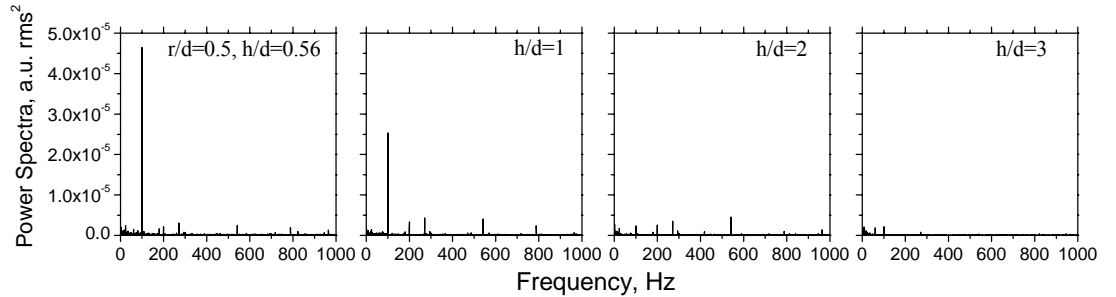
Figure 7.6 Measured FFT power spectra of TDL sensor at 4 vertical locations in the forced flame, *r/d*=0.5.

Similarly we investigated the best vertical position for the TDL sensor LOS. Figure 7.6 plots the measured FFT power spectra of the TDL sensor at four vertical locations (r=2.5 cm). For sensor positions high in the flame (h/d>2), the signature of the oscillation is nearly buried in the noise because of the mixing of gases from the different regions of the combustor. For h/d<0.5, no flame is observed along the sensor LOS due to the flame structure. For the range 0.5<h/d<1.5, the TDL sensor clearly identifies the flame oscillation. These experiments show that the best region for sensing temperature oscillations is near the flame tip (h/d~1 and r/d~0.5); however, good performance (SNR larger than 10) is observed over a wide range of positions (0.5<h/d<1.5, 0.2<r/d<0.7) and the sensor LOS does not need to be precisely located.

The TDL sensor is also used to monitor the natural thermoacoustic instability induced by the round quartz duct [Zhou 2005c; Zhou *et al.* 2007]. Figure 7.7a shows the measured temperature and its FFT power spectrum for a laser LOS near the flame tip with an air flow rate of 820 SLM and propane flow rate of 39.6 SLM (ϕ=1.1). A time resolution of 0.5 ms is achieved with a laser scan rate of 2 kHz; and an FFT is performed on 0.5-seconds of temperature data, providing a resolution of 2 Hz. The measured acoustic signal and CH* chemiluminescence are also shown in Fig. 7.7 for comparison. The dominant oscillation mode (232 Hz) and its harmonic (464 Hz) can be clearly seen from the FFT spectra of three sensors. This oscillation is near the acoustic frequency of the combustion chamber (~225 Hz assuming a sound speed of 450 m/s, tube length 50 cm). This confirms the interpretation of the temperature data: thermoacoustic instability is the coupling of unsteady heat release to acoustic oscillations. The measurements illustrate qualitative comparison of the three sensors, although the positions of the chemiluminescence and acoustic detectors were not optimized and the signal strengths were not calibrated. The TDL sensor has some potential advantages for instability control owing to its spatial resolution and insensitivity to background noise and luminosity. The TDL sensor can accurately identify flame oscillations and can be used in an active control system to suppress these instabilities. A detailed discussion about active control of thermoacoustic instability has been described in [Li *et al.* 2007b; Zhou 2005c].
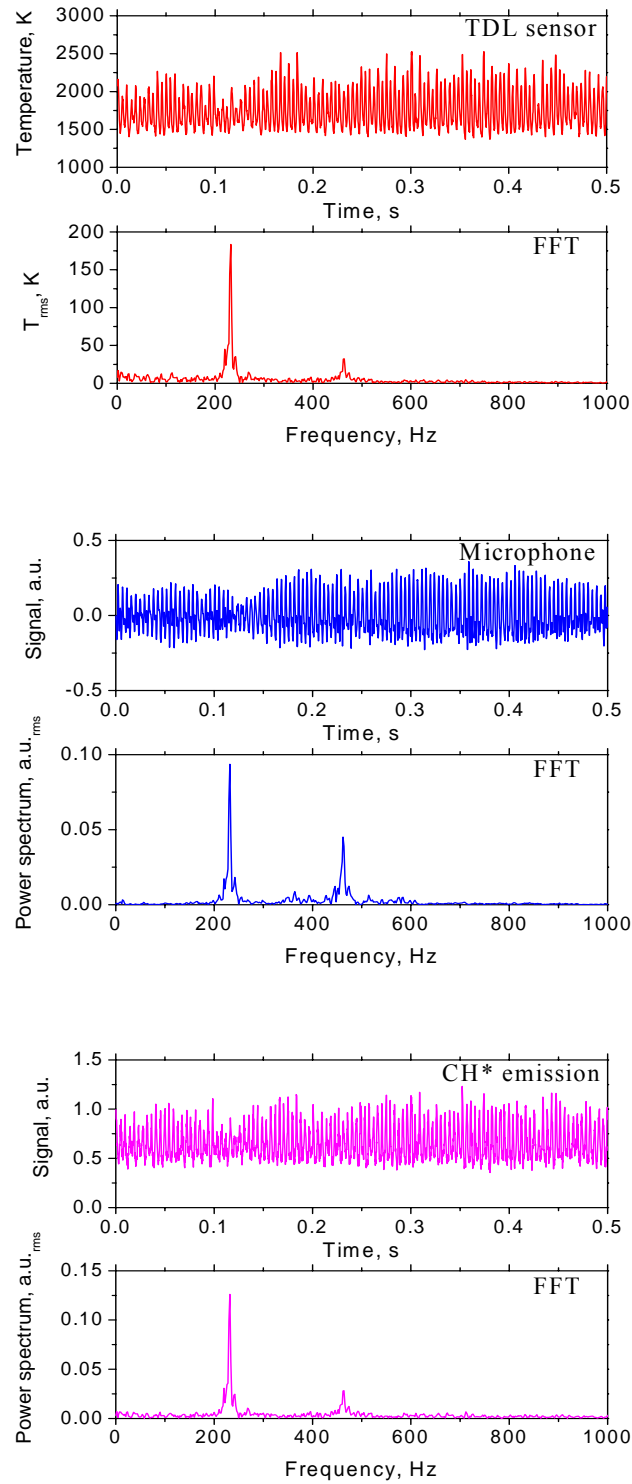
Figure 7.7 Measured signals and FFT power spectra of: a) TDL sensor; b) microphone; c) CH* chemiluminescence. Propane-air flame. Data from [Zhou 2005c; Zhou *et al.* 2007].

7.5 Lean blowout process characterization

The TDL sensor can also be used to characterize LBO process. Figure 7.8 shows the pictures of flame as the fuel is reduced from stable combustion to near LBO for a constant air flow rate. A stable flame is anchored to both the CRZ and ORZ. However, the quenching by flame stretch becomes more important near LBO. There is less heat release between two recirculation zones and more reaction occurs downstream along the wall, resulting in less intense combustion; hence the flame loses its anchor with the ORZ and becomes unstable. These observations are consistent with the recirculation zone stabilization mechanism of a swirl-stabilized combustor reported by [Bradley *et al.* 1998]. These flame structures suggest the best location for the sensor LOS for LBO sensing is the shear layer between the CRZ and ORZ or wall (see Fig.7.4).

| ϕ-ϕ_{LBO}=0.25 | 0.15 | 0.06 | 0.03 | 0.01 |
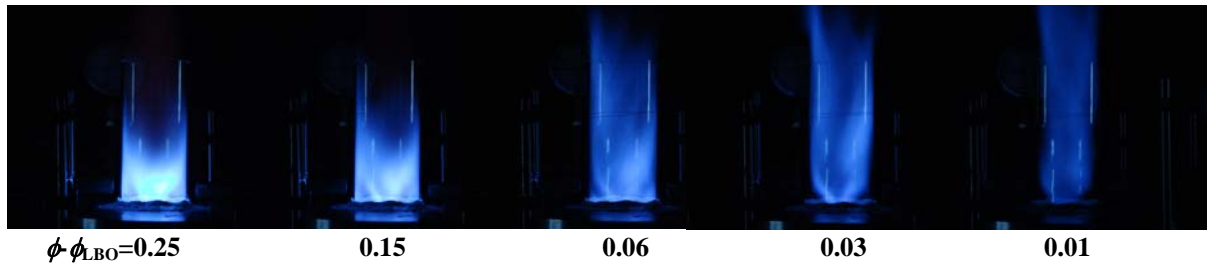
Figure 7.8 Flame structure from stable combustion to near LBO (ϕ_{LBO}=0.44).
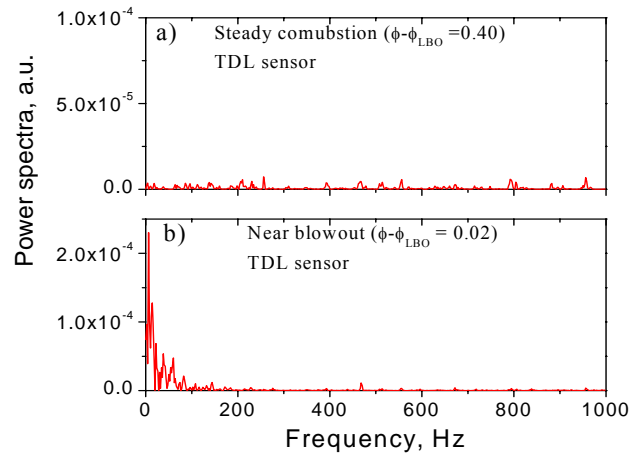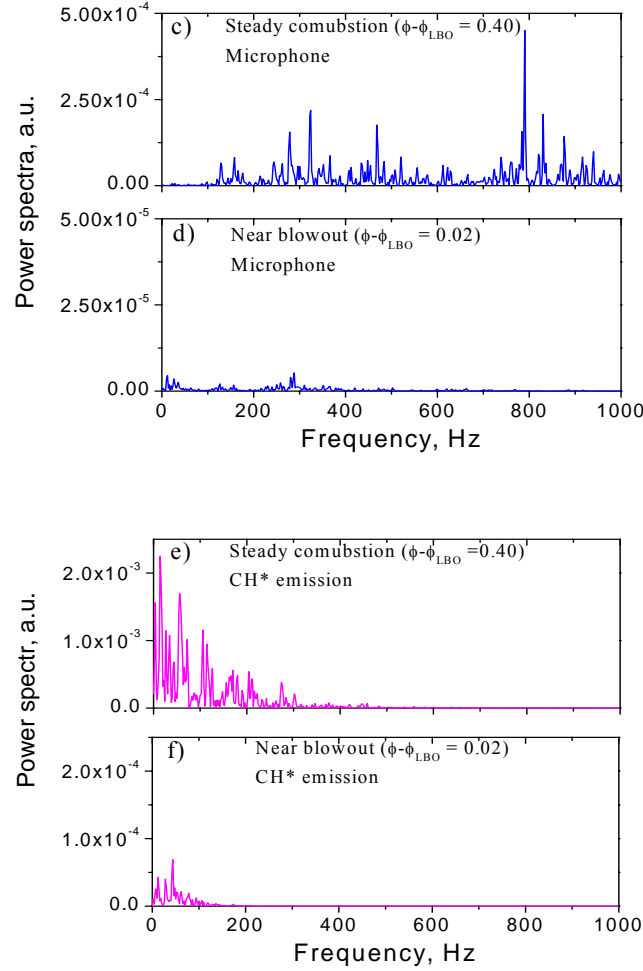
Figure 7.9 FFT power spectra of the TDL sensor, microphone, and CH* emission at two different conditions. TDL sensor location: *h/d*=1, *r/d*=0.5.

The TDL temperature sensor was used to characterize the flame behavior as equivalence ratio was reduced; the first results were presented in [Li *et al.* 2007a]. In these experiments, the fuel flow rate was decreased gradually, while holding the air flow constant, until LBO occurs. The power spectrum is calculated by a FFT algorithm for every 0.5-second series of recorded WMS-2*f* peak ratio. Figure 7.9 plots the FFT power spectra of the TDL sensor at two different equivalence ratios: ϕ-ϕ_{LBO}=0.40 and 0.02 (sensor location: *h/d*=1, *r/d*=0.5). The noise in Fig. 7.9a is nearly white and typical for

steady combustion conditions, whereas the low-frequency fluctuations in Fig. 7.9b are typical for near-blowout conditions. The data in Fig. 7.9b illustrate that these low-frequency components increase significantly as the flame approaches LBO, which is consistent with the increase of local extinction/reignition events. There is no characteristic frequency in the power spectrum since the flame extinction events occur randomly. FFT power spectra of the microphone signal and CH* emission at steady combustion and near LBO conditions are also shown in Fig. 7.9 for comparison. The absolute magnitude of the acoustic and CH* emission signals have large variation from the noisy, bright steady combustion to the quiet, dark flame near LBO. These data illustrate the large dynamic range required for LBO detection with the microphone or emission sensors, whereas the transmitted laser intensity remains strong for flames near LBO. Thus an advantage of the TDL sensing over the traditional sensors for LBO detection is the large signal on a quiet background for the low-frequency temperature fluctuations.

The fraction of FFT power in the 0-50 Hz range, FFT%$_{[0\text{-}50Hz]}$, is used to characterize the low-frequency temperature fluctuations. To investigate the effect of laser beam positioning, measurements were conducted at different horizontal and vertical locations in the propane-air flame. Figure 7.10 shows the measured FFT%$_{[0\text{-}50Hz]}$ as a function of equivalence ratio at 4 different horizontal locations (air flow rate=728 SLM). It is clear that location r/d=0.5 (across the flame) is the best position for the TDL sensor LOS to detect low-frequency temperature fluctuations, which increase sharply as the flame approaches LBO. Approximately 10% of power is in 0-50Hz range when combustion is steady, but increases up to 90% near LBO. At positions very near wall (r/d>0.75), no flame is observed along the sensor LOS near LBO since the flame is located downstream of the sensor. At positions near the centerline (r/d=0.02), we find additional low-frequency temperature fluctuations even for equivalence ratios with stable flames due to the fully reacted gases in the CRZ.

Similar experiments were carried out for different vertical locations (r/d=0.5), as shown in Fig. 7.11. At positions well above the flame tip (h/d>3), additional low-

frequency temperature fluctuations are observed even for stable flames due to the effect of gas mixing. At positions very low in the flame (h/d<0.5), occasionally no flame is observed along the sensor LOS due to the asymmetric flame structure near LBO. Therefore, the most effective location for the TDL sensor for LBO sensing is at the tip of the flame during stable combustion, i.e., h/d~1 and r/d~0.5 for current combustor configuration, which is similar to the optimum position found for thermoacoustic instability detection. Good LBO sensing (contrast between near-LBO and steady combustion larger than 5) is observed over a wide range of positions (0.5<h/d<2, 0.25<r/d<0.6) and the sensor does not need to be precisely located.
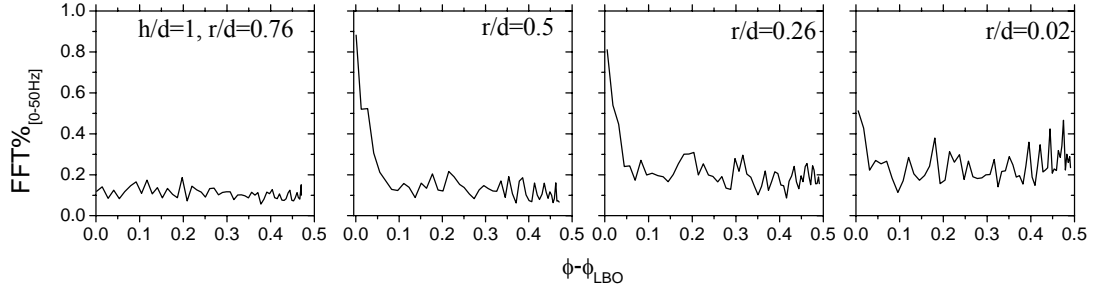
Figure 7.10 Fraction of FFT power in 0-50 Hz of the TDL sensor as a function of equivalence ratio at 4 horizontal locations, *h/d*=1. Air flow rate=728 SLM.
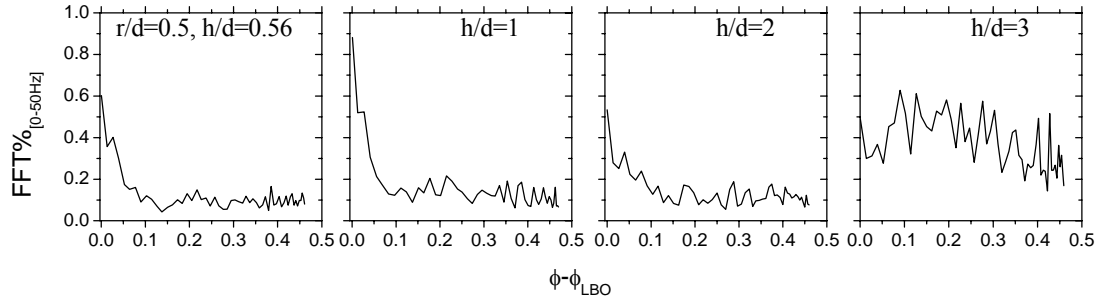
Figure 7.11 Fraction of FFT power in 0-50 Hz of the TDL sensor as a function of equivalence ratio at 4 vertical locations, *r/d*=0.5. Air flow rate=728 SLM.
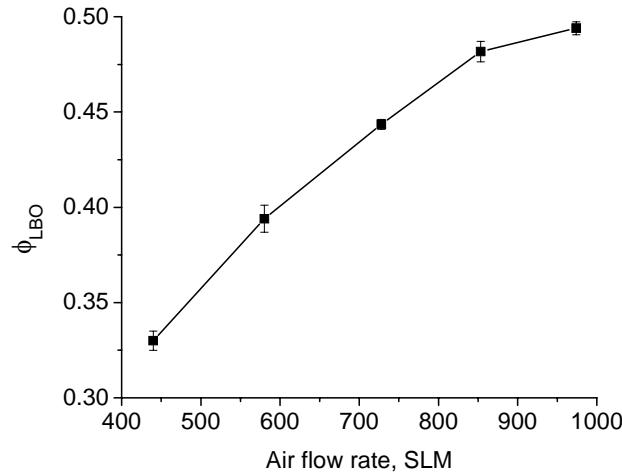
Figure 7.12 LBO equivalence ratio as a function of air flow rate.

Similar behavior was observed at various air flow rates from 440 to 980 SLM. For a specific air flow, the LBO stoichiometry is observed to be repeatable within 0.01; and the LBO limit increases with air flow rate (from 0.33 to 0.49 for the tested air flows), as illustrated by Fig. 7.12.

7.6 Detecting proximity to LBO

The measured increase in low-frequency temperature fluctuations can be used to detect the proximity to LBO without knowing the actual LBO limit for a specific operating condition. Figure 7.13a plots the measured $FFT\%_{[0-50Hz]}$ as a function of equivalence ratio and the best fit to the exponential control model [Li *et al.* 2007a]:

$$FFT\%_{[0-50Hz]} = \frac{T_{rms^2[0,50]}}{T_{rms^2[0,1000]}} = 0.75\exp\left[-(\phi-\phi_{LBO})/0.03\right]+0.12 . \qquad (7.2)$$

A threshold value for $FFT\%_{[0-50Hz]}$ which is larger than all values of $T_{rms^2[0,50]}/T_{rms^2[0,1000]}$ for steady combustion can be set to distinguish near-blowout conditions from steady conditions. As shown by the flame structure in Fig. 7.8, there is an unstable flame range between stable combustion and LBO. This unstable flame range

(ϕ-ϕ_{LBO}<0.05) is successfully identified by the TDL sensor (Fig. 7.13a), and exists for all conditions studied. For this combustor, we found that the same threshold (FFT%$_{[0-50Hz]}$=0.25) is suitable to detect LBO for all air flow rates.
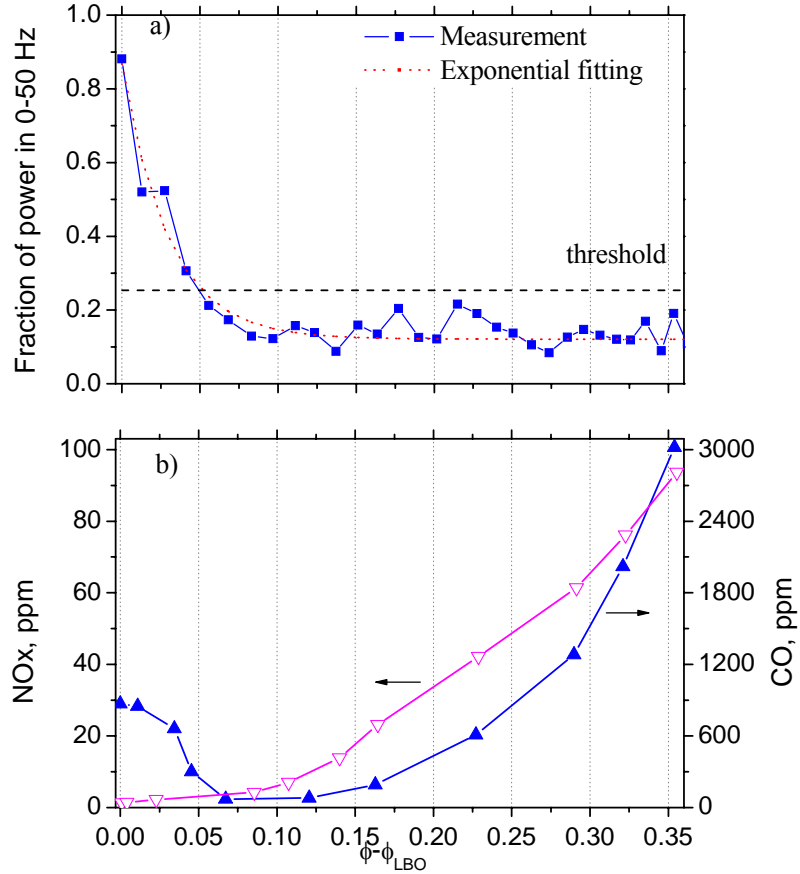
Figure 7.13 a) Fraction of FFT power in 0-50 Hz of the TDL sensor output; b) measured CO, NOx concentrations (dry-based) in the exhaust gas as a function of equivalence ratio. Air flow rate=728 SLM.

The CO and NOx concentrations measured in the exhaust gas are consistent with the LBO sensing with TDL sensor, as shown in Fig. 7.13b. The NOx concentration decreases as equivalence ratio is reduced, mainly due to lower combustion temperature, and a minimum NOx concentration as low as 1 ppm is observed near LBO. The CO

concentration decreases as equivalence ratio is reduced when the flame is stable, but increases near ϕ-ϕ_{LBO}=0.05 as the low-frequency fluctuations begin, in good agreement with the measurements in a similar combustor [Li and Gutmark 2003]. Local extinction and reignition events near LBO lead to reduced combustion efficiency and increased CO concentration. Therefore, for the current combustor, the optimum operating condition for ultra-lean, low-emission combustion is ϕ-ϕ_{LBO}~0.05. Since the LBO limit, ϕ_{LBO}, depends on flow rates as well as other operating parameters, an active control system is required to achieve this optimum operation. The TDL sensor can be used to detect the proximity to LBO and provide a control variable (FFT%$_{[0-50Hz]}$) for the active suppression of LBO.

7.7 Feedback control of LBO

A closed-loop feedback control system for LBO suppression was built using the low-frequency temperature fluctuations as a control variable. FFT is performed on the temperature sensor output, and the fraction of power in 0-50Hz is determined as the feedback control variable for the control system. Two different data acquisition/analysis techniques were utilized. The simplest scheme records 0.5s of data and then calculates the FFT with a calculation time of ~10ms. The second method uses a moving window FFT: i.e., the FFT is calculated every 0.1s on the last 0.5s of recorded data through data buffering. The first method is used in the following experiments to illustrate the control principle. The results obtained for the second method were similar for the current experimental setup due to the relatively slow control valve.

In all control experiments, the air flow rate was held constant at 730 SLM, which corresponds to a bulk average axial velocity of around 2m/s in the combustor under cold conditions, or ~10m/s assuming complete combustion. The fuel flow rate is changed by two electronic proportional valves. Figure 7.14 illustrates the schematic of the setup for LBO control experiment (see Appendix C for detailed description). The main valve (1/8" orifice, 1-5V operating range) opening can be varied with a preset program to modulate the fuel flow rate to simulate load changes. The control valve (3/64" orifice, 0-5V), in parallel with the main valve, is used as the actuator of the LBO control system. The 1/e

response time of the flow control system is estimated to be 0.1s from measurements of the gas temperature in response to a 0.5V step change of the control valve signal. The fuel-flow-delay time from the valve to the combustor is negligible compared to the valve-opening time.
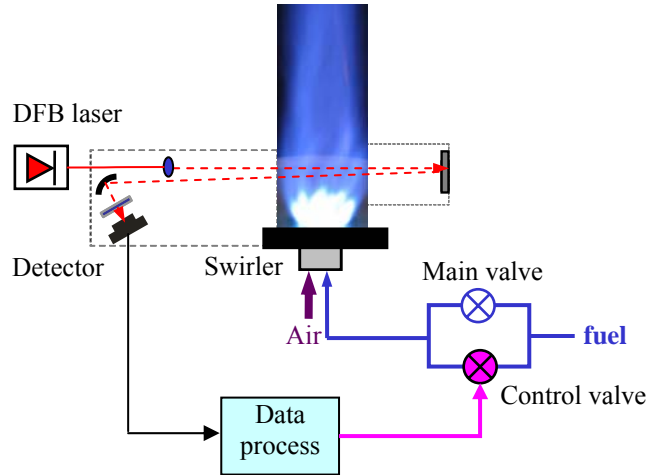
Figure 7.14 Schematic diagram of the LBO control experiment.

The feedback control system was first tested under the case where the main valve was programmed to gradually reduce the fuel flow to simulate engine power reduction. Figure 7.15 shows the time history of the main valve voltage, the low-frequency temperature fluctuations ($FFT\%_{[0-50Hz]}$), and the control valve signal. A threshold for $FFT\%_{[0-50Hz]}$ =0.25 is used for the control regulator. Initially (time=0 in Fig. 7.15), the combustion is stable (ϕ=0.89), and the fraction of the temperature fluctuations in the low-frequency region is about 10% ($FFT\%_{[0-50Hz]}$ ~0.1). As the main valve opening decreases, the low-frequency fraction of the temperature fluctuations ($FFT\%_{[0-50Hz]}$) increases above the threshold at time=20s, indicating the flame is near LBO. The control valve signal (initially 1.0V to facilitate control) is increased proportionally to the difference between $FFT\%_{[0-50Hz]}$ and the threshold to prevent LBO. The measured overall equivalence ratio is also shown in Fig. 7.15. As indicated by Fig. 7.15, without knowing the actual LBO limit, the flame is maintained even when the main valve is fully closed. To our knowledge, this

is the first application of laser-based sensors in LBO control of swirl-stabilized dump combustors.
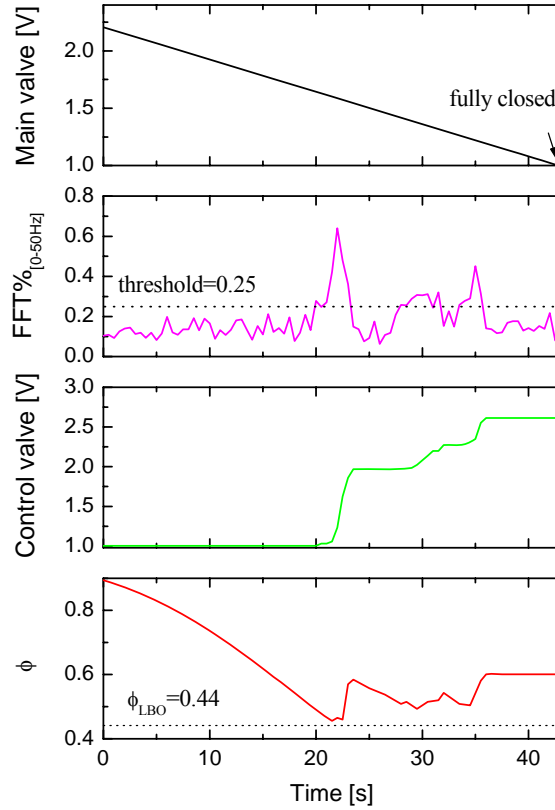
Figure 7.15   Control to prevent LBO during power reduction.

The second control demonstration maintains a stable flame in the combustor with a minimal equivalence ratio (thus minimum LBO margin). As mentioned above, the LBO limit is uncertain for turbine engine combustors. This requires a wide safety margin in engine design to prevent LBO at the worst-case operating conditions. We show the feedback control system can be used to maintain the flame at very lean conditions (near LBO) without knowing the actual LBO limit. For this demonstration, the main valve is closed, and the control valve is used to achieve a minimum fuel flow to maintain the flame, and a threshold of 0.3 is chosen. When the $FFT\%_{[0-50Hz]}$ is below the threshold, the fuel flow is decreased gradually until the $FFT\%_{[0-50Hz]}$ increases above the threshold.

Then the regulator increases the fuel flow to avoid LBO. The performance of the control system is shown in Fig. 7.16, where the controller attains a nearly stationary condition with an average equivalence ratio of 0.47, slightly larger than the LBO limit of 0.44. Thus, the feedback control system can greatly reduce LBO margin to ~0.03 without knowing the actual LBO limit. When operating conditions (e.g., fuel composition) change, this control system can also be used to track the actual LBO limit without turning off the engine. The effects of different thresholds were also investigated; a threshold of 0.25 yields slightly higher mean equivalence ratio ($\phi = 0.49$), but larger thresholds (0.30-0.45) yield almost the same results ($\phi = 0.47$). This result is consistent with the control model of Eq. (7.2).
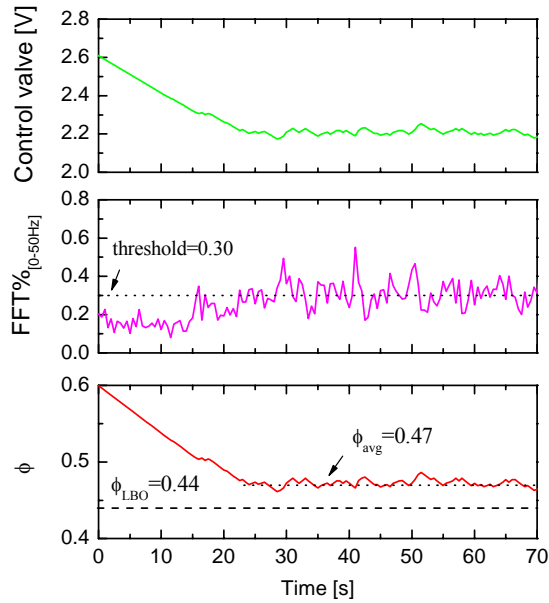
Figure 7.16 Control to maintain flame at very lean conditions.

The engine load (power output) changes during transient processes. A feedback LBO control system needs to prevent LBO without residual effects, i.e., adding fuel only when necessary (near LBO). Thus, the control valve should return back to the initial setting when the flame is stable. The control system was demonstrated for a transient process by modulating the fuel flow with the main valve as shown in Fig. 7.17. Note the controller

does not take action until the LBO is approached (time=18s). The control system successfully prevents LBO by adding fuel for 18<*t*<30s. When the fuel flow through the main valve is sufficient to maintain the flame (time ~35s), the controller returns to the initial setting. More advanced control strategies are of course possible, depending on the specifics of the combustor instabilities and the actuators available.
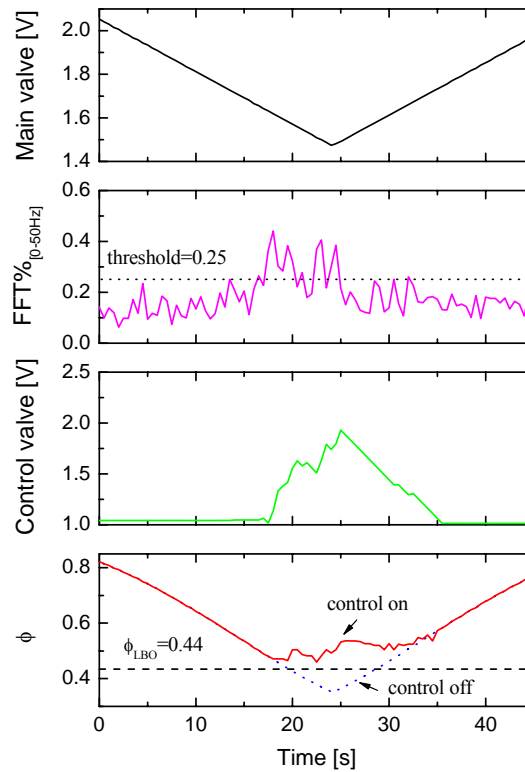
Figure 7.17 LBO control during transient process.

The response time of the current control system is limited to 0.1 s by the actuator, which can be improved by using faster valves. The LBO sensing rate also can be further increased, e.g., by using time-averaged temperature (WMS-2f peak ratio). To prove these assertions, we have used a 0.05s-averaged R_{2f} signal as the control variable and set the threshold at a learned value through the same procedure as Fig. 7.16. Feedback control based on this R_{2f} signal was then successfully applied to prevent LBO in the swirl-stabilized combustor in the same test (and with equivalent results) as Fig. 7.17. Using the

same hardware, the sensor bandwidth could be increased to 10 kHz, and a moving-window FFT could provide an LBO control rate of 100Hz, a value sufficient for many practical LBO problems.

Chapter 8

SUMMARY AND FUTURE WORK

8.1 Summary of spectroscopic measurements

8.1.1 H$_2$O linestrength and self-broadening measurements

High-resolution absorption lineshapes of NIR H$_2$O transitions suitable for short-path and long-path applications have been recorded in a heated static cell as a function of temperature and pressure using DFB diode lasers. The measured absorption spectra for pure H$_2$O are fit with both Voigt and Galatry profiles. It is found that the collisional narrowing effect induces a relatively small error for line strength (<1%) and self-broadening coefficient (<1.8%) measurements with pure water vapor. The measured line strengths and self-broadening coefficients are compared to previously published data, and provide improvements in the H$_2$O spectroscopic database for gas sensing applications.

8.1.2 TDL sensor for coal-fired power plants

A fiber-coupled diode laser sensor system based on direct absorption spectroscopy techniques has been developed (through collaboration with Zolo Technologies Inc.) for the first time to quantitatively measure gas temperature and water vapor concentration in the harsh environment of coal-fired power plants. The long path lengths in these facilities limit the choice of H$_2$O transitions for quantitative absorption measurements. Nine weak H$_2$O transitions suitable for long-path applications are well characterized in the gas cell with multi-pass configuration (path length ~3.8 m) to determine the spectroscopic parameters. Three fiber-coupled diode lasers near 1400 nm are multiplexed for

simultaneous measurements of absorption at five H_2O transitions along a common path in the combustion chamber. The fiber-coupled sensor also facilitates multiple path measurements. The field measurement results (through collaboration with Zolo Technologies Inc.) at a TVA 280 MW coal-fired power plant demonstrate the utility of the diode laser sensor for rapid *in-situ* measurements of important combustion parameters for combustion optimization in large-scale facilities.

8.1.3 Ar-perturbed H_2O lineshape measurements

A strong collisional-narrowing effect is observed in the Ar-broadened H_2O spectra (near 7185.6 and 7154.35 cm^{-1}) at near-atmospheric pressure due to the relatively weak collisional broadening induced by Ar-H_2O collisions. The Ar-induced broadening, narrowing and shift coefficients are determined as a function of temperature using Galatry fits to the absorption data. As predicted by theory, the collisional narrowing parameters have similar temperature dependence to the broadening coefficients. To the best of our knowledge, this is the first determination of temperature-dependent Ar-induced narrowing coefficients for H_2O transitions in the near-IR. These measurements provide a critical spectroscopic database for TDL absorption measurements of temperature and H_2O concentration in Ar-diluted mixtures being used to study combustion kinetics mechanisms.

8.2 Summary of WMS including read diode laser performance

Wavelength modulation absorption spectroscopy with $2f$ detection provides a promising strategy for measuring temperature and species concentration in high-pressure gases using large modulation depths. When a diode laser is injection current modulated over a large wavelength (frequency) range, the phase shift between frequency modulation and intensity modulation and the nonlinear intensity modulation become important for quantitative understanding of the WMS $2f$ signal. These effects are specific to individual lasers and laser settings, and become more pronounced at large modulation depths. Real diode laser performance is characterized and included for the first time in the WMS

model for accurate interpretation of the signals. The measured intensity modulation is found to be well characterized by the combination of 1f and 2f terms with phase shifts. Explicit expressions are presented for the 2f and 1f signals with these effects included. Digital lock-in detection of 2f magnitude is performed to remove the dependence on detection phase. The model improvements are demonstrated and validated by probing pressure-broadened water vapor features near 1388 nm using NIR diode laser. The effects of the non-ideal performance parameters of commercial diode lasers are especially important away from line center of discrete spectra, and these contributions become more pronounced for 2f signals with the large modulation depths needed for WMS at elevated pressures. It is also shown that normalizing the 2f signal by 1f signal can remove the need for calibration when the diode laser performance parameters are characterized and used in the data interpretation.

8.3 Summary of rapid TDL sensor for shock tube

A NIR tunable diode laser absorption sensor based on wavelength modulation spectroscopy with second-harmonic detection is developed for rapid measurements (bandwidth 100 kHz) of temperature and H_2O concentration in shock-heated gases. The sensor is based on TDL absorption of two H_2O transitions near 7185.60 cm^{-1} and 7154.35 cm^{-1}, which are selected as the optimum line pair (based on design rules) for the target temperature range of 1000-2000 K and pressure range of 1-2 atm. The laser modulation depth for each H_2O transition is optimized to maximize the WMS-2f signal for the target test conditions. The fast response of the TDL sensor is achieved by fixing the laser wavelengths near the line center of corresponding H_2O transitions, and set by the digital lock-in bandwidth (currently 100 kHz). Normalization of the WMS-2f signal by the 1f signal is used to remove the need for calibration and minimize interference from emission, scattering, and beam steering. To our knowledge, this is the first realization of a temperature sensor with a 100 kHz bandwidth using a WMS-2f technique.

The WMS-2f sensor is first validated in a controlled laboratory environment (heated static cell) for the temperature range of 500-1200 K (P=1 atm). Temperature

measurements are within 1.9% of thermocouple readings, and H_2O concentration measurements are within 1.4% of expected values. Shock tests with non-reactive H_2O-Ar mixtures are then conducted to demonstrate the sensor accuracy and response at higher temperatures (1200-1700 K, P=1.3-1.6 atm). Temperature measurements are within 1.5% of calculated values from the ideal shock relations, and H_2O concentration measurements are within 1.4% of expected values. This fast-response WMS-2f sensor provides a new diagnostic tool for shock tube experiments and is currently being used to study the thermal decomposition and oxidation of hydrocarbon fuels.

8.4 Summary of CHEMSHOCK model for gas properties behind reflected shock waves

A simple gasdynamic model called CHEMSHOCK has been developed to predict combustion gas temperature and species concentrations behind reflected shock waves with significant energy release. CHEMSHOCK is based on combining constant-U,V reaction with isentropic expansion (or compression) to the measured pressure for a control mass of gas mixture in infinitesimal time steps. The computational time for the proposed model is significantly reduced relative to more exact 1-D reacting gasdynamics codes. The CHEMSHOCK model is first validated with 1-D reacting CFD calculations using a reduced heptane mechanism, and then compared to the measured gas temperature and H_2O concentration by the TDL absorption sensor summarized in section 8.3. Excellent agreement is found between the simulations and measurements in shock tests with H_2O/Ar (no energy release), H_2/O_2/Ar (small energy release), and heptane/O_2/Ar (large energy release) mixtures.

CHEMSHOCK offers several advantages over constant-U,V CHEMKIN or reacting CFD calculations for predicting combustion gas properties behind reflected shock waves. By incorporating the measured pressure, CHEMSHOCK efficiently models the combustion in mixtures with significant energy release. In addition, it successfully predicts gas temperature and species concentration after the rarefaction wave. Therefore, CHEMSHOCK provides a convenient simulation tool, in conjunction with diagnostics

for pressure, temperature, and species (e.g., OH, H_2O, and CO_2), to study various combustion mechanisms over a wide range of conditions.

8.5 Summary of instability control in gas-turbine model combustor

A tunable diode laser temperature sensor has been applied to monitor thermoacoustic instability and LBO in propane/air flames in an atmospheric pressure, swirl-stabilized combustor which serves as a model of gas turbine combustors. This is an extension of the initial work by Zhou [2005c]. The real-time (2 kHz) temperature sensor is based on TDL absorption of H_2O in the NIR, and uses only one telecom fiber-coupled DFB diode laser. Detailed experiments are conducted to optimize the position of the sensor LOS in the flame for thermoacoustic instability and LBO sensing. The TDL sensor accurately identifies the frequency, phase, and amplitude of the flame oscillation, and can be utilized in the feedback control system to suppress the thermoacoustic instability.

A feedback LBO control system including sensing, actuation and control algorithms has been developed and demonstrated in the gas turbine model combustor. The TDL sensor is successfully applied to characterize the LBO process. It is found that low-frequency temperature fluctuations increase near LBO, with the fraction of FFT power in the 0-50 Hz range increasing sharply. These low-frequency temperature fluctuations are used to sense the proximity to LBO and as a control variable for the feedback LBO control system. Without knowing the actual LBO limit, the control system can successfully prevent LBO during power reduction and transient fuel variation. The feedback control system can maintain the flame at very lean conditions near blowout, and reduce the LBO safety margin to 0.03 above the LBO equivalence ratio.

The TDL sensor can offer some advantages over traditional pressure and emission sensors for instability and LBO sensing. These advantages can arise because of the TDL sensor's localized LOS. In addition, the TDL sensor is insensitive to background acoustic noise and flame emissions. Traditional sensors have diminished signals when the flame approaches LBO, whereas the TDL signal remains strong.

133

8.6 Future work

8.6.1 Combustion diagnostics

This thesis presents the development and application of TDL sensors based on H_2O absorption near 1.4 μm for a variety of reactive systems. The same strategy can be used to extend such sensors to other wavelengths (e.g. ~2.7 μm) with stronger absorption features to achieve higher SNR measurements. Diode lasers in the mid-IR are becoming more robust due to improvements in laser technology. Either the fixed-wavelength direct absorption or WMS-2*f* technique can be used in sensor design to increase the sensitivity of temperature and H_2O concentration measurements in short-path applications like the shock tube. The stronger features should provide reduced noise and uncertainty, making it easier to obtain the precise measurements needed to distinguish different combustion mechanisms.

Similar strategies can also be applied to design sensors for other species. CO_2 sensing in the mid-IR is particularly promising due to the relatively strong absorption near 2.7 μm. CO_2 is also a major combustion product of hydrocarbon fuels. In addition, CO_2 may be added into the test gas mixture to improve the absorption signal. Thus, CO_2 can also be chosen as the target absorbing species to be probed in the shock tube. Combined diagnostics for temperature and species (OH, fuel, H_2O, and CO_2) could provide very useful information to study combustion mechanisms.

8.6.2 Shock tube study of combustion mechanisms

CHEMSHOCK model provides a convenient simulation method to study various combustion mechanisms over a wide range of conditions. This model provides the ability to model the combustion mixtures with significant heat release. This extends the parameter spaced for shock tube studies of combustion chemistry. It can be used, in conjunction with various diagnostics tools (temperature, pressure, and species concentrations), to test and improve the understanding of the combustion chemistry of hydrocarbon fuels like propane or n-dodecane which have very large reaction

mechanisms. This experimental approach, combining realistic simulation with multi-parameter diagnostics, will enhance the process of translating experimental kinetics data into highly refined combustion mechanisms for a variety of practical fuel blends such as gasoline, JET A, JP-8, or diesel fuel.

8.6.3 Sensing and control of combustion instabilities in high-pressure spray flames

In this thesis, a feedback instability control system based on the real-time temperature sensor was demonstrated in an atmospheric-pressure combustor. The response time of the current LBO control system is limited to 0.1 s by the actuator. One useful extension of the current work is to investigate different control strategies (e.g., fuel injection, plasma ignition) to improve the control response time.

The control demonstration could be extended to spray flames using liquid hydrocarbon fuels. Normalizing the $2f$ signal by the $1f$ signal can remove the need for calibration and minimize interference from non-resonant losses such as beam steering, droplet scattering, and flame emission. The control work can also be extended to high-pressure flames typical of practical combustors. The current single-laser sensor has a maximum usable pressure of 3.7 atm due to feature overlapping by pressure broadening [Zhou *et al.* 2005a]. Other line pairs (e.g., near 1982 nm) might be able to achieve pressures up to 8 atm for this wavelength-scanned single-laser temperature sensing strategy. For large-scale combustion systems operating at higher pressure, e.g., 20-30 atm, a two-line thermometry scheme using two multiplexed diode lasers can be used instead. Different wavelength modulation parameters could be used to achieve optimum detection of the broadened spectra. The wavelength-multiplexed TDL sensor can be realized with frequency-division multiplexing (as shown in [Rieker *et al.* 2007a]), or wavelength-division multiplexing (as shown by [Mattison 2006]). Alternatively, time-division multiplexing using ultra-fast optical switches (Agiltron website) has recently become commercially available. This architecture could be used to achieve high sensor bandwidth (e.g., MHz for fixed-wavelength WMS). Such sensing technology could enable active control of combustion instabilities in large-scale combustion systems.

APPENDIX A: DIODE LASER-INDUCED INFRARED FLUORESCENCE OF WATER VAPOR

In this appendix, infrared laser-induced fluorescence (LIF) of water vapor is investigated for its potential as a spatially-resolved gasdynamic diagnostic. This work has been published in Measurement Science and Technology [Li *et al.* 2004]. A cw diode laser operating near 1392 nm is scanned across a single absorption transition in the $v_1 + v_3$ band of H_2O in a static cell, and the resulting fluorescence signal is collected near 2.7μm. Experiments are conducted at low pressure in pure water vapor and mixtures of water vapor and N_2 using a DFB diode laser. A simple analytical model is developed to relate LIF intensity to gas properties as a function of laser power. The spectrally-resolved, single-line excitation spectrum is fit with a Voigt profile, allowing inference of the temperature from the Doppler-broadened component of the measured fluorescence lineshape. A two-line excitation scheme is also investigated as a means of measuring temperature with reduced measurement time. From these initial measurements, the power needed for a practical sensor for atmospheric-pressure applications is estimated.

1. Introduction

Pulsed LIF diagnostics using vibrational excitation of CO and CO_2 in the infrared have been demonstrated previously for spatially-resolved gasdynamic measurements [Kirby and Hanson 1999, 2000, 2001]. In the current investigation, we explore the feasibility for continuous (cw) excitation of combination bands of water vapor in the NIR, with observation of mid-IR fluorescence. Near-infrared excitation is attractive owing to the potential for exploiting cw telecommunication laser technology. Semiconductor diode laser technology has become quite robust in the near-IR because of telecom investments,

and fiber-coupled diode lasers are readily available which can access combination bands of H_2O. Although the power is currently limited to about 20 mW, there is potential for a large increase in this quantity, e.g., through use of fiber lasers and fiber amplifiers.

The aim of this research is to investigate the potential of cw diode laser-excited LIF of water vapor as a spatially-resolved gasdynamic diagnostic. For many practical diagnostic applications, the spatial resolution of LIF is advantageous compared to line-of-sight absorption measurements. To our knowledge, this is the first observation of cw LIF of water vapor.

2. Measurement technique

2.1. Combination band excitation LIF

The LIF signal is the result of a three step process: excitation via absorption of laser photons, energy transfer to a fluorescing state, and subsequent emission. The fluorescence signal can be expressed by

$$S_F = (photons\ absorbed) \times (fluorescence\ yield) \times (fraction\ collected) \qquad (A.1)$$
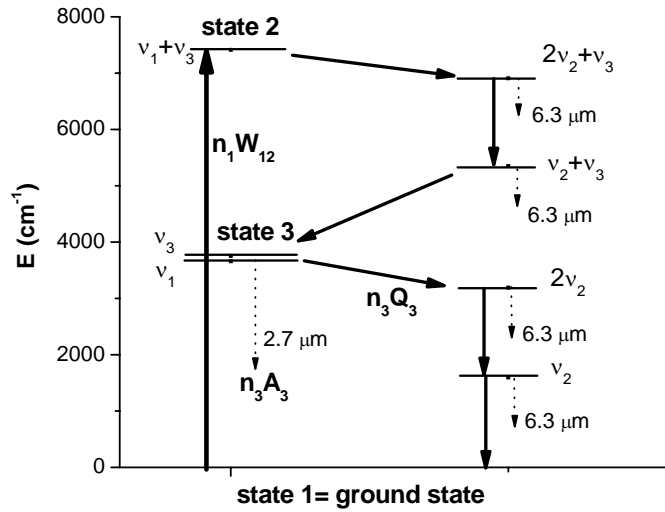
Figure A.1 Vibrational energy levels of H_2O.

Figure A.1 shows the vibrational energy levels [Herzberg 1945] for H_2O. Relaxation rates of the stretching vibrational modes (ν_1, ν_3) and the bending overtone mode ($2\nu_2$) of H_2O have been measured by pulsed LIF [Zittel and Masturzo 1989; Finzi *et al.* 1977]. From that work, it is clear that when single vibration-rotation levels of H_2O (ν_1) or H_2O (ν_3) are excited, the dominant path for self-relaxation is relaxation of the stretching levels (ν_1, ν_3) to the bending overtone level ($2\nu_2$) followed by stepwise vibration to translation (and rotation) relaxation to ν_2 and then the ground state.

In this study, a cw infrared diode laser is used to excite one transition of the $\nu_1 + \nu_3$ combination band. It can be assumed that the primary relaxation pathway is $\nu_1 + \nu_3$ to $2\nu_2 + \nu_3$, to $\nu_2 + \nu_3$, then to $\nu_3 (\nu_1)$, $2\nu_2$, ν_2 and finally the ground state. Since the observed relaxation rates are the same for ν_1 and ν_3, the model treats them together as a single level [Zittel and Masturzo 1989]. Fluorescence signal may be collected around $2.7\,\mu m$ ($\nu_1 = 1 \to 0$ and $\nu_3 = 1 \to 0$), or around $6.3\ \mu m$ ($\nu_2 = 2 \to 1$ and $\nu_2 = 1 \to 0$).

2.2. Estimate of signal

A goal of this work is to develop and experimentally validate an approximate model of LIF signal strength to estimate the laser power needed for a practical cw LIF diagnostic based on water vapor.

A. Absorption

The transmission of a probe beam of monochromatic light through a uniform absorbing medium follows the Beer-Lambert relation, from which the absorbance is defined as

$$\alpha(\nu) = -\ln\left(\frac{I_\nu}{I_\nu^0}\right) = P_{abs} S(T, \nu_0) \phi(\nu) L \tag{A.2}$$

where I_ν^0 is the incident intensity of the probe beam, and I_ν is the intensity observed after propagation through a length L of the absorbing medium. P_{abs} is the partial pressure of the absorbing species (atmospheres), $S(T, \nu_0)$ is the line strength of the transition centered at

ν_0 (cm^{-2}atm^{-1}), and $\phi(\nu)$ is the line-shape function (cm). The lineshape function is often expressed in terms of a Voigt profile. Line positions and the temperature dependent line strength for water vapor transitions can be taken from the HITRAN database [Rothman *et al.* 2005].

B. Fluorescence & collection

In the present study, the laser intensity is sufficiently low that the LIF signal is in the weak excitation limit, i.e., $n_1 \simeq n^0$, where n^0 is the total number density of H$_2$O. Neglecting induced emission and collisional excitation, and assuming full conversion of molecules in state 2 to state 3, the steady-state rate of change of the population of molecules in state 3 is given by

$$\dot{n}_3 = n_1 W_{12} - n_3 (Q_3 + A_3) = 0 \tag{A.3}$$

where W_{12} is the rate (s^{-1}) that individual molecules in state 1 undergo the transition to state 2 due to absorption, Q_3 the quenching rate of state 3, and A_3 the Einstein A coefficient of state 3 (estimated to be 89 s^{-1}, from [Pugh and Rao 1976]) . Thus the population of state 3 is given approximately by

$$(n_3)_{ss} = n^0 \frac{W_{12}}{A_3 + Q_3} . \tag{A.4}$$

The fluorescence signal from state 3 becomes (in collected photons per sec)

$$S_F = n_3 \times V \times A_3 \times \frac{d\Omega}{4\pi} = \underbrace{(n^0 \times V \times W_{12})}_{photons\ absorbed\,/\sec} \times \underbrace{(\frac{A_3}{A_3 + Q_3})}_{fluor\ yield} \underbrace{(\frac{d\Omega}{4\pi})}_{\substack{fraction\\collected}} . \tag{A.5}$$

The number of absorbed photons can be converted to the absorbed energy by

$$(n^0 \times V \times W_{12}) \times h(\nu_1 + \nu_3) = I_{laser} \times (1 - e^{-\alpha}) \approx I_{laser} \times \alpha . \tag{A.6}$$

For pure water vapor, the quenching rate of state 3, $Q_3 = P \times k_3 \gg A_3$, where k_3 is the V-V transfer rate constant of state 3. From [Finzi *et al.* 1977], k_3 is $7.5 \times 10^5 \sec^{-1} \mathrm{torr}^{-1}$ at room temperature.
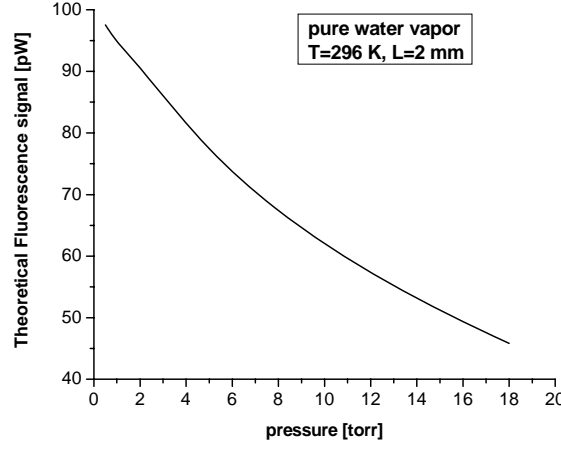
Figure A.2   Estimated peak fluorescence signal as a function of pressure for pure water vapor (diode laser power = 20 mW).

C. Estimated signal

For pure water vapor with P=1.0 torr, L=2 mm, peak (line-center) absorbance can be calculated from equation (A.3) to be 0.005. With a fluorescence yield of $A_3 / Q_3 = 1.2 \times 10^{-4}$, and for a laser power of 20 mW, the fluorescence signal observed from the ν_1 band and ν_3 band (2.6-2.9 μm) would be about 95 pW ($\frac{d\Omega}{4\pi} = 0.016$).

Figure A.2 shows the dependence of fluorescence signal on water vapor pressure when the diode laser wavelength is coincident with the linecenter of the absorption line. The fluorescence signal decreases as the pressure increases. This can be clearly seen by substituting equation (A.6) with equation (A.2) into equation (A.5), for pure water vapor,

$$S_{F,peak} = \frac{I_{laser} A_3}{h(\nu_1 + \nu_3)} \frac{S(T,\nu_0)\phi(\nu_0)L}{k_3} \frac{d\Omega}{4\pi} \tag{A.7}$$

where $\phi(\nu_0)$ decreases due to pressure broadening. For mixtures of H_2O and N_2, equation (A.7) becomes

$$S_{F,peak} = \frac{I_{laser} A_3}{h(\nu_1 + \nu_3)} \frac{P_{H_2O} S(T,\nu_0)\phi(\nu_0)L}{P_{H_2O}k_3 + P_{N_2}k_{H_2O-N_2}} \frac{d\Omega}{4\pi} \tag{A.8}$$

141

where $k_{H_2O-N_2}$ is the deactivation rate of $H_2O(\nu_1, \nu_3)$ by N_2.

If we assume all excited water vapor molecules deactivate through $2\nu_2$ and ν_2, the fluorescence signal collected at 6.3 μm ($\nu_2 = 1 \rightarrow 0$ and $\nu_2 = 2 \rightarrow 1$) is estimated to be 8 pW ($A_{\nu_2=1\rightarrow0} = 20$ sec^{-1}, $k_{\nu_2} = 2 \times 10^6 \, sec^{-1} torr^{-1}$). This is about 1/10 of the estimated signal at $2.7\,\mu m$. In addition, there is more blackbody background near $6.3\,\mu m$ at room temperature, and detectors sensitive to this wavelength typically have lower quantum efficiency. Therefore, fluorescence is collected near 2.7 μm using an InSb detector in this investigation.

3. Experimental setup

Figure A.3 shows the experimental setup consisting of a cw fiber-coupled DFB diode laser (NEL), a static cell, and a data acquisition system. The DFB structure constrains the laser to operate in a single longitudinal mode (single frequency) with a spectral linewidth of 2 MHz. The laser diode provides an output of 19 mW and a wavelength near the linecenter of one strong absorption line of water vapor (1392.53 nm, $J'K'_{-1}K'_1 = 202 \leftarrow J''K''_{-1}K''_1 = 303$, $\nu'_1\nu'_2\nu'_3 = 101 \leftarrow \nu''_1\nu''_2\nu''_3 = 000$), which is near the peak of the rotational distribution.

The water vapor absorption is easily observed on the transmitted intensity, which facilitates tuning the laser wavelength. To measure the small fluorescence signal, the laser beam is modulated by a mechanical chopper (500 Hz). The fluorescence signal is collected by CaF_2 lenses filtered with a band-pass filter (2.57-3.22 μm), detected by an InSb detector (Judson, 2 mm diameter, 30° FOV), and measured with a lock-in amplifier (DSP model 7280) with a full-scale sensitivity of 10 mV and a time constant of 1 s. To increase the fluorescence signal, a double-pass scheme is used to increase the effective laser power (to ~35 mW) and a concave mirror is used to increase the effective collection solid angle (to ~ 0.4 sr).
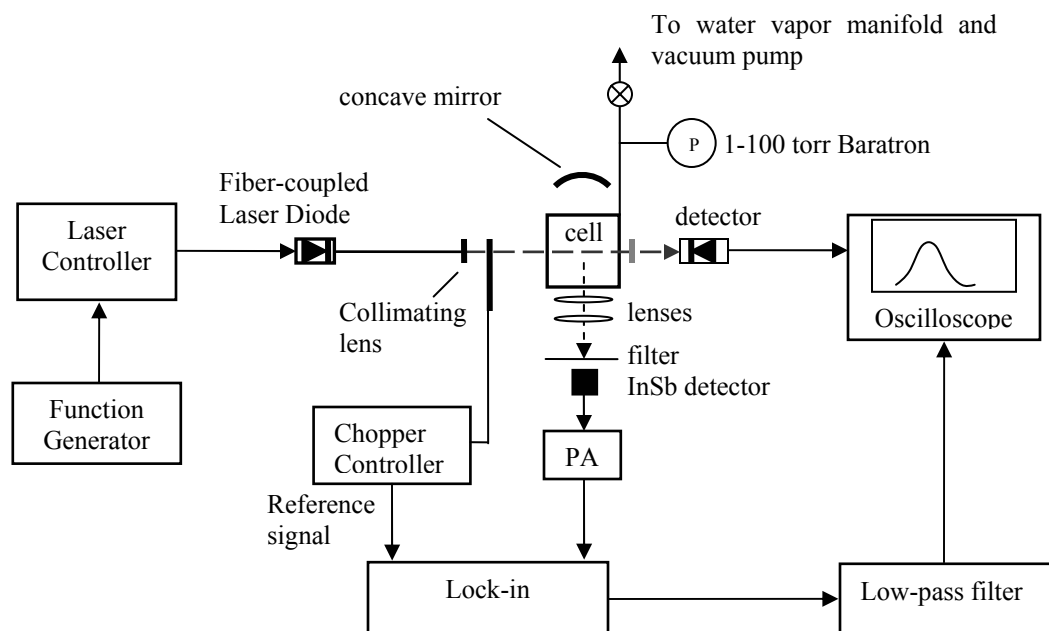
Figure A.3   Experimental setup used to measure fluorescence of water vapor.

4. Results and discussion

The laser wavelength is first tuned to the linecenter of the transition $J^{'}K^{'}_{-1}K^{'}_{1} = 202 \leftarrow J^{''}K^{''}_{-1}K^{''}_{1} = 303$, $v^{'}_{1}v^{'}_{2}v^{'}_{3} = 101 \leftarrow v^{''}_{1}v^{''}_{2}v^{''}_{3} = 000$. For pure water vapor at 1.0 Torr, the measured fluorescence signal with a single-pass arrangement is 12 ± 1 µV (~76 pW), which is very close to the estimated value, 15 µV (95 pW). This agreement provides confidence in the signal estimate from the simple model developed in section 2. The background noise is about 15% of the fluorescence signal with the single-pass arrangement. As expected, the SNR is nearly doubled by use of a double-pass arrangement.
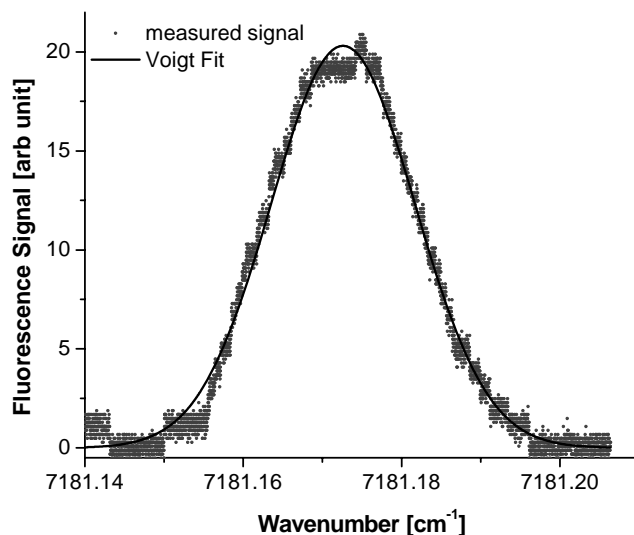
Figure A.4 Single-scan measurement of the fluorescence signal (from the oscilloscope) of pure H_2O at 1.0 torr and room temperature; scanning freq.=0.02 Hz, chopping freq.=500 Hz, lock-in time constant 1 s. The Voigt fit gives a Gaussian FWHM of 0.021 cm^{-1}.

Gasdynamic parameters (temperature, pressure or concentration) may be inferred from the spectrally-resolved excitation spectrum (fluorescence signal as a function of excitation wavelength). The laser wavelength is current tuned and the lock-in signal recorded with the low-pass filter. Figure A.4 shows a single-sweep measurement of the fluorescence signal of pure water vapor at 1.0 Torr and room temperature. The total scan time is 50 s. At this low pressure, Doppler broadening is dominant. A Voigt fit of the measured signal gives a Gaussian FWHM of 0.021 cm^{-1}, which is exactly the same as the theoretical value at room temperature (296 K), confirming that the fluorescence signal follows the absorption lineshape. This suggests that, in practical applications, the temperature of water vapor could be estimated from the FWHM of the lineshape, or from the ratio of the integrated areas using a two-line technique. In atmospheric-pressure applications, the measured collision-broadened lineshape data could also be used to infer pressure.

The fluorescence of H_2O in a mixture of water vapor and N_2 is also examined. The peak fluorescence signals (when the laser diode wavelength is fixed at the linecenter) of

1.0 Torr water vapor with different amounts of N_2 (up to 100 Torr) are recorded. The signal is smaller due to pressure broadening and collisional deactivation by N_2. Figure A.5 shows the linear fit of $\phi(v)/I_F$, where I_F is measured fluorescence signal. From equation (A.8), the ratio of intercept and slope (about 50) corresponds to the ratio of deactivation rate of H_2O (v_1, v_3) by H_2O itself (k_3) and by N_2 ($k_{H_2O-N_2}$). This result ($k_{H_2O-N_2} = 1.4 \times 10^4 \, \text{sec}^{-1}\text{torr}^{-1}$) agrees well with previous measurements ($1.5 \pm 0.4 \times 10^4 \, \text{sec}^{-1}\text{torr}^{-1}$) [Zittel and Masturzo 1989; Finzi *et al.* 1977].
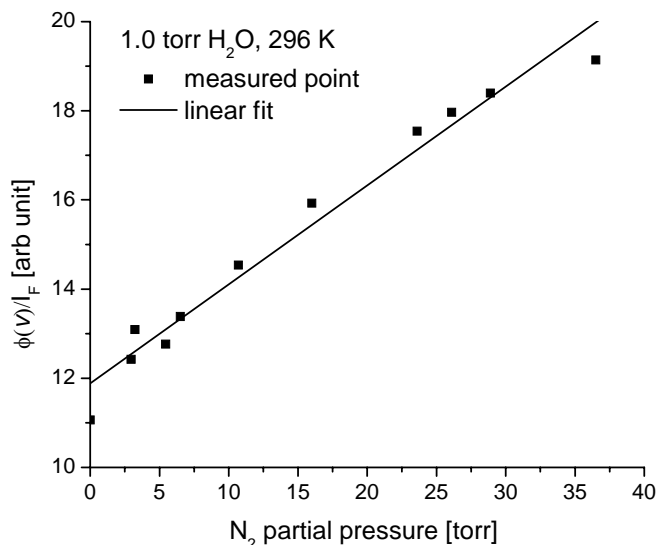
Figure A.5   Fluorescence signal of water vapor in the mixture with N_2.

Figure A.6 shows the peak fluorescence signal of pure water vapor as a function of pressure. As expected from the model, fluorescence signal decreases as pressure increases. Also shown is the estimated value after considering the effects of increased absorption of the excitation laser and the self-absorption of the fluorescence as the water vapor density increases. The estimated value is normalized at P=0.5 Torr to be equal to the measured signal.

145
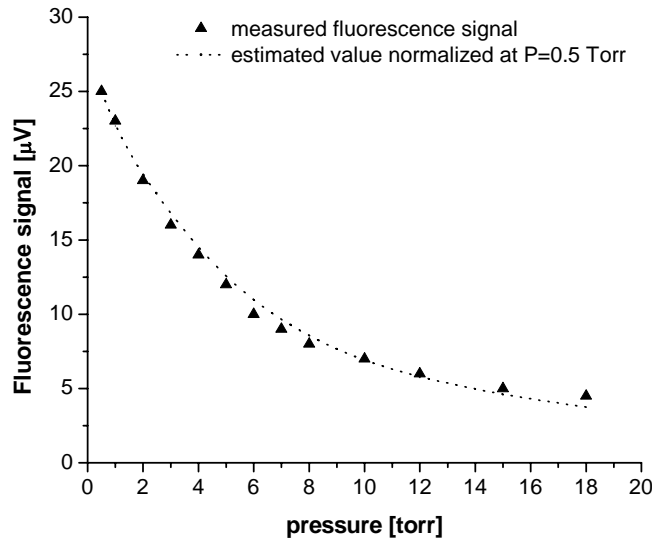
Figure A.6   Pure H_2O fluorescence under different pressures at room temperature (2-pass arrangement) (points). The dashed line shows the predicted pressure dependence normalized to the measured value at 0.5 Torr.

From these initial measurements, the laser power necessary for a practical sensor can be estimated. In room temperature air with 18 Torr H_2O, the fluorescence signal will be smaller than pure H_2O at 18 Torr due to pressure broadening and quenching by air. The fluorescence yield A_3/Q_3 and lineshape function $\phi(v_0)$ of room air will be 52% and 14%, respectively, of those of 18 Torr pure H_2O. From equation (A.8), it can be estimated that the required laser power for the same fluorescence signal as 18 Torr pure H_2O would be about 14 times of the current laser power (20 mW). Another factor of 5 would be necessary to achieve the same SNR as 1 Torr pure H_2O. Finally, yet even more power will be necessary for a practical sensor for a higher scanning frequency. We estimate that 70 watts laser power would be needed for 18 Torr H_2O in 1 atm air to achieve the same SNR as observed in Fig. A.4 for 1 Torr pure H_2O (using 1 s total scan time with a lock-in time constant of 0.02 s).

In typical atmospheric combustion products (e.g., C_3H_8+air, stoichiometric), there are about 15% H_2O and 73% N_2 at equilibrium. The H_2O pressure, fluorescence yield,

linestrength and lineshape function are about 6.3 times, 70%, 10%, 23% those for 18 Torr pure H_2O. From equation (A.8), the needed laser power for the same fluorescence signal as 18 Torr pure H_2O would be 10 times of the current power. A practical sensor (1 s time response, same SNR as 1 Torr H_2O) for atmospheric pressure combustion applications with these gases would require above 50 watts of laser power. In the model built in section 2, we assumed that the laser-induced emission is negligible, i.e., $W_{12} \ll Q_2 + A_2$, where Q_2, A_2 are the quenching rate and Einstein A coefficient of state 2, respectively. The laser power for saturated LIF can be estimated to be greater than 1 MW for a laser beam diameter of 1 mm (by assuming $W_{12}^{sat} = Q_2 + A_2$). Therefore, with 50 watts laser power, water vapor in atmospheric combustion products or room air will remain in the weak excitation limit.

It should also be noted that, in atmospheric applications, H_2O concentration or pressure could also be inferred from the Voigt fit of the fluorescence lineshape. For the higher temperature atmospheric pressure combustion applications at 1500 K, the collisional halfwidth and the Doppler halfwidth are on the same order ($\Delta \nu_C = 0.12 \, \text{cm}^{-1}$, $\Delta \nu_D = 0.05 \, \text{cm}^{-1}$). After determining gas temperature from the Gaussian FWHM, H_2O concentration or pressure could be determined from the Lorentzian FWHM, assuming that the line broadening coefficients for H_2O, CO_2 and air are known at this temperature.

5. Two-line strategy for temperature

Gas temperature can also be inferred from the ratio of the fluorescence signals for two H_2O lines. Two candidate transitions in the $\nu_1 + \nu_3$ band, useful near room temperature, are listed in Table A.1. This line pair provides good temperature sensitivity and accuracy. Experiments conducted with 1.0 Torr water vapor in the static cell, and both diode lasers (20-25 mW) fixed at line center, yield temperature accuracies of 5% for data averaged over 1 s. This fixed-wavelength, two-line excitation scheme substantially reduces the measurement time for temperature relative to the scanned-wavelength, single-line method detailed above. The power needed for a practical sensor (1 s time constant) at

atmospheric pressure would be 1-2 watts for this method, to achieve the same SNR as demonstrated above for 1 Torr pure H_2O in Fig. A.4.

Table A.1 Spectroscopic data for two-line excitation scheme from HITRAN (T=296 K)

Line	wavelength (nm)	Frequency (cm^{-1})	Lower sate energy (cm^{-1})	Line strength (cm^{-1}/atm.cm^{-2})	Laser power (mW)
1	1392.53	7181.172	136.762	1.78E-20	20
2	1385.11	7219.658	447.252	7.08E-21	25

6. Conclusions

Infrared laser induced fluorescence (LIF) of water vapor is investigated for its potential as a gasdynamic diagnostic. A cw DFB fiber-coupled diode laser (19 mW) operating near 1392 nm is used to excite the H_2O in the $\nu_1 + \nu_3$ combination band, and the fluorescence is collected around 2.7 μm ($\nu_1 = 1 \rightarrow 0$ or $\nu_3 = 1 \rightarrow 0$). Experiments are conducted in pure water vapor and mixtures of water vapor and N_2 in a static cell, which validate the simple model developed to estimate the fluorescence signal. The Gaussian FWHM from the Voigt fit of the measured signal match well with the absorption lineshape, illustrating the potential of cw IR LIF of H_2O as a gasdynamic diagnostic for temperature (and pressure).

We estimate that a practical sensor with a 1 s time constant would require a minimum of 70 watts of laser power for scanned-wavelength application and 1-2 watts of laser power for fixed-wavelength applications at atmospheric pressure. Developments in semiconductor diode laser technology may make such powerful diode lasers available in the future. NIR diode laser excitation of H_2O LIF could then be used to provide spatially resolved information of water vapor concentration, temperature and pressure in practical gaseous flows.

APPENDIX B: LONG PATH FLAT FLAME BURNER

A water-cooled, premixed, flat flame burner of rectangular shape (10"×1") was built to serve as a combustion test facility. The uniform temperature distribution along the long pathlength makes the burner extremely useful for validations of laser-based sensors or investigations of absorption features, e.g, see one application in [Liu *et al.* 2007a].

1. Configuration

The long path flat flame (LPFF) burner (10"×1") is an updated generation of an old flat flame burner (4×10 cm) [Mihalcea 1999]. Figure B.1 provides the schematic of the new flat flame burner. The burner housing is made of stainless steel, and is sealed by a Viton O-ring (8" diameter, 3/16" thick) between the top plate and the burner body. One U-shaped channel (1/4" diameter) is drilled in the top plate for the cooling water; plugs are used to seal the ends of the cross-drilled passage at the end (away from the water inlet/exit) of the burner.

The premixed fuel/air mixture is introduced into the lower chamber of the burner through 10 equal-spaced small holes in a ¼" stainless steel tube. The end of the tube is plugged. The holes are faced down to achieve more uniform flow. The mixture passes through a sintered wire mesh (TWP Inc., 0.000079" opening, 0.0223" thickness, stainless steel) and glass balls (1/8" diameter). A stainless steel honeycomb (Kentucky Metals, 1 mm pore size, 0.2 mm wall thickness) is used to create a uniform flow.

There are two additional ports on each end of the burner body for secondary air flow when further manipulation is needed in combustion experiments. Usually, these two ports are plugged. If non-uniform temperature profiles are needed, secondary air flows may be introduced into the upper chamber through these ports.
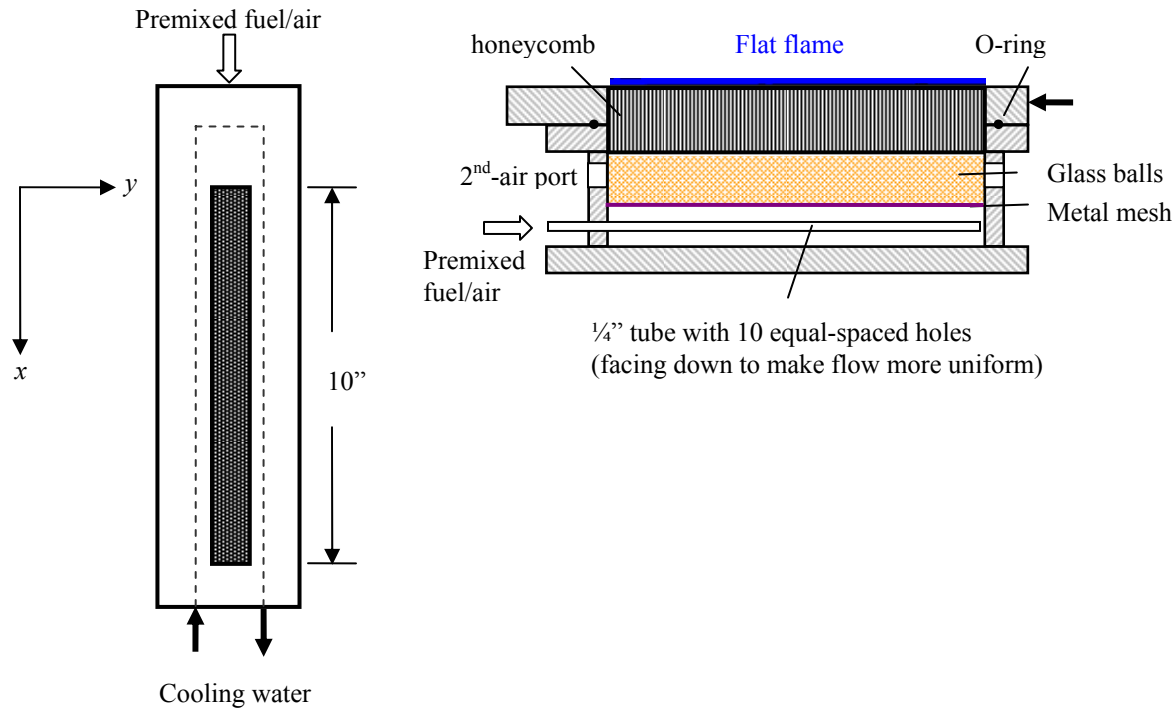
Figure B.1 Schematic of the long path flat flame burner. Left panel: top view; right panel: side view.

2. Burner Characterization

Ethylene and air flows were metered with calibrated rotameters, premixed, and injected into the water-cooled, long path flat flame burner. No secondary air flow was used in the measurements. Stable laminar flames were achieved with operating conditions listed in Tab. B.1. The equivalence ratio ranged from 0.58 to 1.42.

A comparison of corrected thermocouple temperature measurements and calculated adiabatic flame temperature is illustrated in Fig. B.2. The temperature measurements were performed at a 3 mm height from the burner surface in the center of the flame with a type-S thermocouple (2 mil wire). The calculated radiation corrections for the thermocouple measurements were about 50 K. The measured temperatures were much lower than adiabatic flame temperature (simulated using STANJAN) due to heat transfer to the burner and radiation loss. Flame temperatures from thermocouple measurements ranged from 1450 K to 1600 K.

Table B.1   Tested C_2H_4/air flow rates in the LPFF burner. SLM: standard liters per minute.

No.	Fuel flow rate [SLM]	Air flow rate [SLM]	Equivalence ratio
1	1.35		0.58
2	1.49		0.64
3	1.62	33.21	0.70
4	1.76		0.76
5	1.92		0.82
6	2.04		0.88
7		31.23	0.88
8		28.94	0.95
9	1.92	26.51	1.03
10		23.97	1.14
11		21.78	1.26
12		19.27	1.42
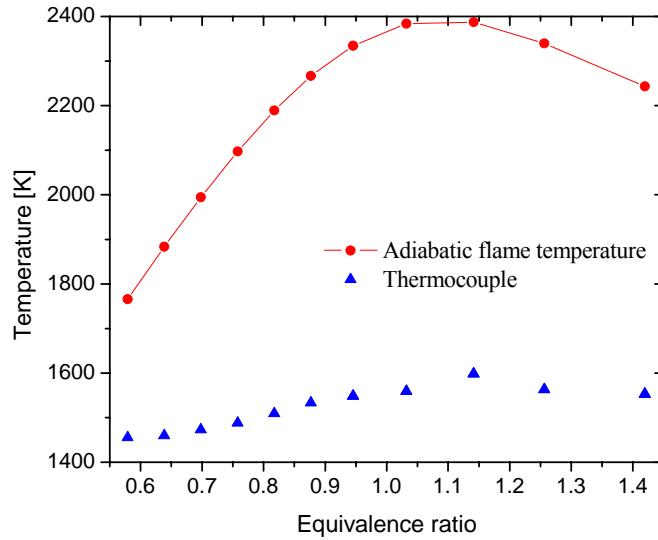
Figure B.2   Measured thermocouple temperature (corrected) in the C_2H_4-air flame as function of equivalence ratio (measurement location 3 mm above burner, center of the burner). Adiabatic flame temperature (simulated using STANJAN) is given as well.

The temperature profile was measured along the long dimension (*x* direction in Fig. B.1) of the burner on the center-line and at a 3 mm height to determine the flame non-uniformity (Fig. B.3). The temperature profile shows a flat central core of ~ 9" length with a center temperature of 1525 K. The temperature increases by approximately 70 K towards the flame boundaries before it drops off rapidly in regions where cooling and mixing occurs. This is also due to a combined heat transfer effect of conduction and radiation. The honeycomb has relatively low conductivity owing to its structure. The center portion of honeycomb surface has higher temperature and thus more radiation loss, than the edge. The dominant heat loss is radiation for the center portion instead of conduction for the edge. From energy balance, the product gas temperature will be lower in the center portion.

The temperature profile along the short dimension (*y* direction in Fig. B.1) of the burner at a 3 mm height was also measured (Fig. B.4). The temperature profile shows similar distribution as Fig. B.3.

premixed
C_2H_4: 1.92 SLM
air: 33.21 SLM
Equivlance ratio=0.82
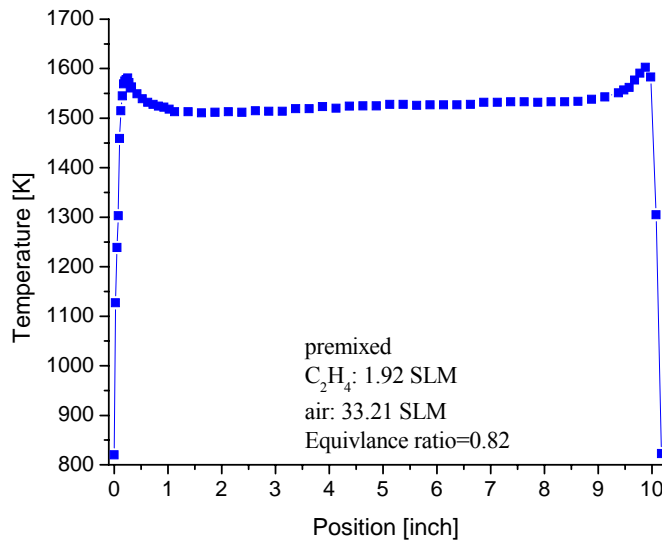
Figure B.3   Measured temperature profile (using type-S thermocouple, 2 mil wire) along *x* direction (long dimension) in the premixed C_2H_4-air flame, 3 mm height above burner, center-line.
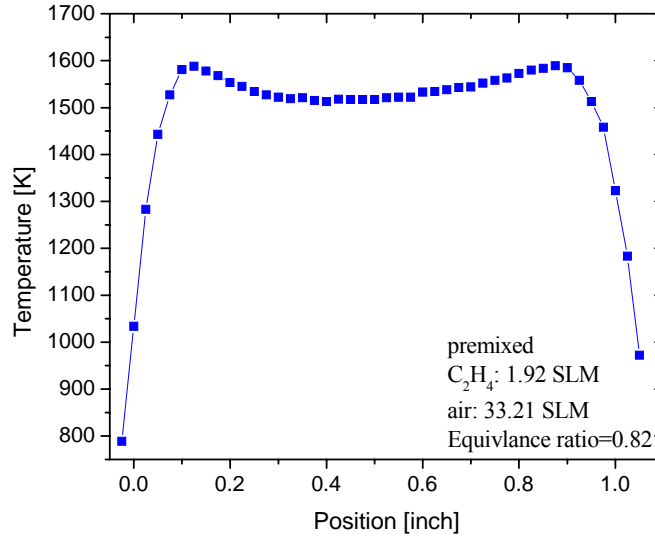
Figure B.4 Measured temperature profile (using type-S thermocouple, 2 mil wire) along *y* direction (short dimension) in the premixed C_2H_4-air flame, 3 mm height above burner, center-line.

Two pictures of the flame at the operating condition of Fig. B.4 (1.92 SLM C_2H_4 and 33.21 SLM air) are shown in Fig. B5. The flat flame is stable and uniformly distributed. From the end view, it is clearly seen that the flame is not lifted at the edge. With uniformly-distributed temperature along the long pathlength, the LPFF burner can be used for diode laser sensor validations. In addition to ethylene, the burner may be operated with other fuels such as CH_4 or C_3H_8.
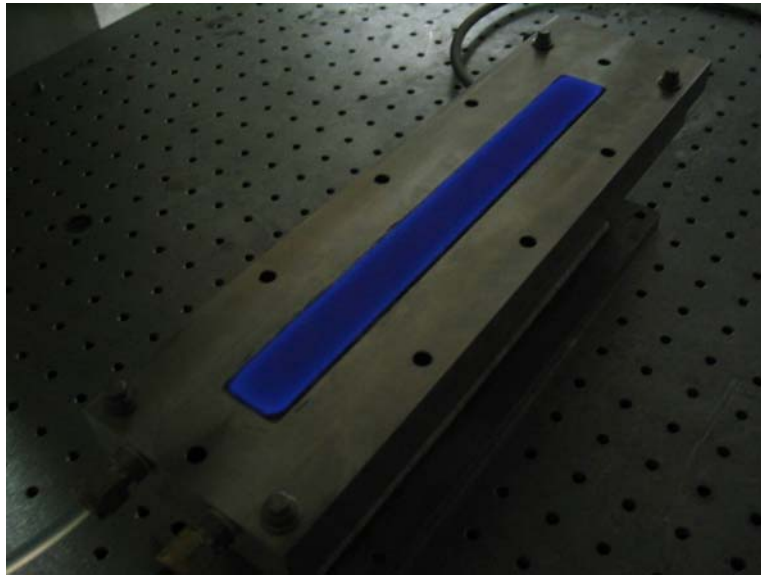
(a) top view
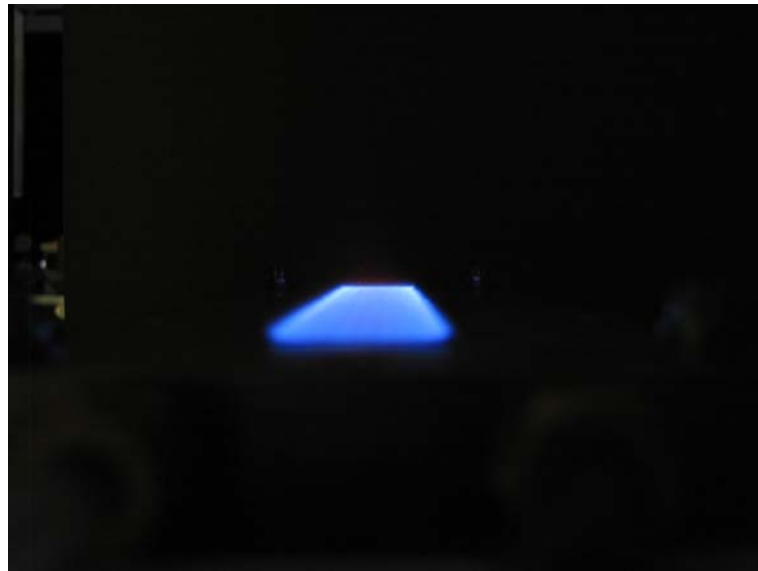
(b) end view

Figure B.5 Long path flat flame burner with premixed C_2H_4-air flame: 1.92 SLM C_2H_4 and 33.21 SLM air.

APPENDIX C: HARDWARE AND SOFTWARE INVOLVED IN THE COMBUSTION CONTROL SYSTEM

This appendix summarizes the hardware and software involved in the real-time combustion control system presented in Chapter 7. All software programs presented here are archived in the Hanson research group at Stanford University [Hanson group website].

The architecture of the single-laser, real-time temperature sensor based on WMS-2f technique has been detailed in X. Zhou's Ph.D. thesis [Zhou 2005c]. Two-kHz real-time data processing, including peak finding and WMS-2f ratio calculation, is achieved by a fast PC combined with a laboratory code written in C/C++ (see [Zhou 2005c] for detail). The fast PC is equipped with:

1) a Gage CompuScope 1250 card for data acquisition (to acquire the second-harmonic component of the detector signal measured by a Perkin-Elmer lock-in amplifier);

2) a National Instruments PCI 6115 board for real-time 2f ratio output at 2 kHz.

This thesis utilized the real-time temperature sensor for thermoacoustic detection and lean blowout control in a swirl-stabilized combustor (see Fig. C.1 for the experimental setup). Another computer equipped with NI-DAQ board is used to log the WMS-2f peak ratio from the sensor computer, and calculate a running power spectrum using a fast FFT algorithm using a LabVIEW program. For thermoacoustic detection, the dominant oscillation frequency can be identified from the power spectrum (e.g., see Fig. 7.7). In LBO control experiments, the LabVIEW program also controls fuel flow rate by changing the voltage applied on the control valve. Figure C.2 illustrates the LBO control

diagram corresponding to the control experiment shown in Fig 7.17. In the LabVIEW program, control parameters, such as the threshold (r) and gain (g), can be set by the user to optimize the performance of the feedback control system.
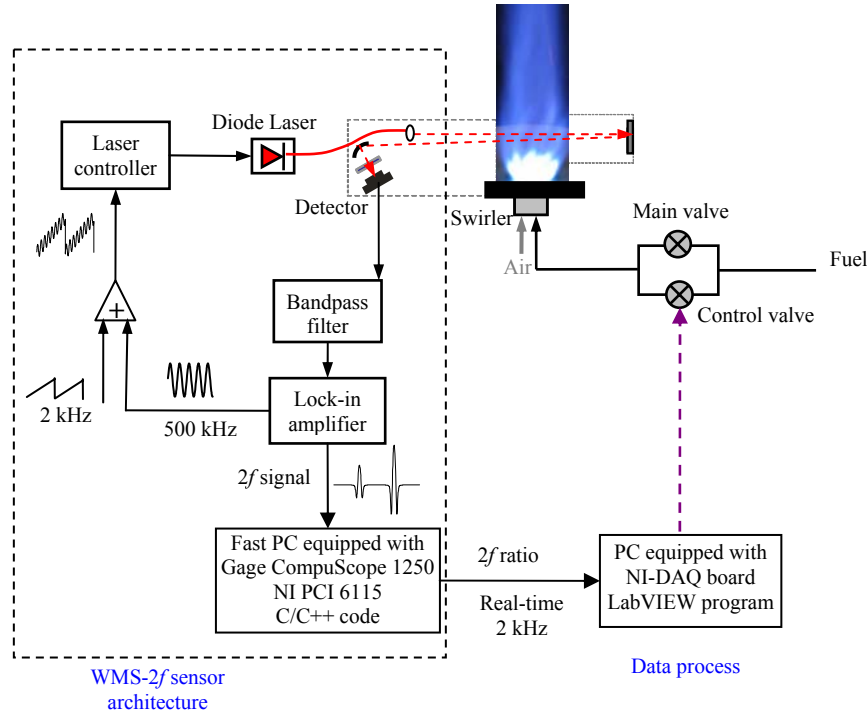
Fig. C.1 Schematic diagram of the lean blowout control experiment.
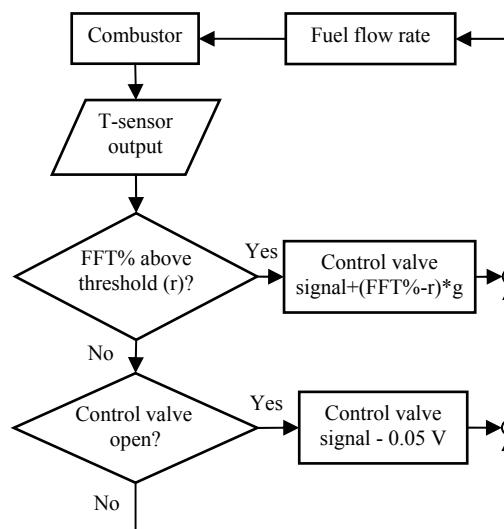
Fig. C.2 LBO control algorithm.

REFERENCES

Agiltron website: http://www.agiltron.com/

T. Aizawa, "Diode-laser wavelength-modulation absorption spectroscopy for quantitative in situ measurements of temperature and OH radical concentration in combustion gases," Appl. Opt., 40, 4894-4903, 2001.

M.G. Allen, "Diode laser absorption sensors for gas-dynamic and combustion flows," Meas. Sci. Technol. 9, 545-562, 1998.

M.G. Allen, E.R. Furlong, and R.K. Hanson, "Tunable diode laser sensing and combustion control," in Applied Combustion Diagnostics, K. Kohse-Hoeinghaus and J.B. Jeffries, eds., Taylor and Francis, Washington, D.C., 479-498, 2002.

R. Arndt, "Analytical line shapes for Lorentzian signals broadened by modulation," J. Appl. Phys. 36, 2522-2524, 1965.

M.P. Arroyo, and R.K. Hanson, "Absorption measurements of water-vapor concentration, temperature, and line-shape parameters using a tunable InGaAsP diode laser," Appl. Opt. 32, 6104-6116, 1993.

A. Ateshkadi, V.G. McDonell, and G.S. Samuelsen, "Lean blowout model for a spray-fired swirl-stabilized combustor," Proc. Combust. Inst. 28, 1281-1288, 2000.

D.S. Baer, V. Nagali, E.R. Furlong, and R.K. Hanson, "Scanned- and fixed-wavelength absorption diagnostics for combustion measurements using multiplexed diode lasers," AIAA J. 34, 489-493, 1996.

R.W. Bates, D.M. Golden, R.K. Hanson, C.T. Bowman, "Experimental study and modeling of the reaction $H+O_2+M \rightarrow HO_2+M$ (M=Ar, N_2, H_2O) at elevated pressures and temperatures between 1050 and 1250 K," Phys. Chem. Chem. Phys. 3, 2337-2342, 2001.

D.L. Baulch, C.T. Bowman, C.J. Cobos, R.A. Cox, Th. Just, J.A. Kerr, M.J. Pilling, D. Stocker, J. Troe, W. Tsang, R.W. Walker, J. Warnatz, "Evaluated kinetic data for combustion modeling: supplement II," J. Phys. Chem. Ref. Data 34, 757-1397, 2005.

D.S. Bomse, A.S. Stanton, and J.A. Silver, "Frequency modulation and wavelength modulation spectroscopies: comparison of experimental methods using a lead-salt diode laser," Appl. Opt. 31, 718-731, 1992.

C.T. Bowman, R.K. Hanson, "Shock tube measurements of rate coefficients of elementary gas reactions," J. Phys. Chem. 83, 757-763, 1979.

D. Bradley, P.H. Gaskell, X.J. Gu, M. Lawes, and M.J. Scott, "Premixed turbulent flame instability and NO formation in a lean-burn swirl burner," Combust. Flame 115, 515-538, 1998.

References

P.N. Brown, G.D. Byrne, A.C. Hindmarsh, "VODE: a variable coefficient ODE solver," SIAM J. Sci. Stat. Comput. 10(5), 1038-1051, 1989.

D.T. Cassidy and J. Reid, "Atmospheric pressure monitoring of trace gases using tunable diode lasers," Appl. Opt. 21, 1185-1190, 1982.

D.T. Cassidy and L.J. Bonnell, "Trace gas detection with short-external-cavity InGaAsP diode laser transmitter modules operating at 1.58 μm," Appl. Opt. 27, 2688-2693, 1988.

Y.C. Chao, Y.L. Chang, C.Y. Wu, and T.S. Cheng, "An experimental investigation of the blowout process of a jet flame," Proc. Combust. Inst. 28, 335-342, 2000.

S.I. Chou, D.S. Baer, and R.K. Hanson, "Diode-laser measurements of He-, Ar- and N_2-broadened HF lineshapes in the first overtone band," J. Mol. Spectrosc. 196, 70-76, 1999.

S.I. Chou, "Diode-laser absorption spectroscopy of hydrogen halides for semiconductor plasma process diagnostics," Ph.D. dissertation, Dept. Mechanical Engineering, Stanford Univ., Stanford, CA, 2000.

C. Claveau, A. Henry, D. Hurtmans, A. Valentin, "Narrowing and broadening parameters of H2O lines perturbed by He, Ne, Ar, Kr and nitrogen in the spectral range 1850-2140 cm^{-1}," J. Quant. Spectrosc. Radiat. Transfer. 68, 273-98, 2001

S.A. Clough, F.X. Kneizys, R.W. Davies, "Line shape and the water vapor continuum," Atmospheric Research, 23, 229-241, 1989.

M.O. Conaire, H.J. Curran, J.M. Simmie, W.J. Pitz, C.K. Westbrook, "A comprehensive modeling study of hydrogen oxidation," Int. J. Chem. Kinet. 36, 603-622, 2004.

H.J. Curran, P. Gaffuri, W.J. Pitz, C.K. Westbrook, "A comprehensive modeling study of n-heptane oxidation," Combust. Flame 114, 149-177 , 1998.

D.F. Davidson and R.K. Hanson, "Interpreting shock tube ignition data," Int. J. Chem. Kinet. 36, 510-523, 2004.

S.G. Davis, A.V. Joshi, H. Wang, F. Egolfopoulos, "An optimized kinetic model of H_2/CO combustion," Proc. Combust. Inst. 30, 1283-1292, 2005.

R.H. Dicke, "The effect of collisions upon the Doppler width of spectra lines," Phys. Rev. 89, 472-473, 1953.

A.P. Dowling and A.S. Morgans, "Feedback control of combustion oscillations," Annu. Rev. Fluid Mech. 37, 151-182, 2005.

X.R. Duan, W. Meier, P. Weigand, and B. Lehmann, "Phase-resolved laser Raman scattering and laser Doppler velocimetry applied to periodic instabilities in a gas turbine model combustor," Appl. Phys. B 80, 389-396, 2005.

M.D. Durbin and D.R. Ballal, "Studies of lean blowout in a step swirl combustor," J. Eng. Gas Turb. Power 118, 72-77, 1996.

P. Duggan, P.M. Sinclair, A.D. May, and J.R. Drummond, "Line-shape analysis of speed-dependent collisional width inhomogeneities in CO broadened by Xe, N_2 and He," Phys. Rev. A 51, 218-224, 1995.

A.C. Eckbreth, Laser diagnostics for combustion temperature and species, 2nd edition, Gordon and Breach Publishers, Amsterdam, 1996.

R.S. Eng, A.R. Calawa, T.C. Harman, P.L. Kelley, A. Javan, "Collisional narrowing of infrared water-vapor transitions," Appl. Phys. Lett . 21, 303-5, 1972.

A. Farooq, H. Li, J.B. Jeffries, R.K. Hanson, "Measurements of CO_2 and H_2O near 2.7 μm using tunable diode-laser absorption," 43rd AIAA/ASME/SAE/ASEE Joint Propulsion Conference, AIAA-2007-5015, Cincinnati, OH, 2007.

R.P. Fedkiw, B. Merriman, S. Osher, "High accuracy numerical methods for thermally perfect gas flows with chemistry," J. Comput. Phys. 132, 175-190, 1997.

T. Fernholz, H. Teichert, and V. Ebert, "Digital, phase-sensitive detection for in situ diode-laser spectroscopy under rapidly changing transmission conditions," Appl. Phys. B 75, 229-236, 2002.

J. Finzi, F.E. Hovis, V.H. Panfilov, P. Hess, and C.B. Moore, "Vibrational relaxation of water vapor," J. Chem. Phys. 67, 4053-4061, 1977.

E.R. Furlong, D.S. Baer, and R.K. Hanson, "Combustion control and monitoring using a multiplexed diode-laser sensor system," Proc. Comb. Inst. 26, 2851-2858, 1996.

E.R. Furlong, D.S. Baer, and R.K. Hanson, "Real-time adaptive combustion control using diode-laser absorption sensors," Proc. Comb. Inst. 27, 103-111, 1998.

L. Galatry, "Simultaneous effect of Doppler and foreign gas broadening on spectral lines," Phys. Rev. 122, 1218-1223, 1961.

R.R. Gamache, S. Kennedy, R. Hawkins, and L.S. Rothman, "Total internal partition sums for molecules in the terrestrial atmosphere," J. Mol. Struct. 517-518, 407-425, 2000.

M. Gharavi, S.G. Buckley, "A Multiplexed diode laser sensor based on wavelength modulation spectroscopy for simultaneous measurement of temperature and concentration of H_2O and CH_4," presented at Fourth Joint Meeting of the US Section of the Combustion Institute, Philadelphia, Pennsylvania, 20-23 March 2005.

I. Glassman, Combustion, Academic Press, San Diego, CA 1996.

GRI-Mech 3.0, http://www.me.berkeley.edu/gri-mech/, 1999

E.J. Gutmark, T.P. Parr, K.J. Wilson, D.M. Hanson-Parr, and K.C. Schadow, "Closed-loop control in a flame and a dump combustor," IEEE Control Systems 13(2), 74-78, 1993.

B.E. Grossmann, E.V. Browell, "Water-vapor line broadening and shifting by air, nitrogen, oxygen, and argon in the 720-nm wavelength region," J. Mol. Spectrosc.138, 562-95, 1989.

Hanson Group Website: http://hanson.stanford.edu/.

R.K. Hanson, D.F. Davidson. In Handbook of Shock Waves, G. Ben-Dor, O. Igra, T. Elperin, (Eds.), Vol.1, Ch 5.2, Academic Press, San Diego, CA, 2001.

R.K. Hanson and P.K. Falcone, "Temperature measurement technique for high-temperature gases using a tunable diode laser," Appl. Opt. 17, 2477-2840, 1978.

A. Henry, C. Claveau, A. Valentin, D. Hurtmans, A.W. Mantz, "Confinement narrowing of the R(0) line in the ^{13}CO fundamental band broadened by helium from room temperature down to 40 K," J. Mol. Spectrosc. 214, 28-34, 2002.

References

H. Herbert, "Spectral line profile: a generalized Voigt function including collisional narrowing," J. Quant. Spectrosc. Radiat. Transfer.14, 943-51, 1974.

J.T. Herbon, R.K. Hanson, D.M. Golden, C.T. Bowman, "A shock tube study of the enthalpy of formation of OH ," Proc. Combust. Inst. 29, 1201-1208, 2002.

G. Herzberg, Molecular spectra and molecular structure II: Infrared and Raman spectra of polyatomic molecules, Van Nostrand Reinhold, NY, 1945, Reprinted Krieger Malabar Publishing, FL, 1991.

J.O. Hirschfelder, Molecular Theory of Gases and Liquids, New York, Wiley, 1954.

D.C. Hovde, J.T. Hodges, G.E. Scace, and J.A. Silver, "Wavelength-modulation laser hygrometer for ultrasensitive detection of water vapor in semiconductor gases," Appl. Opt., 40, 829-839, 2001.

P. Kauranen, H.M. Hertz and S. Svanberg, "Tomographic imaging of fluid flows by the use of two-tone frequency-modulation spectroscopy," Opt. Lett. 19, 1489-1491, 1994.

R.J. Kee, F.M. Rupley, J.A. Miller, "Chemkin-II: A Fortran chemical kinetics Package for the analysis of gas phase chemical kinetics," Sandia National Laboratories, Tech. Rept. SAND89-8009, 1989.

B.J. Kirby and R.K. Hanson, "Planar laser-induced fluorescence imaging of carbon monoxide using vibrational (infrared) transitions," Appl. Phys. B 69, 505-507, 1999.

B.J. Kirby and R.K. Hanson, "Imaging of CO and CO2 using infrared planar laser induced fluorescence," Proc. Combust. Inst. 28, 253-259, 2000.

B.J. Kirby and R.K. Hanson, "CO2 imaging with saturated planar laser-induced vibrational fluorescence," Appl. Opt. 40, 6136-6144, 2001.

P. Kluczynski and O. Axner, "Theoretical description based on Fourier analysis of wavelength-modulation spectrometry in terms of analytical and background signals," Appl. Opt. 38, 5803-5815, 1999.

P Kluczynski, A Lindberg, and O. Axner, "Background signals in wavelength-modulation spectrometry with frequency–doubled diode-laser light. I. Theory," Appl. Opt. 40, 783-793, 2001a.

P Kluczynski, A Lindberg, and O. Axner, "Background signals in wavelength-modulation spectrometry with frequency–doubled diode-laser light. II. Experiment," Appl. Opt. 40, 794-804, 2001b.

K. Kohse-Höinghaus, R.S. Barlow, M. Aldén and J. Wolfrum, "Combustion at the focus: laser diagnostics and control," Proc. Comb. Inst. 30, 89-124, 2005.

T. Iseki, H. Tai, and K. Kimura, "A portable remote methane sensor using a tunable diode laser," Meas. Sci. Technol. 11, 594-602, 2000.

S. Langlois, T.P. Birbeck, R.K. Hanson, "Diode laser measurements of H_2O line intensities and self-broadening coefficients in the 1.4-μm region," J. Mol. Spectrosc. 163, 27-42, 1994a.

J.G. Lee and D.A. Santavicca, "Experimental diagnostics for the study of combustion instabilities in lean premixed combustors," J. Prop. Power 19(5), 735-750, 2003.

M. Lepere, A. Henry, A. Valentin, C. Camy-Peyret, "Diode-laser spectroscopy: line profiles of H_2O in the region of 1.39 μm," J. Mol. Spectrosc. 208, 25-31, 2001.

A.H. Lefebvre, Gas Turbine Combustion, Edwards Brothers, Ann Arbor, MI, 1999.

G. Li, and E.J. Gutmark, "Experimental study of flow patterns and reaction in a multiple swirl spray combustor," 41st AIAA Aerospace Sciences Meeting and Exhibit, AIAA 2003-489, Reno, NV, Jan. 6-9, 2003.

H. Li, R.K. Hanson, and J.B. Jeffries, "Diode laser-induced infrared fluorescence of water vapor," Meas. Sci. Technol. 15(7), 1285-1290, 2004.

H. Li, G.B. Rieker, X. Liu, J.B. Jeffries, and R.K. Hanson, "Extension of wavelength modulation spectroscopy to large modulation depth for diode laser absorption measurements in high pressure gases," Appl. Opt. 45, 1052-1061, 2006.

H. Li, X. Zhou, J.B. Jeffries, and R.K. Hanson, "Active control of lean blowout in a swirl-stabilized combustor using a tunable diode laser," Proc. Comb. Inst. 31, 3215-3223, 2007a.

H. Li, X. Zhou, J.B. Jeffries, and R.K. Hanson, "Sensing and control of combustion instabilities in swirl-stabilized combustors using diode-laser absorption," AIAA J. 45, 390-398, 2007b.

H. Li, A. Farooq, J.B. Jeffries, and R.K. Hanson, "Diode laser measurements of temperature-dependent collisional narrowing and broadening parameters of Ar-perturbed H_2O transitions at 1391.7 and 1397.8 nm," J. Quant. Spectrosc. Radiat. Transfer, in press, 2007c.

H. Li, A. Farooq, J.B. Jeffries, and R.K. Hanson, "Near-infrared diode laser absorption sensor for rapid measurements of temperature and water vapor in a shock tube," Appl. Phys. B, in press, 2007d.

T. Lieuwen, H. Torres, C. Johnson, and B.T. Zinn, "A mechanism of combustion instability in lean premixed gas turbine combustors," J. Eng Gas Turb. Power 123, 182-189, 2001.

J.T.C. Liu, J.B. Jeffries and R.K. Hanson, "Wavelength modulation absorption spectroscopy with 2f detection using multiplexed diode lasers for rapid temperature measurements in gaseous flows," Appl. Phys. B 78, 503-511, 2004a.

J.T.C. Liu, J.B. Jeffries and R.K. Hanson, "Large-modulation-depth 2f spectroscopy with diode lasers for rapid temperature and species measurements in gases with blended and broadened spectra," Appl. Opt. 43, 6500-6509, 2004b.

J.T.C. Liu, "Near-infrared diode laser absorption diagnostics for temperature and species in engines," Ph.D. dissertation, Dept. Mechanical Engineering, Stanford Univ., Stanford, CA, 2004c.

J.T.C. Liu, G.B. Rieker, J.B. Jeffries and R.K. Hanson, "Near-infrared diode laser absorption diagnostic for temperature and water vapor in a scramjet combustor," Appl. Opt. 44, 6701-6711, 2005.

X. Liu, J.B. Jeffries, R.K. Hanson and et. al., "Development of a tunable diode laser sensor for measurements of gas turbine exhaust temperature," Appl. Phys. B 82, 469-478, 2006.

X. Liu, J.B. Jeffries, and R.K. Hanson, "Measurement of non-Uniform temperature distributions using line-of-sight absorption spectroscopy," AIAA J. 45(2), 411-419, 2007a.

References

X. Liu, J.B. Jeffries, and R.K. Hanson, "Measurements of spectral parameters of water-vapor transitions near 1388 and 1345 nm for accurate simulation of high-pressure absorption spectra," Meas. Sci. Technol.18,1185-1194, 2007b.

X. Liu, X. Zhou, J.B. Jeffries, and R.K. Hanson, "Experimental study of H_2O spectroscopic parameters in the near-IR (6940-7440 cm^{-1}) for gas sensing applications at elevated temperature," J. Quant. Spectrosc. Radiat. Transfer 103, 565-577, 2007c.

K. Lyle, "Development of a real-time diode-laser mass flux sensor for simultaneous measurement of density and velocity of Oxygen," Ph.D. dissertation, Dept. Mechanical Engineering, Stanford Univ., Stanford, CA, 2005.

R.J. Martin and N.J. Brown, "Nitrous oxide formation and destruction in lean, premixed combustion," Combust. Flame 80, 238-255, 1990.

D. Mattison, "Development and application of laser-based sensors for harsh combustion environments," Ph.D. dissertation, Dept. Mechanical Engineering, Stanford Univ., Stanford, CA, 2006.

J.V. Michael, M.-C. Su, J.W. Sutherland, J.J. Carroll, A.F. Wagner, "Rate constants for $H+O_2+M \rightarrow HO_2+M$ in seven bath gases," J. Phys. Chem. A 106, 5297-5313, 2002.

R.M. Mihalcea, "CO and CO_2 measurements in combustion environments using external cavity diode lasers", Ph.D. dissertation, Dept. Mechanical Engineering, Stanford Univ. Stanford, CA, 1999.

J.A. Miller, C.T. Bowman, "Mechanism and modeling of nitrogen chemistry in combustion," Progress in Energy and Combust Science 15, 287-338, 1989.

V. Nagali, S.I. Chou, D.S. Baer, R.K. Hanson, "Diode-laser measurements of temperature-dependent half-widths of H_2O transitions in the 1.4μm region," J. Quant. Spectrosc. Radiat. Transfer. 57, 795-809, 1997.

V. Nagali, "Diode laser study of high-pressure water vapor spectroscopy," Ph.D. dissertation, Dept. Mechanical Engineering, Stanford Univ., Stanford, CA, 1998.

S. Nair, R. Rajaram, A.J. Meyers, and T.C. Lieuwen, "Acoustic and ion sensing of lean blowout in an aircraft combustor simulator," 43rd AIAA Aerospace Sciences Meeting and Exhibit, AIAA 2005-932, Reno, NV, Jan. 10-13, 2005.

NEL website: http://www.nel-world.com/products/photonics/semicon_ld.html.

Y. Neumeier and B.T. Zinn, "Experimental demonstration of active control of combustion instabilities using real-time modes observation and secondary fuel injection," Proc. Comb. Inst. 26, 2811-2818, 1996.

X. Ouyang, and P.L. Varghese, "Line-of-sight absorption measurements of high temperature gases with thermal and concentration boundary layers," Appl. Opt. 28, 3979-3984, 1989.

Z.C. Owens, R.K. Hanson, "Sigle-cycle unsteady nozzle phenomena in pulse detonation engines," J. Prop. Power 23, 325-337, 2007.

C.O. Paschereit, E. Gutmark, and W. Weisenstein, "Control of thermoacoustic instabilities and emissions in an industrial-type gas-turbine combustion," Proc. Comb. Inst. 27, 1817-1824, 1998.

E.L. Petersen, R.K. Hanson, "Nonideal effects behind reflected shock waves in a high-pressure shock tube," Shock Waves 10, 405-420, 2002.

R. Phelan, M. Lynch, J.F. Donegan and V. Weldon, "Absorption line shift with temperature and pressure: impact on laser-diode based H_2O sensing at 1.393 μm," Appl. Opt. 42, 4968-4974, 2003.

L.C. Philippe and R.K. Hanson, "Laser diode wavelength modulation spectroscopy for simultaneous measurement of temperature, pressure, and velocity in shock-heated oxygen flows," Appl. Opt. 32, 6090-6103, 1993.

A.S. Pine, "Collisional narrowing of HF fundamental band spectral lines by Neon and Argon," J. Mol. Spectrosc. 82, 435, 1980.

A.S. Pine, R. Ciurylo, "Multispectrum fits of Ar-broadened HF with a generalized asymmetric lineshape: effects of correlation, hardness, speed dependence, and collision duration," J. Mol. Spectrosc. 208, 180-87, 2001.

L. A. Pugh and K.N. Rao, Molecular Spectroscopy: Modern Research, Academic Press, New York, 65-90, 1976.

S.G. Rautian, and I.I. Sobel'man, "The effect of collisions on the Doppler broadening of spectral lines. Sov. Phys. Usp. 9, 701-716, 1967.

J.W.S. Rayleigh, The Theory of Sound 2, Dover, New York, 1945.

Reaction Design website: http://www.reactiondesign.com/products/open/news_chemkin.html.

J. Reid and D. Labrie, "Second-harmonic detection with tunable diode lasers - comparison of experiment and theory," Appl. Phys. B 26, 203-210, 1981.

D. Richter, D.G. Lancaster, and F.K. Tittel, "Development of an automated diode-laser-based multicomponent gas sensor," Appl. Opt. 39, 4444-4450, 2000.

G.B. Rieker, H. Li, X. Liu, J.T.C Liu, J.B. Jeffries, R.K. Hanson, M.G. Allen, S.D. Wehe, *et al.*,, "Rapid measurements of temperature and H_2O concentration in IC engines with a spark plug-mounted diode laser sensor," Proc. Combust. Inst. 31, 3041-3049, 2007a.

G.B. Rieker, H. Li, X. Liu, J.B. Jeffries, R.K. Hanson, M.G. Allen, S.D. Wehe, P.A. Mulhall, and H.S. Kindle, "A Diode Laser Sensor for Rapid, Sensitive Measurements of Gas Temperature and Water Vapor Concentration at High Temperatures and Pressures," Meas. Sci. Technol. 18, 1195-1204, 2007b.

G.B. Rieker, X. Liu, H. Li, J.B. Jeffries, and R.K. Hanson, "Measurements of near-IR water vapor absorption at high pressure and temperature," Appl. Phys. B 87, 169-178 2007c.

L.S. Rothman, A. Barbe, D.C. Benner, et. al., "The HITRAN molecular spectroscopic database: edition of 2000 including updates through 2001," J. Quant. Spectrosc. Radiat. Transfer. 82, 5-44, 2003.

L.S. Rothman, D. Jacquemart, A. Barbe, et. al., "The HITRAN 2004 molecular spectroscopic database," J. Quant. Spectrosc. Radiat. Transfer. 96, 139-204, 2005. http://cfa-www.harvard.edu/hitran/.

References

S.T. Sanders, J.A. Baldwin, T.P. Jenkins, D.S. Baer and R.K. Hanson, "Diode laser sensor for monitoring multiple combustion parameters in pulse detonation engines," Proc. Combust. Inst. 28, 587-594, 2000.

S.T. Sanders, J. Wang, J.B. Jeffries and R.K. Hanson, "Diode-laser absorption sensor for line-of-sight gas temperature distributions," Appl. Opt. 40, 4404-4415, 2001.

San Diego reduced heptane mechanism: http://maeweb.ucsd.edu/~combustion/cermech/.

P. Saxena, F.A. Williams, "Testing a small detailed chemical-kinetic mechanism for the combustion of hydrogen and carbon monoxide," Combust. Flame 145, 316-323, 2006.

S. Schilt, L. Thevenaz, and P. Robert, "Wavelength modulation spectroscopy: combined frequency and intensity laser modulation," Appl. Opt. 42, 6728-6738, 2003.

S. Schilt and L. Thevenaz, "Experimental method based on wavelength-modulation spectroscopy for the characterization of semiconductor lasers under direct modulation," Appl. Opt. 43, 4446-4453, 2004.

C. Schmidt, "Flow reactor study of the effect of pressure on the thermal de-NOx reaction," Ph.D. dissertation, Dept. Mechanical Engineering, Stanford Univ., Stanford, CA, 2001.

F. Schreier, "The Voigt and complex error function: a comparison of computational methods," J. Quant. Spectrosc. Radiat. Transfer., 48, 743-762, 1992.

H. Seiser, H. Pitsch; K. Seshadri, W. J. Pitz, H. J. Curran, "Extinction and autoignition of n-Heptane in counterflow configuration," Proc. Combust. Inst. 28, 2029-2037, 2000.

C.R. Shaddix, "Correcting thermocouple measurements for radiation loss: a critical review," Proc. 33rd National Heat Transfer Conf., Albuquerque, New Mexico, Aug. 1999.

J.A. Silver, "Frequency-modulation spectroscopy for trace species detection: theory and comparison among experimental methods," Applied. Opt. 31, 707-717, 1992.

J.A. Silver and D.J. Kane, "Diode laser measurements of concentration and temperature in microgravity combustion," Meas. Sci. Technol. 10, 845-852, 1999.

S. Song, R.K. Hanson, C.T. Bowman, D.M. Golden, "Shock tube determination of the overall rate of NH2+ NO→ products at high temperatures," Proc. Combust. Inst. 28, 2403-2409, 2000.

N.K. Srinivasan, J.V. Michael, "The thermal decomposition of water," Int. J. Chem. Kinet. 38, 211-219, 2006.

G. Strang, " On the construction and comparison of difference shemes," SIAM J. Num. Analys. 5, 506-517, 1968.

G.J. Sturgess, D.G. Sloan, A.L. Lesmerises, S.P. Heneghan, and D.R. Ballal, "Design and development of a research combustor for lean blow-out studies," J. Eng. Gas Turb. Power 114, 13-19, 1992.

G.J. Sturgess, S.P. Heneghan, M.D. Vangsness, D.R. Ballal, A.L. Lesmerises, and D. Shouse, "Effects of back-pressure in a lean blowout research combustor," J. Eng. Gas Turb. Power 115, 486-498, 1993.

H. Teichert, T. Fernholz, and V. Ebert, "Simultaneous in situ measurement of CO, H$_2$O, and gas temperatures in a full-sized coal-fired power plant by near-infrared diode lasers," Appl. Opt. 42, 2043-2051, 2003.

M. Thiruchengode, S. Nair, S. Prakash, D. Scarborough, Y. Neumeier, T. Lieuwen, J. Jagoda, J. Seitzman, and B. Zinn, "An active control system for LBO margin reduction in turbine engines," 41st AIAA Aerospace Sciences Meeting and Exhibit, AIAA 2003-1008, Reno, NV, Jan. 6-9, 2003.

R.A. Toth, "Extensive measurements of H$_2$^{16}O line frequencies and strengths: 5750 to 7965cm^{-1}," Appl. Opt. 33, 4851-4867, 1994.

R.A. Toth, "Measurements of positions, strengths and self-broadened widths of H$_2$O from 2900 to 8000 cm^{-1}: line strength analysis of the 2nd triad bands," J. Quant. Spectrosc. Radiat. Transfer 94, 51-107, 2005.

P.L. Varghese, Tunable infrared diode laser measurements of spectral parameters of carbon monoxide and hydrogen cyanide. Ph.D. Dissertation, Sanford University, Stanford, CA 94305, 1983.

P.L. Varghese and R.K. Hanson, "Collisional narrowing effects on spectral line shapes measured at high resolution," Appl. Opt. 23, 2376-2385, 1984.

V. Vasudevan, D.F. Davidson, and R.K. Hanson, "High-temperature measurements of the reactions of OH with toluene and acetone," J. Phys. Chem. A 109, 3352-3359, 2005.

W.G. Vincenti and C.H. Kruger, Introduction to Physical Gas Dynamics, Krieger, Malabar, FL, 1965.

R.T. Wainner, B.D. Green, M.G. Allen, M.A. White, J. Stafford-Evans, R. Naper, "Handheld, battery-powered near-IR TDL sensor for stand-off detection of gas and vapor plumes," Appl. Phys. B 75, 249, 2002.

J. Wang, M. Maiorov, D.S. Baer, D.Z. Garbuzov, J.C. Connolly, and R.K. Hanson, " In situ combustion measurements of CO with diode-laser absorption near 2.3 μm," Appl. Opt. 39, 5579-5589, 2000a.

J. Wang, M. Maiorov, J.B. Jeffries, D.Z. Garbuzov, J.C. Connolly and R.K. Hanson, "A potential remote sensor of CO in vehicle exhausts using 2.3 micron diode lasers," Meas. Sci. Technol. 11, 1576-1584, 2000b.

M.E. Webber, J. Wang, S.T. Sanders, D.S. Baer, and R.K. Hanson, "In-situ combustion measurements of CO, CO$_2$, H$_2$O and temperature using diode laser absorption sensors," Proc. Comb. Inst. 28, 407-413, 2000.

R. Wehr, R. Ciurylo, A. Vitcu, J.R. Drummond, A.D. May, F. Thibault, "Dicke-narrowed spectral line shapes of CO in Ar: experimental results and a revised interpretation," J. Mol. Spectrosc. 235, 54-68, 2006.

E.E. Whiting, "An empirical approximation to the Voigt profile," J. Quant. Spectrosc. Radiat. Transfer. 8, 1379-1384, 1968.

G.V.H. Wilson, "Modulation broadening of NMR and ESR line shapes," J. Appl. Phys. 34, 3276-3285, 1963.

A. Yariv, An introduction to theory and applications of quantum mechanics, Wiley, NY, 1982.

References

F.Y. Zhang, T. Fujiwara and K. Komurasaki, "Diode-laser tomography for arcjet plume reconstruction," Appl. Opt. 40, 957-964, 2001.

X. Zhou, X. Liu, J.B. Jeffries, and R.K. Hanson, "Development of a sensor for temperature and water vapor concentration in combustion gases using a single tunable diode laser," Meas. Sci. Technol. 14, 1459-1468, 2003.

X. Zhou, J.B. Jeffries, and R.K. Hanson, "Development of a fast temperature sensor for combustion gases using a single tunable diode laser," Appl. Phys. B 81, 711-722, 2005a.

X. Zhou, X. Liu, J.B. Jeffries, and R.K. Hanson, "Selection of NIR H_2O absorption transitions for in-cylinder measurement of temperature of an IC-engine," Meas. Sci. Technol., 16, 2437-2445, 2005b.

X. Zhou, "Diode-laser absorption sensors for combustion control," Ph.D. dissertation, Dept. Mechanical Engineering, Stanford Univ., Stanford, CA, 2005c.

X. Zhou, J.B. Jeffries, R.K. Hanson, G. Li, E.J. Gutmark, "Wavelength-scanned tunable diode laser temperature measurements in a model gas turbine combustor," AIAA J. 45(2), 420-425, 2007.

P.F. Zittel and D.E. Masturzo, "Vibrational relaxation of H_2O from 295 to 1020 K," J. Chem. Phys. 90, 977-89, 1989.

Zolo website: http://www.zolotech.com/sub/industrial/.